UNIVERSITY OF HAMBURG
OBSERVATORY OF HAMBURG

PHD THESIS

to obtain the title of

PhD of Science

of the University of Hamburg - Germany
Speciality : ASTROPHYSICS

Defended by
Dimitris MISLIS

Theory and applications for transiting extrasolar planets

Thesis Advisor: Prof. Dr. Schmitt J.H.M.M
defended on 09 June, 2010

Abstract

We present our work in the field of transiting exoplanet systems. Our studies include ground based observations and techniques in combination with space missions (CoRoT & Kepler). In this Thesis, we present our results for transits theory and observations. We have built the Photometric Software for Transits, in order to handle ground based transiting data, and the CoRoT Detrend Algorithm to correct and analyze CoRoT light curves. Using the 1.2m Oskar-Lühning Telescope from Hamburg Observatory and the 2.2m Calar Alto telescope (with BUSCA CCD) we have studied the TrES-2b transiting system. Inclination change has been found after one year of observations (May 2008 - May 2009) probably, because a non-transiting secondary planet. Also, using Tycho catalog we have calculated the transit probability of $\sim 10^6$ stars. We present probability maps of the full sky, for Hot Jupiters and habitable planets, as well. The probability for a Hot Jupiter using a ground based survey (e.g SuperWasp or HatNet) is smaller that $\sim$ 13%. From space, using CoRoT IRa01 data, we calculate that the probability of habitable planets is high enough. We prove the eccentricity threshold of habitable orbits, which the maximum eccentricity $e_{max} = 0.397$, is independent of any stellar properties. Finally, we present a method to extract information for the planetary system (e.g. planetary albedo, eccentricity, ω) using only the photometric light curve of the transit and Kepler's equation if the photometric accuracy is high enough, without any Radial Velocity measurements.

Contents

Chapter 1

Introduction

1.1 Historical Overview

The Greek philosopher Mitrodoros from Chio (~ 4 B.C) said : “If someone assumes that the Earth is the only planet with life in the endless universe, in principal he believes, that from one field full of seeds will grow only one of them”. Simplicius quoted that the philosopher Anaxagoras (500 B.C) believed that there are infinity number of worlds in the universe. Ippolitos, Lefkipos and Democritus agreed with the point of Anaxagoras. After a century, Loukritios (Roman philosopher) wrote: “Nothing is unique in Nature. There are other worlds like Earth with people and animals in the universe”. In 13^{th} century A.C the Chinese philosopher Teng Mou from the Souing dynasty wrote: “The Earth is like a person in a kingdom. A tree has many fruits, and a kingdom many persons. Is not logic to assume that other worlds like Earth do not exist”. Some centuries later, Johhannes Kepler discovered the planetary motion laws and at the end of 17^{th} century, P. Laplace and E. Kant suggested the first scientific theory for planetary creation. In early 19^{th} century, after measuring the temperature of stars, astronomers realized that stars are too hot to harbour life. Some decates later the German astronomer Otto Struve (Fig. 1.1), was the first one who proposed observations of transit events as a means of exoplanetary detection (Struve 1952).

Today (Spring 2010) more that 430 exoplanets have already been discovered. The definition of an extra solar planet is a planet in an orbit around a star different from the Sun. For the discovery of these exoplanets, many teams have used many techniques like radial velocity measurements, photometry (transits), gravitational lensing, astrometry, imaging. The most popular are the Radial Velocity and the Transit technique. In this Thesis, we will comprehensively study the transit technique. The transit phenomenon is very similar to eclipses. In this case we are measuring the light from the host star for a long time and when the planet is passing in front of the star, the light from the host star barely decreases. We try to detect this tiny light variation of the host star which is the signature of the planet. This is something very difficult using a ground based

Figure 1.1: Otto Struve

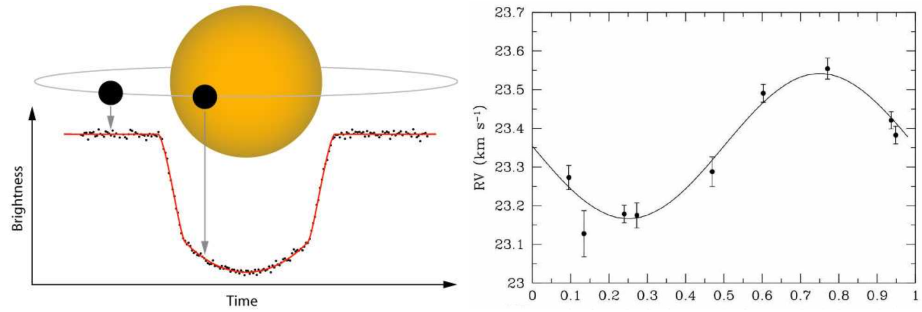

Figure 1.2: **Left:** Transit light curve. **Right** Radial Velocity curve

telescopes but the age of space missions for extra solar planets has already began.

1.2 Transit Theory

As we said above, when the planet passes in front of the host star and the observer, then the star's flux decreases very little because some amount of the light is blocked by the planet. The light curve that we extract is unique for each planetary system and we can derive much information about its physical characteristics like period, radius of the star-planet, inclination of the planet's orbit etc. We will discuss below all these parameters in more detail. Fig. 1.2 shows the geometry of the transit, the transit light curve and the radial velocity curve. Using transit light curves we can measure some parameters and we can calculate some others. First of all, because transit is a periodic phenomenon, we measure the orbital period of the planet (P). Another characteristic is the duration of the transit (D) and also the depth of the light curve ($\Delta Flux$). These three quantities are what we measure from the light curve directly. If we know that the star has a transiting planet it is very easy to use radial velocity technique to calculate other physical parameters, which only with radial velocity measurements could be calculated, like the semi-major axis (α) and planetary mass (M_p) using the equation *(Charbonneau et al. 2006)*

$$K = \left(\frac{2\pi G}{P}\right)^{1/3} \frac{M_p \sin i}{M_*^{2/3}} \frac{1}{\sqrt{1-e^2}}, \tag{1.1}$$

where K is the amplitude of the RV curve, P is the period, M_p and M_* is the mass of planet and the mass of the star respectively and e is the eccentricity of the orbit. The first term of th Eq. 1.1 is function of the semi-major axis α (Kepler's 3^{rd} law). Now we can return to transit equations. We already know the mass of the planet (M_p) and the semi-major axis of the orbit (α) from radial velocity and the duration (D), the orbital period (P) and the depth of the light curve $\Delta Flux$ from the transit. Using Eq. 1.2 we can derive the radius of the planet (R_p) *(Seager & Mallén-Ornelas 2003)*

$$R_p = R_s \cdot \sqrt{\Delta Flux} \tag{1.2}$$

and from Eq. 1.3 we can derive the inclination of the orbit (i) (function of duration, (D), period (P) semi-major axis (α), the radius of the planet and the radius of the star, (R_p) and (R_*) respectively - *Charbonneau et al. 2006*).

$$D = \frac{P}{\pi} \arcsin\left[\frac{R_*}{\alpha \sin i} \sqrt{\left(1 + \frac{R_p}{R_*}\right)^2 - \left(\frac{\alpha \cos i}{R_*}\right)^2}\right], \tag{1.3}$$

We will continue the package of basic transit equations with the limb-darkening law. As we know, the surface of a star does not irradiates homogeneously. The immediate effect is that the planet does not cover the same amount light, from of the stellar surface. This phenomenon is also known as limb-darkening of transits (Eq. 1.6).

The probability of a transit event is also an important issue. The geometry and the inclination of the system star-planet play the main role for the probability to observe the transit, which is very small. Only if the inclination of the planet's orbit is high enough, we could detect the transit from the Earth. For Hot Jupiters this probability is higher because the orbital distance from their host star is smaller. The probability equation for Hot Jupiters detection is

$$P_r = 0.238 \left(\frac{M_*}{M_o}\right)\left(\frac{R_*}{R_o}\right)\left(\frac{P}{d}\right), \tag{1.4}$$

(Gilliland et al. 2000) where M_* and R_* are the stellar mass and radius respectively in solar units and P is the period of the planet in days. For Eq. 1.4, we assume circular orbits (Hot Jupiters mostly). For larger orbital distances (possible eccentric) we are using a different equation *(Seagroves et al. 2003)*

$$P_r = 0.0045 \frac{1AU}{\alpha} \frac{R_*}{R_o} \frac{1 + e\cos(\pi/2 - \omega)}{1 - e^2}, \tag{1.5}$$

where α is the semi-major axis, e is the eccentricity and ω is the periastron of the orbit. These two equations are basic for the analysis which have done in Chapter 5 and 6.

1.3 Transit Modeling

The light curve modeling of a transit is the most useful part of the analysis. As a model we define the theoretical light curve of the transit if there is no noise in our data. There are some works in this field (e.g. from Mandel & Algol - *Mandel et. al. 2006* or Pál - *Pál et. al. 2008*). For this Thesis we used the Pál's transit model and below are the basic equation for the model. First of all, we are using a quadratic limb darkening law

$$I(r) = 1 - \sum_{m=1,2} \gamma_m \left(1 - \sqrt{1 - r^2}\right)^m, \tag{1.6}$$

where r is the normalized distance from the center of the star ($0 \leq r \leq 1$), γ_1 and γ_2 are the limb darkening coefficient (or u_1 and u_2) and the flux of the star is

$$f = 1 - \Delta f, \tag{1.7}$$

Δf is defined as

$$\Delta f = W_o F_o + W_2 F_2 + W_1 \left[F_1 + F_K K(k) + F_E E(k) + F_\Pi \Pi(n,k)\right], \tag{1.8}$$

where

$$W_o = \frac{6 - 6\gamma_1 - 12\gamma_2}{6 - 2\gamma_1 - \gamma_2}, \tag{1.9}$$

$$W_1 = \frac{6\gamma_1 + 12\gamma_2}{6 - 2\gamma_1 - \gamma_2}, \tag{1.10}$$

$$W_2 = \frac{6\gamma_2}{6 - 2\gamma_1 - \gamma_2} \tag{1.11}$$

The terms F_0, F_1, F_K, F_E, F and F_2 are only functions of the occultation geometry and the functions $K(k)$, $E(k)$ and $\Pi(n,k)$ denote the complete elliptic integrals of the first, second and third kind respectively (k and n are constants).

$$K(k) = \int_0^{\frac{\pi}{2}} \frac{d\theta}{\sqrt{1 - k^2 \sin^2\theta}}, \tag{1.12}$$

$$E(k) = \int_0^{\frac{\pi}{2}} \sqrt{1 - k^2 \sin^2\theta}\, d\theta, \tag{1.13}$$

$$\Pi(n,k) = \int_0^{\frac{\pi}{2}} \frac{d\theta}{(1 - n\sin^2\theta)(\sqrt{1 - k^2 \sin^2\theta})}, \tag{1.14}$$

Based on these equations we build the transit model which we use in this Thesis.

1.4 Algorithms BLS, SysRem, TFA

In this section we present some useful algorithms which have used in this Thesis. This is the Box Least Square (BLS) for exoplanet detection, the SysRem and the Trend Filtering Algorithm (TFA) for noise calibration of the data.

1.4.1 Box Least Square Algorithm

The Box Least Square algorithm was developed by G. Kovacs for transits detection *(Kovacs et.al. 2002)*. Since then BLS is the most popular algorithm for a transit survey. Here we present how it works.

Let's assume a periodic signal with period P. We define the data set as LC_i with $i = \{1, 2, 3, ...n\}$. The duration of the transit is $D = q_o P$, where q_o is a free parameter and the depth of the transit is $\Delta Flux$. If the transit starts at phase ϕ_1 and ends at phase ϕ_2, then the box-transit function is given by Eq. 1.15

$$BF(\phi) = \begin{cases} LC_i & \text{if } \phi \leq \phi_1 \text{ and } \phi \geq \phi_2 \\ LC_i - \Delta Flux & \text{if } \phi_1 < \phi < \phi_2 \end{cases} \tag{1.15}$$

where ϕ is the phase. When we use a normal χ^2 fit

$$BLS_{number} = \sum_{i=1}^{n} \left[\frac{LC_i - BF_i}{\sigma_i} \right]^2 \tag{1.16}$$

where n is the total number of points and σ_i the flux errors. The fitting parameters are the period P, duration limits ϕ_1 and ϕ_2 and the depth $\Delta Flux$. Fig 1.3 shows an example of how BLS works. We used CoRoT-1b exoplanet for testing BLS. CoRoT-1b has period P=1.5089557 days and the period window we have used is up to 10 days (from 1 to 10 days with step size 0.001 days). The BLS number for each period is close to 0.007. The correct period of ~ 1.508 days gives $BLS_{number} = 0.003$ (Fig. 1.3).

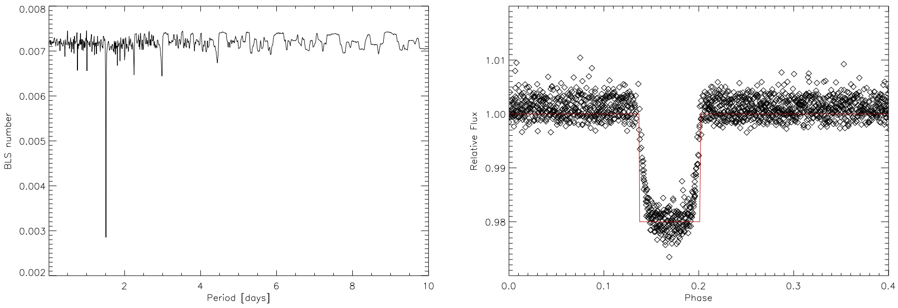

Figure 1.3: **Left:** The BLS number (χ^2) vs period for CoRoT-1b exoplanet. **Right:** Phase diagram (dots) and BLS results (red solid line) for CoRoT-1b.

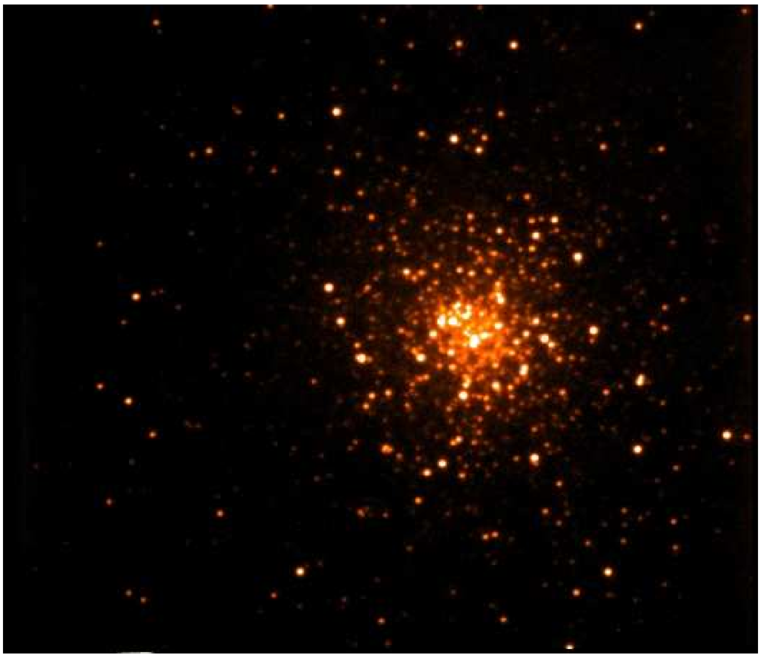

Figure 1.4: M92 Globular Cluster from OLT

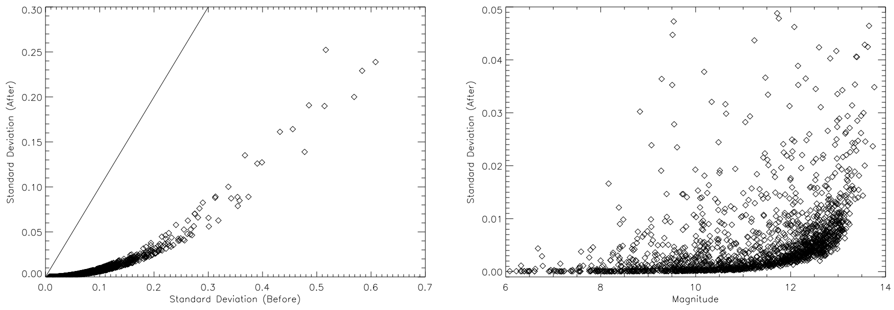

Figure 1.5: **Left:** Light curve standard deviation before vs after SysRem. **Right:** Light curves standard deviation vs magnitude. Using SysRem, the accuracy is high enough for transiting planets ($RMS < 0.01$).

1.4.2 SysRem Algorithm

SysRem is a data reduction algorithm by Tamuz *(Tamuz et. al. 2005)* for detrending systematic effects from light curves. SysRem has been used by many surveys for data reduction because most of them are using small telescopes and lenses. With this instruments is quite difficult to detect a transit because the noise is high enough to cover the transit signal. The main idea of SysRem is to reduce the systematic effects that the data might have like atmospheric effects, extinction, PSF changes and detectors efficiency. SysRem is using all the light curves of the field to remove these kind of trends. We assume N light curves and K measurements per light curve. We define the airmass data set, as $\{a_j; j = 1, 2, ..., K\}$ and each raw light curve data set as $\{w_{i,j}; i = 1, 2...N\}$. The final light curves are produced by the equation

$$w_{i,j} = w_{j,i} - c_i^1 a_j^1 \tag{1.17}$$

where c_i is the extinction coefficient

$$c_i^1 = \frac{\sum_j (w_{i,j} a_j / \sigma_{i,j}^2)}{\sum_j (a_j^2 / \sigma_{i,j}^2)} \tag{1.18}$$

and $\sigma_{i,j}$ is the error of each measurement per frame. The label ^{1} (c_j^1) means that the extinction coefficient is a first order parameter. After we found the first order of extinction coefficient, we can calculate the first order of airmass data set using

$$a_i^1 = \frac{\sum_j (w_{i,j} c_i / \sigma_{i,j}^2)}{\sum_j (c_i^2 / \sigma_{i,j}^2)} \tag{1.19}$$

We can run again and again these equation to derive the second, third or fourth order of the extinction coefficient. Each time the algorithm removes a different part from systematic effects. Fig 1.5 shows an example of the SysRem algorithm using data from the Globular Gluster M92 and 1.2m Oskar-Lühning Telescope (OLT) (Fig. 1.4).

1.4.3 Trend Filtering Algorithm

Trend Filtering Algorithm is one more algorithm for data reduction, instrumental effects and systematic variation, developed by G. Kovacs in 2004 *(Kovacs et. al. 2004)*.

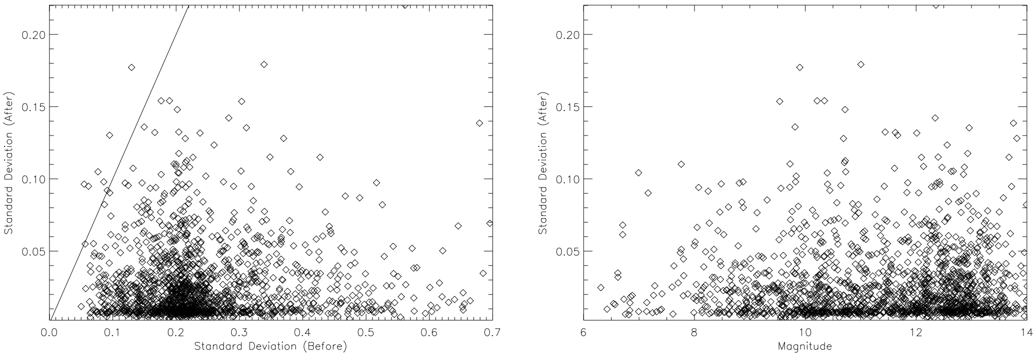

Figure 1.6: **Left:** Light curves standard deviation before vs after TFA. **Right:** Light curves standard deviation after TFA vs magnitude. As a conclusion, SysRem produces better results that TFA (Fig 1.5-1.6).

TFA, as SysRem, has been used by many survey teams and it is more powerful in wide or crowed fields. We assume that each light curve is a time-series $T_j(i)$, where j is the star id number and i the frame number. After we zero-average all the light curves, TFA makes a base data set (we are using 100 stars as base in this example) including only the light curves with the minimum variation. We call $X_j(i)$ each base light curve and we calculate the base-matrix below

$$g_{j,k} = \sum_{i=1}^{N} X_j(i) X_k(i), \tag{1.20}$$

where N is the total data points. After we compute the inverse matrix of $g_{j,k}$ ($G_{j,k}$), we derive for each target-light curve ($T(i)$) the h-factor

$$h_j = \sum_{i=1}^{N} T(i) X_j(i) \tag{1.21}$$

We also need to estimate the c-factor by

$$c_i = \sum_{k=1}^{M} G(j,k) h_k \tag{1.22}$$

where M is the total number of frames. The final equation which will produce new light curves is

$$NTi = T(i) - \sum_{k=1}^{M} c(i) X_j(i) \tag{1.23}$$

where $NT(i)$ is the final light curve. The advantages of TFA is that the results quality is function of the number base-stars. For crowded fields case, can use many stars as a base. The disadvantages, are that the base-stars cannot be used after TFA, so all the base-stars are excluded from the survey. Fig. 1.6 shows an example of TFA. We applied the algorithm in the same field of M92 as before (SysRem).

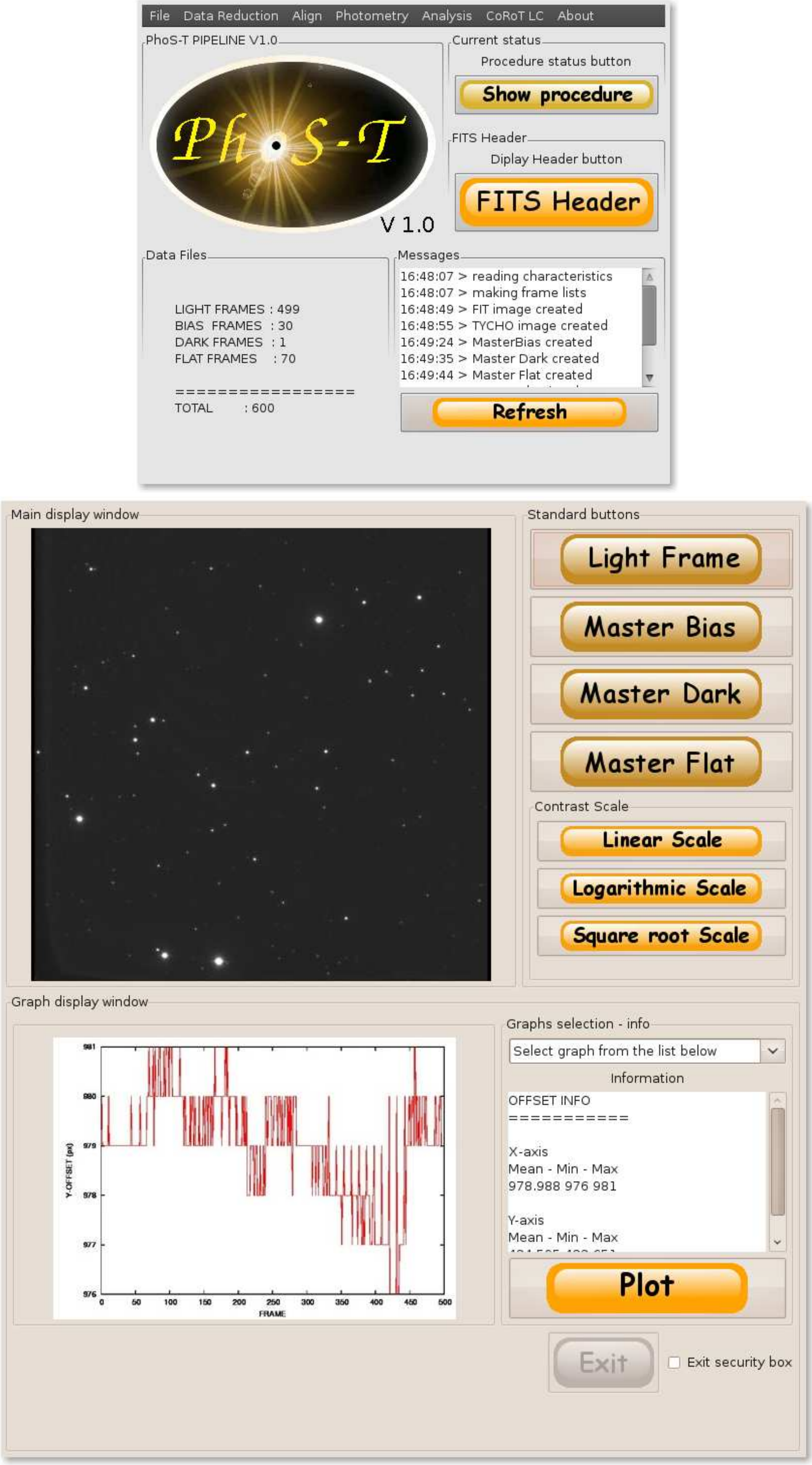

```
LIGHT FRAMES : 499
BIAS  FRAMES  : 30
DARK FRAMES  : 1
FLAT FRAMES    : 70

=================
TOTAL        : 600
```

```
16:48:07 > reading characteristics
16:48:07 > making frame lists
16:48:49 > FIT image created
16:48:55 > TYCHO image created
16:49:24 > MasterBias created
16:49:35 > Master Dark created
16:49:44 > Master Flat created
```

```
OFFSET INFO
===========

X-axis
Mean - Min - Max
978.988 976 981

Y-axis
Mean - Min - Max
```

Figure 1.7: Two screens of PhoS-T

1.5 PhoS-T Software

Phos ($\Phi\Omega\Sigma$) is the Greek word for light. PhoS-T is an abbreviation for Photometric Software for Transits and is a *graphical* software for data reduction and light curve analysis (Fig. 1.7). The software has been created in order to analyze transiting light curves. PhoS-T has three modes. In the first mode user could run the packages below :

- Bias - Dark - Flat reduction
- Frame Alignment
- Photometry
- Light curve creator
- Transit modeling
- Monte Carlo simulation

In the second mode the user could upload a previous light curve using PhoS-T for further analysis and finally, in the third mode, PhoS-T includes an additional packages for calibration and analysis of CoRoT's data (using CDA - see chapter 6).

- CDA application
- BLS (see section 1.4.1)
- Transit modeling
- Monte Carlo simulation

We will discuss PhoS-T with more details in Chapter 8. Also in Appendix-A we present one version of the software's manual.

1.6 Telescopes & Instruments

To complete this Thesis we have used several instruments and telescopes. The first one is the Oskar-Lühning telescope (OLT) at Hamburg's observatory (Fig.1.8). OLT is a 1.2m telescope and focal length of a 15.60m in Cassegrain focus. It uses two different CCDs with 5 filters from B-band to I-Band and Ha-narrow filter. The first CCD has resolution $1Kx1K$ and the total field of view is $5.4^{'}x5.4^{'}$. Readout noise and gain are 4.68 e and 1.12 e^{-}/ADU respectively. The second CCD has resolution $3Kx3K$ and the readout noise and gain are 16.37 e and 1.33 e^{-}/ADU respectively. We used this telescope for photometry of TrES-2b exoplanet (Chapter 2-3).

Another instrument what we used is the 2.2m telescope at Calar Alto (Spain), also for the photometry of TrES-2b exoplanet with BUSCA CCD on it (Fig. 1.8). BUSCA is a powerful instrument. Has four individuals CCDs and the opportunity for multi-band photometry in four bands simultaneously from ultra-violet to near-infrared part of the spectrum. The combination of the 2.2m telescope and BUSCA CCD produce a field of view of $11^{'}x11^{'}$. The readout noise of the detectors are $9.09e$, $3.50e$, $3.72e$, and $3.86e$ respectively for the a,b,c, and d channels. The gain values for the same channels are $1.347e/ADU$, $1.761e/ADU$, $1.733e/ADU$ and $1.731e^{-}/ADU$ respectively.

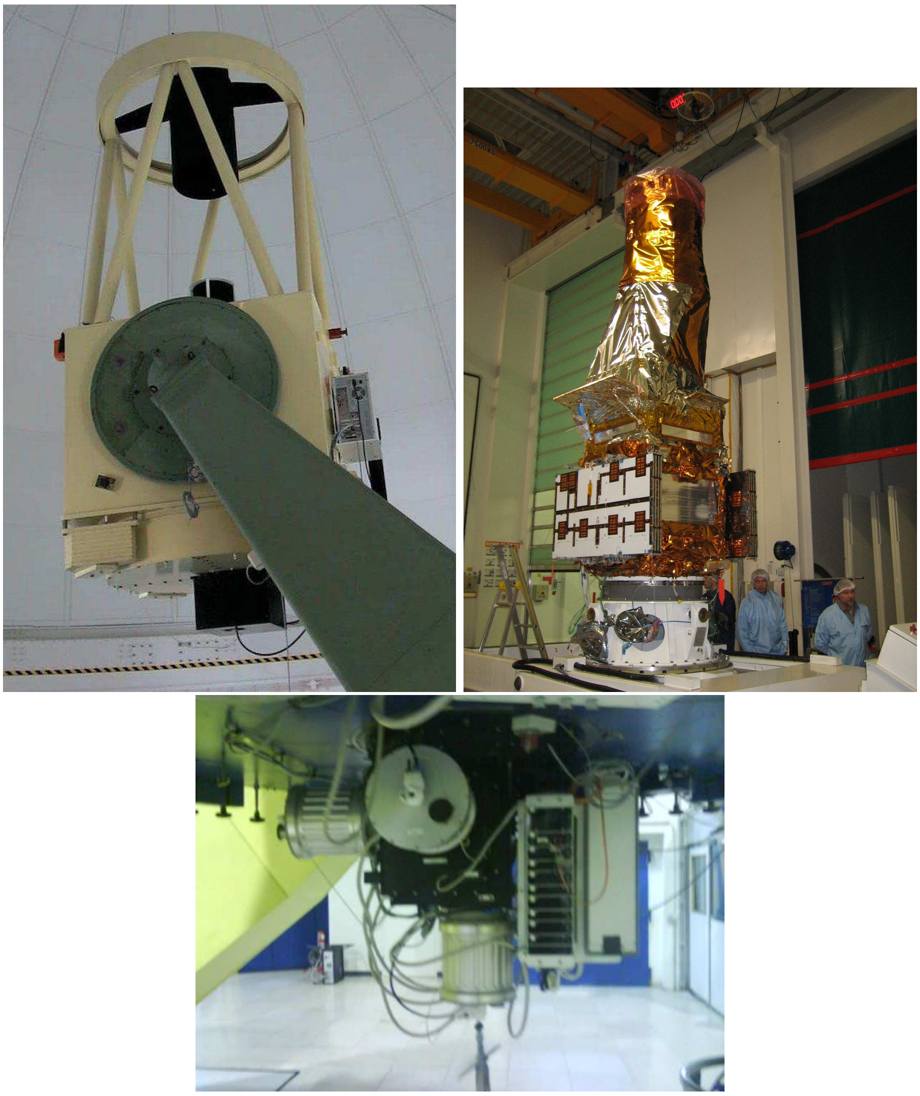

Figure 1.8: **Left** The 1.2m Oskar-Lühning telescope. **Right** CoRoT satellite. **Bottom** BUSCA CCD

CoRoT (COnvection, ROtation & planetary Transits) was the first exoplanet mission capable to detect not only Hot Jupiters but rocky planets as well (Chapter 5 - Fig. 1.8). It was launched on 27 December 2006 and consists a small telescope (29 cm) and two cameras, for the asteroseismology and for exoplanet survey. The field of view is 2.8^o x 2.8^o. CoRoT provides light curves in four different bands (white color, red, green and blue - Chapter 6). Until now, CoRoT has discovered the smallest planet (CoRoT-7b - $M = 0.035 M_j$ and $R = 0.15 R_j$) and many other Hot Jupiters. For this Thesis we used only the channel for exoplanets. CoRoT's data are coming in four bands (white light, red, green and blue band) and in two exposure modes. Using the slow one, CoRoT takes one image per 8 minutes. When it finds an interesting object change to the fast mode and takes 1 image per 32 seconds due to study the object with higher time resolution. CoRoT follows a polar inertial circular orbit and the total duration of the mission is ~ 6 years. We will study CoRoT's data with more details in Chapter 7.

1.7 Thesis structure

In this Thesis we present a study of transiting exoplanets. At the second and third Chapter we will discuss TrES-2b exoplanet. TrES-2b is a Hot Jupiter and we present the analysis of planet's orbit using ground base telescopes. A transit probability about Hot Jupiters and their distribution is given in Chapter 4. The same idea about distribution of habitable planets using ground based and space telescopes is given in Chapter 5 (CoRoT and Kepler). In Chapter 6 we present CoRoT's data main problem and the solution that we suggest using the CoRoT Detrend Algorithm (CDA). In Chapter 7 we discuss a general transiting model including the thermal emission of the planet and the reflected light from it. Assuming high accuracy data (Kepler mission - JWST) we are able to determine extra parameters of the planetary system like eccentricity (e), orbital orientation angle (ω) and even the planetary albedo (a_g) using only the light curve. Finally, in Chapter 8 we give an introduction of the Photometric Software for Transits (PhoS-T) for data reduction and transiting planets light curve analysis.

1.8 Bibliography

Charbonneau, D., Winn, J. N., Latham, D. W., et. al. 2006, ApJ, 636, 445
Claret, A. 2004, A & A, 428, 1001
Gilliland, R. L., Brown, T. M., Guhathakurta, P., et al. 2000, ApJ, 545, L47
Kovács, G., Bakos, G., & Noyes, R. W. 2005, MNRAS, 356, 557
Mandel, K., & Agol E., 2002, ApJ, 580, L171
Pál, A. 2008, MNRAS, 390, 281
Seager, S. & Mallén-Ornelas, G. 2003, ApJ, 585, 1038
Seagroves, S., Harker, J., Laughlin, G., et al. 2003, PASP, 115, 1355
Tamuz, O., Mazeh, T., & Zucker, S. 2005, MNRAS, 356, 1466

Chapter 2

Detection of orbital parameter changes in the TrES-2b exoplanet ?

D. Mislis and J.H.M.M. Schmitt

Astronomy & Astrophysics, 508, L45-L49, 2009

LETTER TO THE EDITOR

Detection of orbital parameter changes in the TrES-2 exoplanet ?

D. Mislis & J.H.M.M. Schmitt

Hamburger Sternwarte, Gojenbergsweg 112, D-21029 Hamburg
email : mdimitri@hs.uni-hamburg.de

Accepted : 18 May 2009

ABSTRACT

We report a possible change in the orbit parameters of the TrES-2 exoplanet. With a period of 2.470621 days, the TrES-2 exoplanet exhibits almost ”grazing” transits 110.4 minutes duration as measured in 2006 by Holman and collaborators. We observed two transits of TrES-2 in 2008 using the 1.2m Oskar-Lühning telescope (OLT) of Hamburg observatory employing CCD photometry in an i-band and a near to R-band filter. A careful light curve analysis including a re-analysis of the 2006 observations shows that the current transit duration has shortened since 2006 by ≈ 3.16 minutes. Although the new observations were taken in a different filter we argue that the observed change in transit duration time cannot be attributed to the treatment of limb darkening. If we assume the stellar and planetary radii to be constant, a change in orbit inclination is the most likely cause of this change in transit duration.

Keywords Stars : planetary systems – Techniques : photometry

2.1 Introduction

The study of transits is one of the most powerful methods in exploring extrasolar planet properties. Although transits events are rare, viewing geometry dependent phenomena, they can provide information about extrasolar planets and that is otherwise inaccessible. Space missions such as CoRoT or the Kepler mission use the transit method in surveys of extrasolar planet systems. The transit light curve incorporates all relevant physical system parameters and, therefore, a highly accurate extrasolar planet transit light curve provides access to this information. The orbits of the planets in our solar-system as well as the Moon and artificial Earth-orbiting satellites are known to undergo secular changes in their orbit parameters. The reasons for these changes are the gravitational attraction of other (”third”) bodies, deviations from spherical symmetry, air drag, non-gravitational forces and relativistic effects among others. Similarly, the orbits of extrasolar planets are expected to vary at some level, although, there is so far no evidence that the orbit or the physical parameters of any exoplanet have changed.

Changes in the orbit inclination i caused by a precession of the orbit plane are particular interest. Transiting planets are ideal for detecting these changes, especially when the transit is ”grazing”, i.e., when the planet eclipses only the polar regions of its host star. As a consequence, extrasolar planets with lower inclination and larger impact values (but still producing transits) such as the cases of OGLE-56, TrES-2, TrES-3, and TrES-4 are particularly well suited to detecting these orbital changes.

The TrES-2 exoplanet system was discovered in 2006 by the TrES (Trans-Atlantic Exoplanet Survey) project (O'Donovan et. al. 2006). Using the Mt. Hopkins Observatory 1.2m FWLO, Holman et. al. (2007) performed the first accurate analysis of TrES-2, using three TrES-2 light curves obtained in the fall of 2006. TrES-2 turned out to be a rather typical hot Jupiter exoplanet of mass $M_p = 1.198 M_J$ and radius $R_p = 1.222 R_J$, orbiting a G0V star of mass $M_* = 0.98 M_{Sun}$ and radius $R_* = 1.003 R_{Sun}$ in a 2.47 day orbit. In this *Letter*, we present new transit observations of TrES-2 obtained on May and September of 2008, which suggest that the orbit inclination and hence the transit duration of TrES-2 have changed.

2.2 Observations and data reduction

We observed two transits of TrES-2 using the ephemeris suggested by O'Donovan et. al. (2006) and by Holman et. al. (2007) from

$$T_c(E) = 2,453,957.6358[HJD] + E \cdot (2.47063 \text{ days}),$$

using the 1.2m Oskar Lühning telescope (OLT) at Hamburg Observatory. For the first observing run on 20 May 2008, we used a $1Kx1K$ CCD with a $5'x5'$ FOV, readout noise of 4.68 e^-, and gain of 1.12 e^-/ADU without filter (corresponding to a near R band). With a 30-second exposure time and $1x1$ binning, we achieved a time resolution of 1.13 minutes. For the second observing run on 18 September 2008, we used a new CCD camera with a $3Kx3K$ chip and $10'x10'$ FOV, readout noise and gain were 16.37 e^- and 1.33 e^-/ADU respectively, with an i-band filter. With this setup, we used a 60-second exposure time and a binning of $2x2$, which provided an effective time resolution of 1.17 minutes. During our observations, the airmass values ranged from 1.661 to 1.081 and from 1.0423 to 1.7176, during the first and second observing runs, respectively, and the seeing was typically 2.93" and 1.85", respectively, which are quite typical of the Hamburg site.

For the data reduction, we used *Starlink* and *DaoPhot* software routines, and the *MATCH* code. After applying bias subtraction, dark correction, and flat fielding, we continued with our photometry. For TrES-2, we selected the aperture photometry mode using apertures centered on the target star, check stars, and sky background. Typical sky brightness values (the night sky is quite bright near Hamburg) for the first and second night was 325.6 and 270.2 ADUs, respectively, i.e., values at a level 1.5% and 1.25% of the star's flux, respectively. We used a total of 4 reference stars to test and calibrate the light curve ($U1320 + 10215660 - 10214928 - 10220179 - 10219455$). To estimate the magnitude errors, we followed Howell & Everett (2001) and used the expression

$$\sigma_{mag} = 1.8057 \frac{\sqrt{N_* + p}}{N_*}, \tag{2.1}$$

where $p = n_{pix}(1 + \frac{N_{pix}}{n_B})(N_S + N_D + N_R^2 + G^2\sigma_f^2)$, N_* is the total number of photons, N_{pix} is the number of pixels, which was used to define N_*, n_B is the total number of background pixels, N_S is the number of total number of photons per pixel from background, N_D is the total number of dark electrons per pixel, N_R^2 is the total number of electrons per pixel due to the readout noise, G is the gain, and σ_f^2 is the 1σ error of the A/D converter (~ 0.289). The factor of 1.8057 converts the errors in flux (electrons) into errors in magnitudes (Howell & Everett 2001), we made no further changes to the

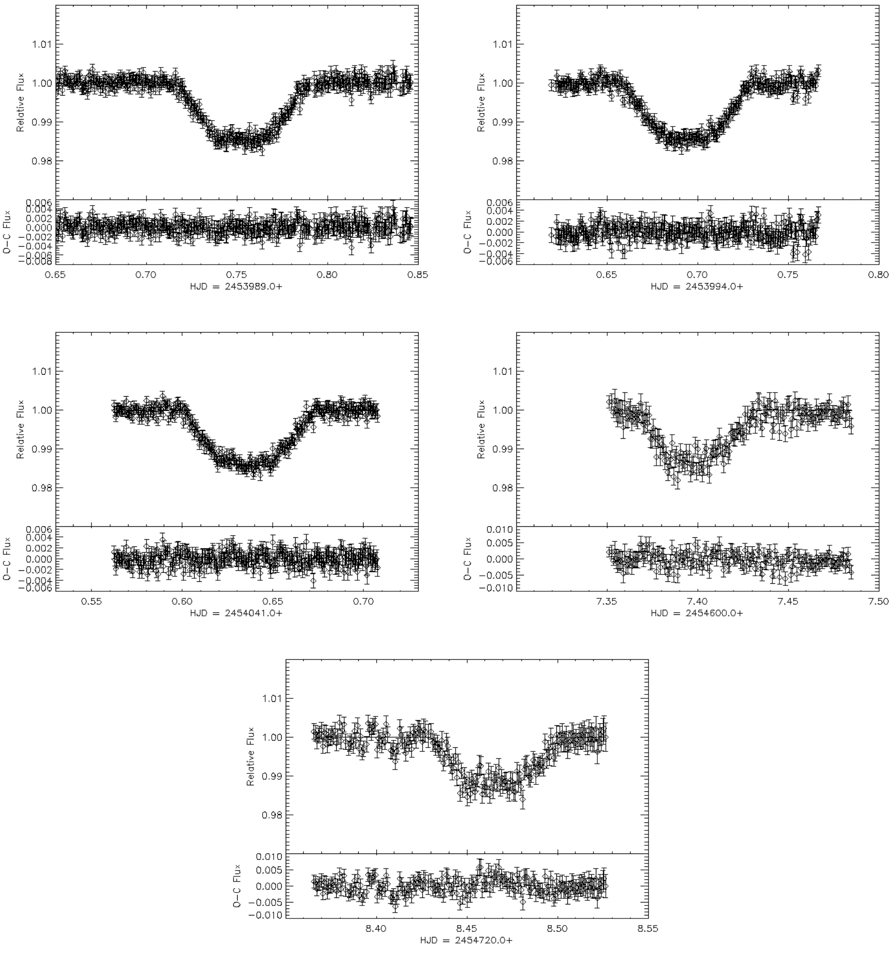

Figure 2.1: Observed TrES-2 light curves, model fits and residuals (lower panel); upper three light curves were taken 1.2m FLWO (Holman et. al. 2007), but fitted with our model code using Holman et al.'s (2007) limb darkening. The lower two light curves were taken with the 1.2m OLT at Hamburg Observatory, and fitted with the same model and the appropriate limb-darkening coefficients. The transit duration measured in 2008 is ~ 3 minutes shorter than that measured in 2006.

Table 2.1: Relative Photometry data.

HJD	$RelativeFlux$	$Uncertainty$
2454607.3512	1.001980	0.0015717
2454607.3528	1.002020	0.0021024
2454607.3536	0.999300	0.0014341
2454607.3543	1.002150	0.0031083
2454607.3551	0.999920	0.0030757
2454607.3559	0.998690	0.0030854

Note : Table 1 is available electronically. The time stamps refer to the Heliocentric Julian Date (HJD) at the end of each exposure.

adopted values of the measurement errors and continued with the light curve analysis with transit model fitting. Our final relative photometry is presented in Table.2.1, which is available in its entirety in machine-readable form in the electronic version of this paper.

2.3 Model analysis

There are various ways of creating a physical transit model as described by Mandel & Agol (2002), Winn (2008), or Kipping (2008). The main physical parameters of an exoplanet system are the host star mass and radius M_*, R_*, the planet mass and radius M_p and R_p, the orbit semi-major axis α_{orbit}, the orbit inclination i_{orbit}, and the limb darkening law. There are also indirect or secondary parameters that can be computed once the main parameters are known, or which have no specific physical meaning or cannot otherwise be measured. These parameters include the central transit time T_c, which can be observed and used as a phase reference. The planetary period P must be determined by other means (i.e., not from the shape of the transit light curves), the eclipse duration and depths are functions of the orbit inclination, the stellar and planetary sizes and the limb darkening law. In our modeling, we assume exactly spherical stars and planets with radii independent of the observing wavelength. We also assume circular orbits and – of course – the validity of Kepler's third law, which links the parameters α_{orbit}, M_*, and M_p, since the period P is known. Usually one needs to fit all the main light curve parameters simultaneously, although, we clearly demand that the masses of star and planet, their radii, and the semi-major axis of the orbit remain constant for all our transit observations.

Following Mandel & Agol (2002) and Holman et. al. (2007) we assume a quadratic limb darkening law of

$$\frac{I_\mu}{I_o} = 1 - u_1(1-\mu) - u_2(1-\mu)^2, \tag{2.2}$$

where μ denotes the cosine of the angle between the surface normal and the observer, and I_o and I_μ are the intensities at disk center and angle μ respectively; a complete list of the system parameters is given in Table 2.2. While in principle the limb darkening coefficients could be fitted by a transit light curve, limb darkening is indicated by the structure of the star's atmosphere and should not have to be adjusted to fit a specific transit light curve. Based on Claret (2004) and Sozzetti et. al. (2007), we used the

Table 2.2: TrES-2 physical parameters (adopted from Holman et al.)

TrES-2 system parameters	*Values*
M_*	0.98 M_o
M_p	1.198 M_J
R_*	1.003 R_o
R_p	1.222 R_J
Orbit Radius	0.0367 *AU*
Period	2.470621 *days*

values $u_1 = 0.318$ and $u_2 = 0.295$ for the i filter and $u_1 = 0.430$ and $u_2 = 0.265$ for the R filter. The relation between duration and inclination is given by Eq. 2.3 (Charbonneau et. al. 2006; Seager & Mallén-Ornelas 2003)

$$D = \frac{P}{\pi}\arcsin\left[\frac{R_*}{\alpha\sin i}\sqrt{\left(1+\frac{R_p}{R_*}\right)^2-\left(\frac{\alpha\cos i}{R_*}\right)^2}\right], \tag{2.3}$$

where all parameters have the meanings explained above and D denotes the total transit duration. It is important to realize that the duration of a transit as defined by Eq. 2.3 is not a function of the assumed limb darkening coefficients (see also Knutson et. al. 2007), since the stellar and planetary radii are assumed to be wavelength independent; only the transit shape and depth, but not the transit duration depend on the limb dark coefficients.

To determine the best fit model parameters, we used the χ^2 statistic of

$$\chi^2 = \sum_{j=1}^{N_F}\left[\frac{F_{j,obs}-F_{j,mod}}{\sigma_j}\right]^2, \tag{2.4}$$

where N_F denotes the number of available data points, $F_{j,obs}$ the flux, $F_{j,mod}$ the model flux, and σ_j the error in $F_{j,obs}$ all at time j. To ensure a consistent analysis, we re-analyzed the light curves already presented by Holman et. al. (2007) using the appropriate limb darkening coefficients in addition to our own new transit observations.

To determine the error in the derived fit parameters, we used the following bootstrap procedure, which has some similarities to a Markov chain error analysis. In step (1), we obtained the best-fit light curve minimizing Eq. 2.4. In step (2), we computed the best-fit model residuals FR defined by ($FR_j = F_{j,obs} - F_{j,mod}$). In step (3), we determined the second moment σ of the residual distribution, assuming a Gaussian distribution. In step (4), we generate a random light curve (RL_j) using the model and the derived value of σ, and finally in step (5) determined a best-fit to this randomized light curve by repeating step (1). This procedure was repeated typically 1000 times and we recorded the variations in the fit parameters such as inclinations and durations.

2.4 Results

With the method described above we analyzed all available transit observations (cf., Fig. 2.1); the results of our fits are summarized in Table 2.3, where we also indicate the darkening coefficients used in the analysis (upper five entries). For the Table 2.3,

Table 2.3: Duration, inclination, χ^2 values and limb darkening coefficients from five light curve fits; units for duration and errors are minutes and for inclination and errors are degrees.

Tc time $[HJD]$	*Duration*	*Errors*	*Inclin.*	*Errors*	χ^2*value*	*LDL*
3989.7529 ± 0.0069	110.308	0.432	83.59	0.019	432.1	$S1$
3994.6939 ± 0.0066	109.230	0.448	83.56	0.019	296.8	$S1$
4041.6358 ± 0.0070	109.025	0.430	83.55	0.019	290.6	$S1$
4607.4036 ± 0.0072	106.620	0.883	83.44	0.036	179.1	$S2$
4728.4740 ± 0.0071	106.112	0.870	83.43	0.036	190.1	$S3$
3989.75286	113.275		83.74		443.0	$S2$
3989.75286	111.632		83.66		435.6	$S3$
3994.69393	111.450		83.65		305.5	$S2$
3994.69393	110.195		83.60		300.1	$S3$
4041.63579	111.790		83.67		296.6	$S2$
4041.63579	110.197		83.60		292.4	$S3$
4607.40356	104.317		83.35		180.0	$S1$
4607.40356	105.060		83.38		179.1	$S3$
4728.47400	104.890		83.37		195.7	$S1$
4728.47400	107.100		83.47		192.6	$S2$

we used three sets of limb dark coefficients. Set-1 for Holman's data (S1:$u_1 = 0.22$, $u_2 = 0.32$), Set-2 for OLT's data in R filter (S2:$u_1 = 0.430$, $u_2 = 0.265$), and finally, Set-3 for OLT's data in i filter (S3:$u_1 = 0.318$, $u_2 = 0.295$). In the first part of table, we listed the best-fit results using the most suitable set of limb dark coefficients. In the second part, we used all the possible combinations of limb dark coefficients to show that duration is not strongly affected by limb darkening. Holman's light curves have 433, 301, and 299 data points, and ours have 169 and 193 data points, respectively. With our new observations, we now have precise measurements of T_c for five transits, so we are able to refine the ephemeris equation. A least squares fit to these five transit events results in the expression

$$T_c(E) = 2,453,957.63403\,[\mathrm{HJD}] + E \cdot (2.4706265\,\mathrm{days}).$$

In our basic analysis, we assumed the period, masses, radii, and semi-major axis of the orbit to have the values derived by Holman et. al. (2007). With this approach, we found that the OLT data taken in 2008 appear to prefer different inclinations than the FLWO data taken in 2006 (cf., Table 2.3). To assess the significance of these inclination differences, we carried out the following analysis. We assumed that the five transit light curves (cf., Fig. 2.1) can be described by variable stellar and planetary radii, variable inclination, and variable central transit times (model A; 20 fit parameters), and generated 1000 realizations of this light curve with the method described above. In model B (10 fit parameters), we fixed the stellar and planetary radii to a common value, but still allowed the inclinations and central transit times to vary for each data set, while in model C with (5 fit parameters), we also kept all inclinations constant at the best-fit model value and allowed only the transit times T_c to vary. The generated random light curves were then fitted (via χ^2 minimization) by models (A), (B), and (C), and the errors were computed as described above; clearly, the closest fits are expected

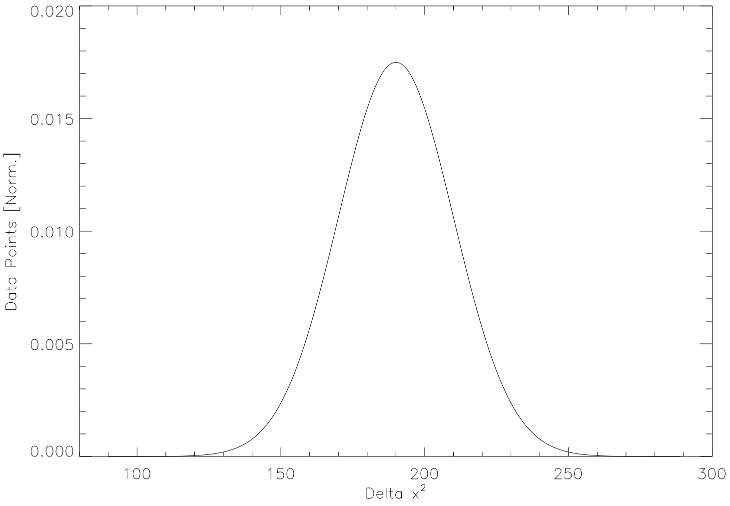

Figure 2.2: Fit improvement $\Delta\chi^2$ for 1000 Monte Carlo realizations when going from models of fixed inclination to models of free inclination (see text for details).

for model (A), and the poorest fits for model (C), which is, however, the ”canonical” model. The essential question is whether the fit improvement between models C, B, and A is significant or not ?

We first consider the fit improvement between models (C) and (B); for each generated light curve, we can compute the appropriate $\Delta\chi^2$, and the distribution of these $\Delta\chi^2$ residuals is shown in Fig. 2.2. A typical value of $\Delta\chi^2$ is clearly ≈ 200, and an F-test indicates that the fit improvement between model (C) and model (B) is highly significant; carrying out the same exercise for going from model (B) to model (A), we find any additional fit improvement is insignificant. This does of course meet our physical expectations, since the sizes of the star and planet are not expected to change, while the orbit inclinations might change.

The bootstrapped error distribution of the derived inclinations in model (B) at the five epochs is shown in Fig. 2.3, which shows the distributions to have very little overlap. We thus conclude that from a statistical point of view the change in inclination observed in the 2008 data is very significant.

Can the apparent change in inclination be caused by errors in the analysis? We investigated possible non-physical causes of the derived inclination change. Our own OLT observations were not carried out with the same filter as the observations by Holman et. al. (2007). Since our fit approach explicitly assumes that the stellar radius is independent of wavelength, the eclipse duration defined by Eq. 2.3 depends only on both the sizes of the host star and planet and the orbit inclination, but not on the shape of the transit light curve, which depends on the chosen limb darkening law. Since we keep the stellar and planetary radius fixed in our fitting scheme (model B), a change in inclination is the only way to produce a change in eclipse duration. However, since the entire observed light curve is fitted to an assumed model light curve, we can obtain an incorrect fit and thus an incorrect inclination and duration if we assume an inappropriate limb darkening law.

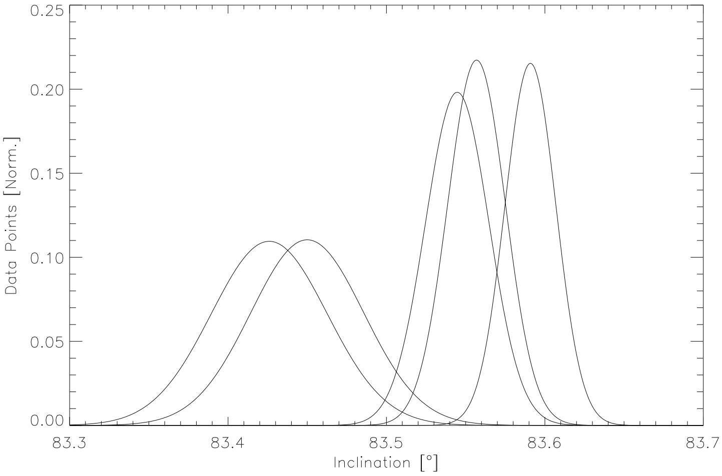

Figure 2.3: Inclination error distribution derived from 1000 *Monte Carlo* bootstraps: OLT light curves (left) and FLWO light curves (right).

Since the Hamburg OLT observations were carried out in ”bluer” filters (than the filter which Holman used) with larger contrasts between disk center and limb, we assessed the influence of limb darkening by analyzing all data for all limb darkening coefficients, assuming a quadratic limb darkening law specified by Eq. 2.2; the results of these fits are also given in Table 2.3 (lower ten entries). As is clear from Table 2.3, the derived durations depend on the assumed limb darkening coefficients, although, the inclination discrepancy between the 2006 and 2008 data cannot be attributed to limb darkening. We further note that the nominal limb darkening coefficients provide the best fits in all cases.

Finally, we asked ourselves which sets of limb darkening model coefficients would provide the best-fit light curve to our new OLT data, keeping the transit duration fixed at the values observed in 2006. With this fit setup we found poorer fits ($\chi^2 = 204.58$) with unrealistic limb darkening coefficients of $u_1 = 0.4258$ and $u_2 = 0.2254$, corresponding to $T_{eff} \sim 4800^oK$, for epoch-312 (Claret 2004), too low given the spectral type of TrES-2’s host star. We repeated the experiment for all combinations of limb darkening coefficients in the range $0.00 < u_1 + u_2 < 1.00$, and found a best-fit model with $\chi^2 = 182.0$, although, the corresponding coefficients of $u_1 = 1.19$ and $u_2 = -0.80$ do not relate to any significant physical meaning. We therefore conclude that the discrepancy between the derived durations of the 2006 and 2008 transits cannot be explained by the assumed limb darkening laws.

Another possible source of error is an incorrect determination of the out-of-transit flux. All assumed model light curves assume an out-of-transit flux of exactly unity. The data points are normalized to unity by the available out-of-transit data points, and therefore the accuracy of this normalization depends on the number of such out-of-transit data points and their respective errors; we note that in the extreme case of zero out-of-transit data points no normalization to unity can be carried out and therefore no meaningful analysis. If the data normalization were for some reason too low, the observed transit depth would be deeper and hence the derived inclination higher (and duration longer); what must then concern us is a data normalization that is too high, reducing the eclipse depth and hence reducing inclination and duration. To study the influence of errors in the data normalization, we introduced a multiplicative amplitude factor to the model, which should nominally be unity but which was allowed to vary to obtain a best fit. In all cases, we found that these amplitudes were close to unity (at the level of a few times 10^{-4}) without any substantial change in transit duration. We thus conclude that normalization errors do not significantly affect our results.

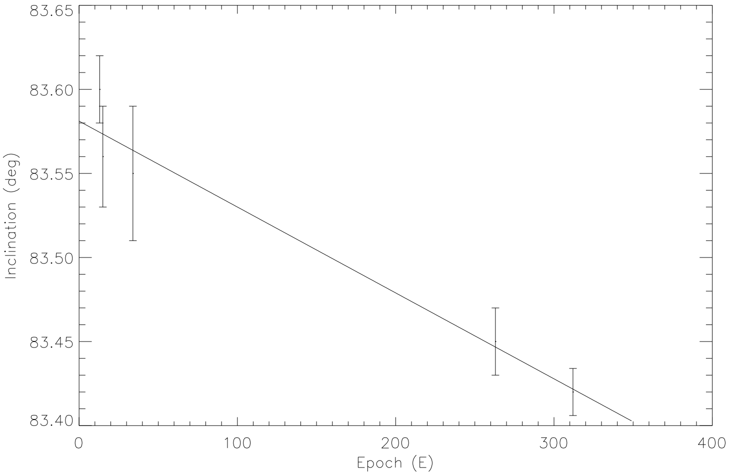

Figure 2.4: Epoch versus inclination: a linear fit is clearly sufficient to describe the available data; if the inclination continues to decrease, the minimum inclination threshold (i_{min} = 81.52^o) will be reached around epoch ~ 4179.

Finally, following Holman et. al. (2007), our modeling approach assumes a spotless star. If the true star were spotted, our modeling approach and thus the inferred model parameters would be incorrect. Clearly, if one were to place spots exactly at those limb positions where the planets enters and leaves the stellar disk, the apparent transit duration would change; at the same time the limb darkening and transit depth would change and it is unclear, what the resulting fit parameters of such an inappropriate model would be. Since we, first, have two transit observations yielding consistent fit results and, second, the $vsin(i)$ of TrES-2's host star is quite low ($<$ 2.0 km/sec, (O'Donovan et. al. 2006) proposed that it was an inactive star and we conclude that star spots are an unlikely explanation of the observed transit duration shortening.

If we accept that the formally measured inclination changes are real, we can study (in Fig. 2.4) the variation in inclination versus time derived from the presently available data; clearly, a linear fit is sufficient for a description. In every transit systems, two theoretical thresholds of minimum inclination angles exist, a first threshold, where the planet is never fully in front of the stellar disk, and a second threshold, where no transit occurs at all. For the TrES-2 system parameters listed in Table 2.2, the first inclination threshold occurs for $i_{min,1}$ = 83.417^o, and the second threshold for $i_{min,2}$ = 81.52^o. From our linear fit shown in Fig. 2.4, the first threshold is reached around $Epoch$ ~ 325 corresponding to October 2008 with an eclipse duration of D = 105.92 minutes.

2.5 Conclusions

Because its orbital properties of TrES-2 is a particularly interesting exoplanet. The transits of TrES-2 are almost ”grazing” and are therefore quite sensitive to inclination changes. By comparing our new 2008 observations of TrES-2 with data obtained in 2006, we have detected an inclination change of 0.1 degrees in a little under two years, corresponding to a transit duration change of about $\sim$ 3.16 minutes. We have investigated the influences of limb darkening and the light curve normalization on the derived inclinations and found that the observed duration changes cannot be attributed to incorrect light curve modeling. We had therefor to search for a physical cause of the observed changes. Since stellar and planetary radii are unlikely to have changed and an explanation related to star spots appears unlikely given the activity status of TrES-2’s host star, a change in the orbital inclination is the only remaining explanation. A third body in the form of an outer planet, which possibly does not cause any transit eclipses, would provide the most straightforward explanation. We emphasize that it appears extremely worthwhile to continue transit monitoring of TrES-2 in the 2008 - 2010 time frame to study its inclination changes as well as to search for further companions of TrES-2 in radial velocity data. In the Kepler field, high precision photometry of hundreds of transits of TrES-2 will be obtained, which should allow a precise determination of all orbit changes as well as a refinement of the stellar and planetary parameters of the TrES-2 exoplanet system.

2.6 Acknowledgements

We want to express our gratitude to Dr. Hans-Jürgen Hagen for his superb technical support at the OLT. We also want to thank Drs. R. Wichmann and M. Esposito and Prof. Dr. G. Wiedemann for useful discussions. DM was supported in the framework of the DFG-funded Research Training Group ”Extrasolar Planets and their Host Stars” (DFG 1351/1).

2.7 References

Charbonneau, D., Winn, J. N., Latham, D. W., et. al. 2006, ApJ, 636, 445

Claret, A. 2004, A & A, 428, 1001 Holman, M. J., Winn, J. N., Latham, D. W., et. al. 2007, ApJ, 664, 1185

Howell, S. B., & Everett, M. E. 2001, in Third Workshop on Photometry, ed. W. J. Burucki, & L. E. Lasher, 1

Kipping, D. M. 2008, MNRAS, 389, 1383

Knutson, H. A., Charbonneau, D., Noyes, R. W., Brown, T. M., & Gilliland, R. L. 2007, ApJ, 665, 564

Mandel, K., & Agol E., 2002, ApJ, 580, L171 O’Donovan, F. T., Charbonneau, D., Mandushev, et. al. 2006, ApJ, 651, L61

Chapter 3

Multi-band transit observations of the TrES-2b exoplanet

D. Mislis, S, Schröter, J.H.M.M. Schmitt, O. Cordes, & K. Reif
Astronomy & Astrophysics, 510, A107, 2010

Multi-band transit observations of the TrES-2b exoplanet

D. Mislis[1], S, Schröter[1], J.H.M.M. Schmitt[1], O. Cordes[2], & K. Reif[2]

[1]Hamburger Sternwarte, Gojenbergsweg 112, D-21029 Hamburg, Germany
email : mdimitri@hs.uni-hamburg.de
[2]Argelander-Institut für Astronomie, Auf dem Hügel 71, 53121 Bonn, Germany

Accepted : 14 December 2009

ABSTRACT

We present a new data set of transit observations of the TrES-2b exoplanet taken in spring 2009, using the 1.2m Oskar-Lühning telescope (OLT) of Hamburg Observatory and the 2.2m telescope at Calar Alto Observatory using BUSCA (Bonn University Simultaneous CAmera). Both the new OLT data, taken with the same instrumental setup as our data taken in 2008, as well as the simultaneously recorded multicolor BUSCA data confirm the low inclination values reported previously, and in fact suggest that the TrES-2b exoplanet has already passed the first inclination threshold ($i_{min,1} = 83.417°$) and is not eclipsing the full stellar surface any longer. Using the multi-band BUSCA data we demonstrate that the multicolor light curves can be consistently fitted with a given set of limb darkening coefficients without the need to adjust these coefficients, and further, we can demonstrate that wavelength dependent stellar radius changes must be small as expected from theory. Our new observations provide further evidence for a change of the orbit inclination of the transiting extrasolar planet TrES-2b reported previously. We examine in detail possible causes for this inclination change and argue that the observed change should be interpreted as nodal regression. While the assumption of an oblate host star requires an unreasonably large second harmonic coefficient, the existence of a third body in the form of an additional planet would provide a very natural explanation for the observed secular orbit change. Given the lack of clearly observed short-term variations of transit timing and our observed secular nodal regression rate, we predict a period between approximately 50 and 100 days for a putative perturbing planet of Jovian mass. Such an object should be detectable with present-day radial velocity (RV) techniques, but would escape detection through transit timing variations.

Keywords Stars : planetary systems – Techniques : photometry

3.1 Introduction

As of now more than 400 extrasolar planets have been detected around solar-like stars. In quite a few cases several planets have been detected to orbit a given star, demonstrating the existence of extrasolar planet systems in analogy to our solar system. Just as the planets in our solar system interact gravitationally, the same must apply to extrasolar planet systems. Gravitational interactions are important for the understanding of the long-term dynamical stability of planetary systems. The solar system has been around for more than four billion years, and the understanding of its dynamical stability over that period of time is still a challenge Simon et. al. (1994). In analogy, extrasolar planet systems must be dynamically stable over similarly long time scales, and most stability studies of extrasolar planet systems have been directed towards an understanding of exactly those long time scales. Less attention has been paid to secular and short-term perturbations of the orbit, since such effects are quite difficult to detect observationally. Miralda-Escudé (2002) gives a detailed discussion on what secular effects might be derivable from extrasolar planet transits; in spectroscopic binaries the orbit inclination i can only be deduced in conjunction with the companion mass, and therefore the detection of an orbit inclination change is virtually impossible. Short-term Transit timing variations (TTVs) have been studied by a number of authors (Holman & Murray 2005; Agol et. al. 2005), however, a detection of such effects has remained elusive so far. In principle, a detection of orbit change would be extremely interesting since it would open up entirely new diagnostic possibilities of the masses and orbit geometries of these systems; also, in analogy to the discovery of Neptune, new planets could in fact be indirectly detected.

The lightcurve of a transiting extrasolar planet with known period allows very accurate determinations of the radii of star and planet (relative to the semi-major axis) and the inclination of the orbital plane of the planet with respect to the line of sight towards the observer. Clearly, one does not expect the sizes of host star and planet to vary on short time scales, however, the presence of a third body can change the orientation of the orbit plane and, hence, lead to a change in the observed inclination with respect to the celestial plane. The TrES-2 exoplanet is particularly interesting in this context. It orbits its host star once in 2.47 days, which itself is very much solar-like with parameters consistent with solar parameters; its age is considerable and, correspondingly, the star rotates quite slowly. Its close-in planet with a size of 1.2 $\mathrm{R_{Jup}}$ is among the most massive known transiting extrasolar planets (Holman et. al. 2007; Sozzetti et. al. 2007).

What makes the TrES-2 exoplanet orbits even more interesting, is the fact that an apparent inclination change has been reported by some of us in a previous paper (Mislis & Schmitt (2009) henceforth called Paper I). The authors carefully measured several transits observed in 2006 and 2008. Assuming a circular orbit with constant period P, the duration of an extrasolar planet transit in front of its host star depends only on the stellar and planetary radii, R_s and R_p, and on the inclination i of the orbit plane w.r.t. the sky plane. A linear best fit to the currently available inclination measurements yields an apparent inclination decrease of 5.1×10^{-4} deg/day. The transit modeling both by Holman et. al. (2007) and Mislis & Schmitt (2009) shows the transit of TrES-2b in front of its host star to be “grazing”. In fact, according to the latest modeling the planet occults only a portion of the host star and transits are expected to disappear in the time frame 2020 – 2025, if the observed linear trend continues. This “grazing” viewing geometry is particularly suitable for the detection of orbital changes, since relatively small changes in apparent inclination translate into relatively large changes in eclipse duration. At the same time, a search for possible TTVs by Rabus et. al. (2009) has been negative; while Rabus et. al. (2009) derive a period wobble of 57 sec for TrES-2, the statistical quality of their data is such that no unique periods for TTVs can be identified.

The purpose of this paper is to present new transit observations of the TrES-2 exoplanet system obtained in 2009, which are described in the first part (Sec.3.2) and analysed (Sec. 3.3). In the second part (Sec.3.4) of our paper we present a quantitatively analysis of what kind of gravitational effects can be responsible for the observed orbit changes of TrES-2b and are consistent with all observational data of the TrES-2

Table 3.1: Observation summary

Date	*Instrument*	*Filter*	*Airmass*	*Seeing*
11/04/2009	*OLT*	I	1.7877 – 1.0712	2.94”
28/05/2009	*BUSCA*	v, b, y, I	1.8827 – 1.0453	3.09”

system.

3.2 Observations and data reduction

We observed two transits of TrES-2 using the ephemeris suggested by O’Donovan et. al. (2006) and by Holman et. al. (2007) from $T_c(E) = 2,453,957.6358[HJD] + E \cdot$ (2.47063 days), using the 1.2m Oskar Lühning telescope (OLT) at Hamburg Observatory and Calar Alto Observatory 2.2m telescope with BUSCA.

The OLT data were taken on 11 April 2009 using a $3Kx3K$ CCD with a $10'x10'$ FOV and an I-band filter as in our previous observing run (Paper I). The readout noise and the gain were 16.37 e^- and 1.33 e^-/ADU respectively. With the OLT we used 60-second exposures which provided an effective time resolution of 1.17 minutes. During the observation, the airmass value ranged from 1.7877 to 1.0712 and the seeing was typically 2.94”.

The Calar Alto data were taken on 28 May 2009 using BUSCA and the 2.2m telescope. BUSCA is designed to perform simultaneous observations in four individual bands with a FOV of $11'x11'$. Therefore it has four individual $4Kx4K$ CCD systems which cover the ultra-violet, the blue-green, the yellow-red and the near-infrared part of the spectrum (channel a-d respectively). For this run we used the Strömgren filters v (chn. a), b (chn. b), and y (chn. c) , and a Cousins-I filter for the near-infrared (chn. d). The readout-noise for these four detectors are $9.09e^-$, $3.50e^-$, $3.72e^-$, and $3.86e^-$ respectively for the a,b,c, and d channels. The gain values for the same channels are $1.347e^-/ADU$, $1.761e^-/ADU$, $1.733e^-/ADU$, and $1.731e^-/ADU$ respectively. The airmass value ranged from 1.8827 to 1.0453 and the seeing was 3.09”. For the BUSCA observations we took 30 seconds exposure yielding an effective time resolution of 1.63 minutes. In Table 3.1 we summarize the relevant observation details.

For the data reduction, we used *Starlink* and *DaoPhot* software routines, and the *MATCH* code. We perform the normal reduction tasks, bias subtraction, dark correction, and flat fielding on the individual data sets before applying aperture photometry on on all images. For TrES-2, we selected the aperture photometry mode using apertures centered on the target star, check stars, and sky background. Typical sky brightness values for the 11 April and for the 28 May were 89 and 98 ADUs, respectively, i.e., values at a level 0.008% and 0.006% of the star’s flux, respectively (for I-filter). For the relative photometry we used the star U1350-10220179 as a reference star to test and calibrate the light curve. For the data analysis presented in this paper we did not use additional check stars, but note that we already checked this star for constancy in the Paper I. To estimate the magnitude errors, we followed Howell Everett (2001) and the same procedure as described in our first paper (Paper I) to obtain better relative results. Our final relative photometry is presented in Table 3.2, which is available in its entirety in machine-readable form in the electronic version of this paper.

Table 3.2: Relative Photometry data.

HJD	*Relative Flux*	*Uncertainty*	*Flag*
2454933.44031	0.99172	0.0037	$OLT - I$
2454933.44091	0.99204	0.0038	$OLT - I$
2454933.44221	1.00514	0.0039	$OLT - I$
2454933.44281	1.00314	0.0038	$OLT - I$
2454933.44341	0.99458	0.0035	$OLT - I$
2454933.44401	0.99745	0.0037	$OLT - I$

Note : Table 3.2: Relative photometry vs. time; note that the complete table is available only electronically. The time stamps refer to the Heliocentric Julian Date (HJD) at the middle of each exposure. The 'Flag' column refers to the telescope and filter.

3.3 Model analysis and results

In our model analysis we proceeded in exactly the same fashion as described in Paper I. Note that the assumption of circularity appears to apply very well to TrES-2b (O'Donovan et. al. 2009; O'Donovan et. al. 2006); the assumption of constant period and hence constant semi-major axis will be adressed in section 4. For our modelling we specifically assumed the values $R_s = 1.003R_o$, $R_p = 1.222\ R_J$, $P = 2.470621$ days, $\alpha = 0.0367$ AU for the radii of star and planet, their period and the orbit radius respectively. All limb darkening coefficients were taken from Claret (2004), and for the OLT data we used the same values as in Paper I, viz., $u_1 = 0.318$ and $u_2 = 0.295$ for the I filter, as denoted by S1 in Table 3.3.

3.3.1 OLT data & modeling

Our new OLT data from 11 April 2009 were taken with the same instrumental setup as our previous data taken on 18 September 2008. The final transit light curve with the best fit model is shown in Fig.3.1, the reduced light curve data are provided in Table 3.1. Keeping the planetary and stellar radii and the limb darkening coefficients fixed (at the above values), we determine the best fit inclination and the central transit time T_c with our transit model using the χ^2 method; the thus obtained fit results are listed in Table 3.3. The errors in the derived fit parameters are assessed with a bootstrap method explained in detail in Paper I, however, we do not use random residuals for the new model, but we circularly shift the residuals after the model substraction to produce new light curves for the bootstrapped data following Alonso et. al. (2008). In Table 3.3 we also provide corrected central times and errors for those transists already reported in paper I, since due to some typos and mistakes the numbers quoted for central time and their error are unreliable (five first lines of Table 3.3). In Fig. 3.3 we plot the thus obtained inclination angle distribution for epoch April 2009 (solid curve) compared to that obtained in September 2008 (dashed curve). While the best fit inclination of $i = 83.38°$ differs from that measured in September 2008 ($i = 83.42°$), the errors are clearly so large that we cannot claim a reduction in inclination from our OLT data (taken with the same instrumental setup, i.e, in September 2008 and April 2009) alone, however, is clearly consistent with such a reduction.

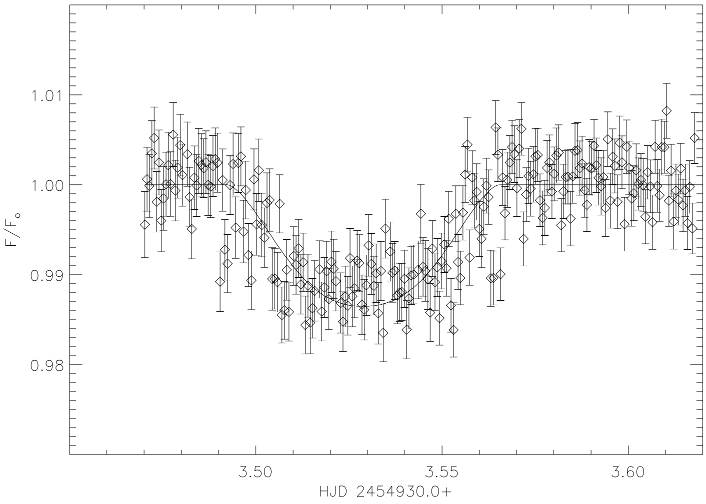

Figure 3.1: Observed TrES-2 light curves and model fits for the light curve taken with the 1.2m OLT at Hamburg Observatory taken in April 2009.

3.3.2 BUSCA data and modeling

Our BUSCA data have the great advantage of providing simultaneously measured multicolor data, which allows us to demonstrate that limb darkening is correctly modelled and does not affect the fitted inclinations and stellar radii. The limb darkening coefficients used for the analysis of the BUSCA data were also taken from Claret (2004); we specifically used u_1 = 0.318 and u_2 = 0.295 for the I filter (S1), i.e., the same values as for the OLT, u_1 = 0.4501 and u_2 = 0.286 for the y filter (S2), u_1 = 0.5758 and u_2 = 0.235 for the b filter (S3), u_1 = 0.7371 and u_2 = 0.1117 for the v filter (S4) respectively. The data reduction and analysis was performed in exactly the same fashion as for the OLT data, we also used the same comparison star U1350-10220179; the reduced light curve data are also provided in Table 3.2. The modelling of multicolor data for extrasolar planet transits needs some explanation. In our modelling the host star's radius is assumed to be wavelength independent. Since stars do not have solid surfaces, the question arises how much the stellar radius R_* does actually change with the wavelength. This issue has been extensively studied in the solar context, where the limb of the Sun can be directly observed as a function of wavelength (Neckel 1995). Basically the photospheric height at an optical depth of unity is determined by the ratio between pressure and the absorption coefficient, and for the Sun, Neckel (1995) derives a maximal radius change of 0.12 arcsec between 3000 and 10000 Å, which corresponds to about 100 km. If we assume similar photospheric parameters in the TrES-2 host star, which appears reasonable since TrES-2 is a G0V star, we deduce a wavelength-dependent radius change on the order of 100 km, which is far below a percent of the planetary radius and thus not detectable. Therefore in our multi-band data modelling we can safely fix the radius of the star and the radius of the planet in a wavelength-independent fashion.

We thus kept the stellar and planetary fixed at the above values, treated all BUSCA channels as independent observations and fitted the light curves – as usual – by adjust-

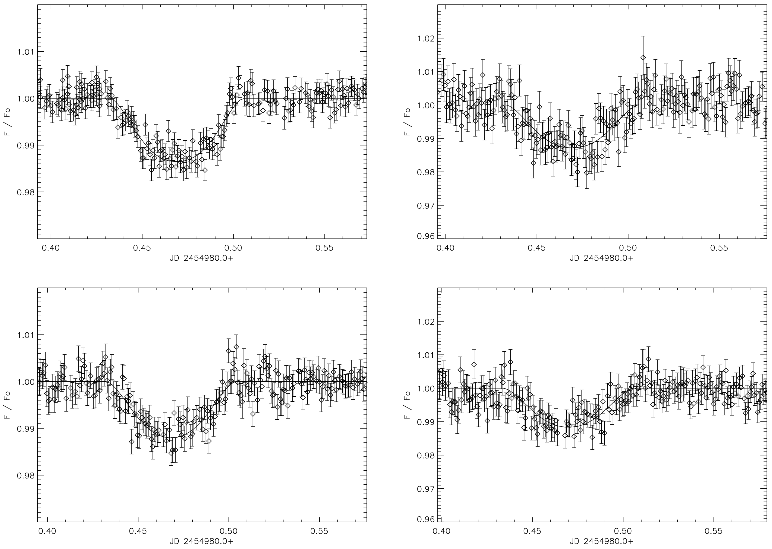

Figure 3.2: Four light curves and corresponding model fits taken in May 2009 with the 2.2m telescope at Calar Alto using BUSCA.

ing inclination and central transit time. The filter light curves are shown together with the so obtained model fits in Fig. 3.2, the model fit parameters are again summarized in Table 3.3. We emphasize that we obtain good and consistent fits for all light curves with the chosen set of limb darkening coefficients, thus demonstrating our capability to correctly model multicolor light curves.

Since the BUSCA data are recorded simultaneously, it is clear that the light curves in the four BUSCA channels must actually be described by the same values of inclination and transit duration. We therefore simultaneously fit all the four light curves, leaving free as fit parameters only the central time T_c and inclination i. With this approach we find an average inclination of $i = 83.36° \pm 0.03°$, which is consistent with our spring OLT data and also suggests that the inclination in spring 2009 has further decreased as compared to our 2008 data.

3.3.3 Joint modeling

Using all our data we can check whether our assumption of the wavelength-independence of the radius is consistent with the observations. For this consistency test we kept the inclination value fixed at $i = 83.36°$ and fitted only the radius of the star R_s and T_c. The errors on R_s were again assessed by a Monte Carlo simulation as described in Paper I and the distribution of the thus derived stellar radius values R_s is shown in Fig. 3.4; as apparent from Fig. 3.4, all BUSCA channels are consistent with the same stellar radius as – of course – expected from theory since any pulsations of a main-sequence star are not expected to lead to any observable radius changes.

The crucial issue about the TrES-2 exoplanet is of course the constancy or variability of its orbit inclination. Our new BUSCA and OLT data clearly support a further decrease in orbit inclination and hence decrease in transit duration. In order to demonstrate the magnitude of the effect, we performed one more sequence of fits, this time

Table 3.3: Individual values of duration, inclination, χ^2 values and limb darkening coefficients from five light curve fits; units for duration and errors are minutes and for inclination and errors are degrees. The OLT light curve has 268 points, the I-filter light curve has 198, the y-filter light curve has 208, the b-filter light curve 198 and the v-filter light curve 162 points respectively.

Tc time $[HJD]$	*Duration*	*Errors*	*Inclin.*	*Errors*	χ^2*value*	*LDL*
3989.7529 ± 0.00069	110.308	0.432	83.59	0.019	432.1	
3994.6939 ± 0.00066	109.230	0.448	83.56	0.019	296.8	
4041.6358 ± 0.00070	109.025	0.430	83.55	0.019	290.6	
4607.4036 ± 0.00072	106.620	0.883	83.44	0.036	179.1	
4728.4640 ± 0.00071	106.112	0.870	83.43	0.036	190.1	
4933.5274 ± 0.00076	105.077	0.964	83.38	0.039	296.1	$S1$
4980.4675 ± 0.00068	105.056	0.848	83.38	0.034	181.7	$S1$
4980.4679 ± 0.00090	104.748	1.076	83.37	0.043	202.2	$S2$
4980.4667 ± 0.00082	103.832	1.021	83.33	0.041	186.0	$S3$
4980.4678 ± 0.00100	104.363	1.194	83.35	0.048	195.0	$S4$
4980.4675 ± 0.00060	104.522		83.36	0.030		

Table 3.4: χ^2 tests for two different inclination values and the χ^2 errors after 1000 Monte Carlo simulations.

Inclination [°]	*OLT*	$B-I$	$B-y$	$B-b$	$B-v$
83.57 (*Holman*)	304.9	199.4	207.8	216.0	206.3
σ_{χ^2} (*Holman*)	16.12	14.04	16.16	21.05	14.26
83.36 (*this paper*)	213.8	173.44	164.3	180.0	131.1
σ_{χ^2} (*this paper*)	11.96	11.11	9.96	12.01	8.77

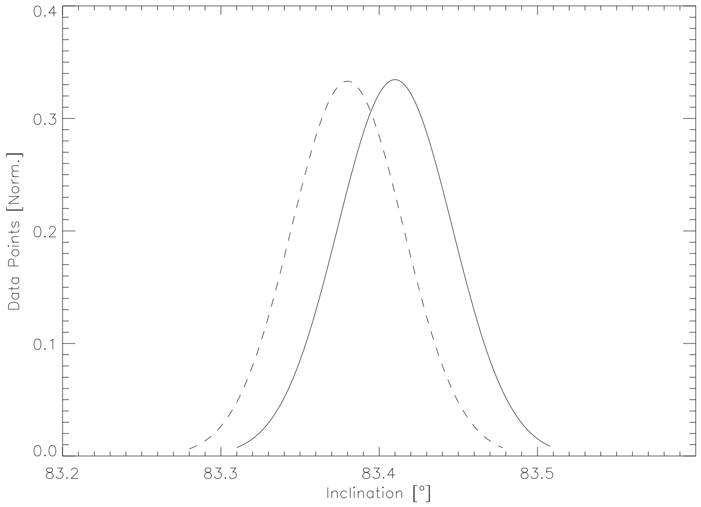

Figure 3.3: Inclination distribution for the OLT data using 1000 Monte Carlo simulations for the September 2008 (solid curve) and April 2009 (dashed curve); see the text for details.

keeping all physical parameters fixed and fitting only the central transit times T_c using 1000 Monte Carlo realisations and studying the resulting distribution in χ^2; for the inclination we assumed for, first, the value $i = 83.57°$ (as derived by Holman et al. for their 2006 data) and the value $i = 83.36°$ (this paper for the 2009 data). The fit results (in terms of obtained χ^2 values) are summarised ed in Tab. 3.4, which shows that for all (independent) data sets the lower inclination values yield smaller χ^2-values; for some filter pairs the thus obtained improvement is extremely significant.

3.3.4 Inclination changes

In Fig. 3.6 we plot all our current inclination vs. epoch data together with a linear fit to all data; a formal regression analysis yields for the time evolution of the inclination ($i = i_o + a \cdot (Epoch)$, $i_o = 83.5778$, $a = 0.00051$). In Paper I we noted the inclination decrease and predicted inclination values below the first transit threshold ($i_{min,1} < 83.417°$) after October 2008. Both the new OLT data set and all BUSCA channel observations yield inclinations below the first transit threshold. While the error in a given transit light curve is typically on the order of 0.04° for i, we consider it quite unlikely that 5 independent measurements all yield only downward excursions. We therefore consider the decrease in inclination between fall 2008 and spring 2009 as significant, conclude that the inclination in the TrES-2 system is very likely below the first transit threshold, and predict the inclinations to decrease further; also, the transit depths should become more and more shallow since the exoplanet eclipses less and less stellar surface.

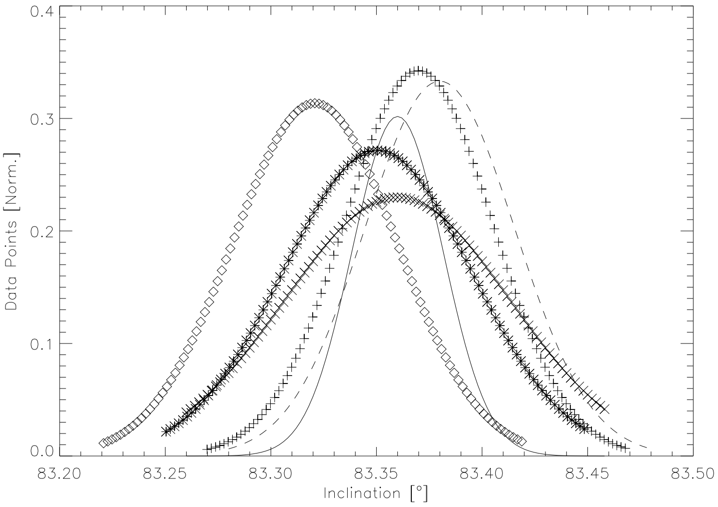

Figure 3.4: Inclination distribution derived 1000 Monte Carlo simulations for the multi-band BUSCA observations data in the I (crosses), y (stars), b (diamonds) and v (x-symbol) filter bands; the mean inclination distribution from the four BUSCA lightcurves is shown as solid line, the inclination distribution derived from the OLT data taken in April 2009 is also shown for comparison (dashed line).

3.3.5 Period changes

The observed change in orbit inclination is in marked contrast to the period of TrES-2b. While possible TTVs in TrES-2b have been studied by Rabus et. al. (2009) we investigate the long-term stability of the period of TrES-2b. From our seven transit measurements (plus five more data points of Rabus et. al. 2009) spanning about ~ 400 eclipses we created a new O-C diagram (cf., Fig. 3.7); note that we refrained from using the transit times dicussed by Raetz et. al. (2009), since these transits were taken with rather inhomogeneous instruments and sometimes only partial transit coverage. For our fit we used a modified epoch equation $HJD_c = HJD_o + E \cdot P$, where we set $P = P_o + \dot{P}(t - HJD_o)$ and explicitly allow a non-constant period P. We apply a χ^2 fit to find the best fit values for $\dot{P}$, P_o, and HJD_o. With this approach we find a best fit period change of $\dot{P} = 5 \times 10^{-9}$, however, carrying out the same analysis keeping a fixed period shows that the fit improvement due to the introduction of a non-zero $\dot{P}$ is insignificant. We then find as best fit values $P_o = 2.47061$ and $HJD_o = 2453957.6350$ conforming to the values derived by Rabus et. al. (2009). Thus, the period of TrES-2b is constant, and any possible period change over the last three years must be less than about 1 sec.

3.4 Theoretical implications of observed inclination change

The results of our data presented in the preceding sections strenghten our confidence that the observed inclination changes do in fact correspond to a real physi-

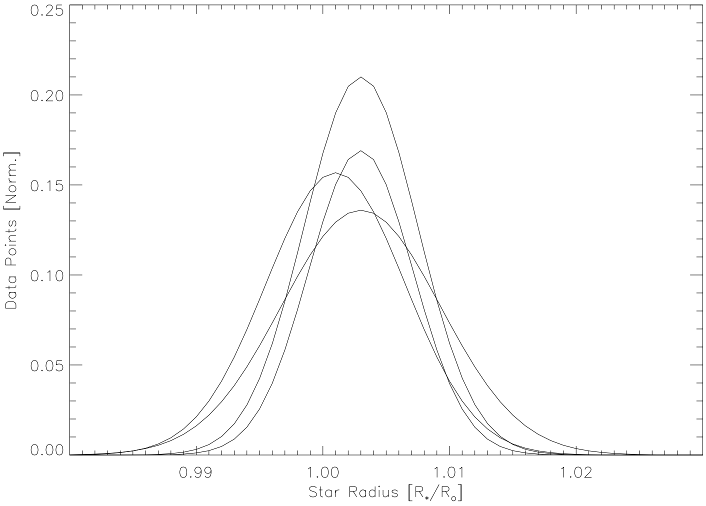

Figure 3.5: Stellar Radius distribution (R_*), derived from 1000 Monte Carlo simulations in four different filters (from higher to lower peak, I, y, b and v filter respectively). The overlap of the curves shows that all colors can be explained with the same stellar radius as suggested by theory (see Neckel 1995).

cal phenomenon. Assuming now the reality of the observed inclination change of $\Delta i \sim 0.075^\circ/\mathrm{yr}$, given the constancy of the period and the absence of TTVs at a level of $\approx$100 sec we discuss in the following a physical scenario consistent with these observational findings. We specifically argue that the apparent inclination change should be interpreted as a nodal regression and then proceed to examine an oblate host star and the existence of an additional perturbing object in the system as possible causes for the change of the orbital parameters of Tres-2b.

3.4.1 Inclination change or nodal regression?

It is important to realize that the reported apparent change of inclination refers to the orientation of the TrES-2 orbit plane with respect to the observer's tangential plane. It is well known that the z-component of angular momentum for orbits in an azimuthally symmetric potential is constant, resulting in a constant value of inclination. An oblate star (cf., Sec. 3.4.2) or the averaged potential of a third body (cf., Sec. 3.4.3) naturally lead to such potentials, thus yielding orbits precessing at (more or less) constant inclination as also realized by Miralda-Escudé (2002). Such a precession would cause an apparent inclination change, however, physically this would have to be interpreted as nodal regression at fixed orbit inclination. To interpret the observations, one has to relate the rate of nodal regression to the rate of apparent inclination change.

Consider a (massless) planet of radius R_p orbiting a star of radius R_* at some distance d. Let the planet's orbit lie in a plane with a fixed inclination i relative to the x-y plane, which we take as invariant plane. Let an observer be located in the x-z plane with some elevation γ, reckoned from the positive x-axis. The line of the ascending node in the x-y plane is denoted by the angle Ω, with $\Omega = 0$ implying the ascending node pointed along the negative y-axis (see Fig. 3.8). Let in the thus defined geometry

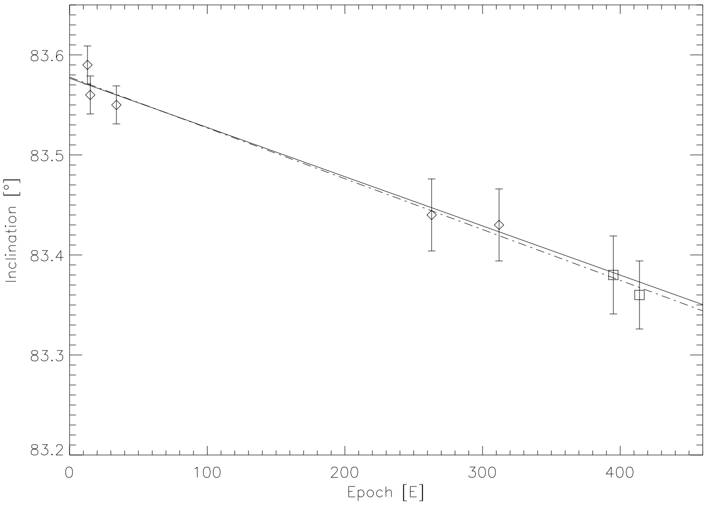

Figure 3.6: Epoch versus inclination together with a linear fit to the currently available data; the diamond points are those taken in 2006 by Holman et. al. (2007), and those taken in 2008 and reported in Paper I. The square points are derived from our new observations taken in April and May 2009. The solid lines showing two linear fits, from the first paper (dashed line) and the fit from the present paper (solid line).

the angle Ψ denote the angle between planet and observer as seen from the central star. For each system configuration defined by the angles (γ, i, Ω) there is a minimal angle Ψ_{min} between orbit normal and observer obtained in each planetary orbit, which can be computed from

$$\cos\Psi_{\mathrm{min}} = \vec{n}_{\mathrm{Orbit}} \cdot \vec{r}_{\mathrm{Observer}} = -\cos\gamma \sin i \cos\Omega + \sin\gamma \cos i. \tag{3.1}$$

A transit takes place when

$$|\cos\Psi_{\mathrm{min}}| \leq (R_p + R_*)/d, \tag{3.2}$$

and from the geometry it is clear that the observed inclination i_{obs}, i.e., the parameter that can be derived from a transit light curve is identical to Ψ_{min}. Setting then $\Psi_{\mathrm{min}} = i_{\mathrm{obs}}$ and differentiating Eq. 3.1 with respect to time we obtain

$$\frac{\mathrm{d}i_{\mathrm{obs}}}{\mathrm{d}t} = -\frac{\sin\Omega \cos\gamma \sin i}{\sin i_{\mathrm{obs}}} \frac{\mathrm{d}\Omega}{\mathrm{d}t}. \tag{3.3}$$

Eq. 3.3 relates the nodal regression of the orbit to its corresponding observed apparent rate of inclination change $\mathrm{d}i_{\mathrm{obs}}/\mathrm{d}t$, given the fixed inclination i relative to the x-y plane. Since transit observations yield very precise values of i_{obs}, the required ascending node Ω and its rate of change can be computed, once the orbit geometry through the angles γ and i_{obs} is specified. In Fig. 3.9 we show a contour plot of the linear coefficient of Eq. 3.3 between nodal regression and observed inclination change as a function of orbit geometry. Note that the apparent change of inclination due to the nodal regression does vanish for $i = 0$. Physically it is clear that a perturbing planet in a coplanar orbit cannot exercise a torque and therefore cannot cause the observed inclination variation. We will therefore always assume $i \neq 0$ in the following.

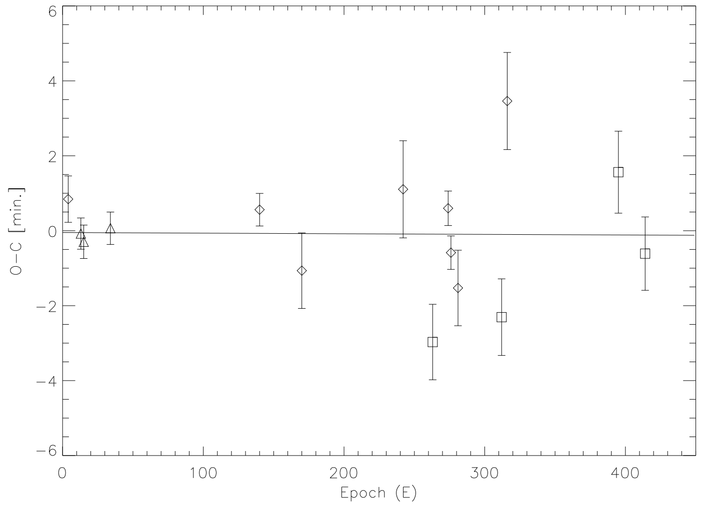

Figure 3.7: O-C values versus epoch including the transits observed by Holman et al., Rabus et al. and our data denoted by triangles, squares and diamonds respectively.

3.4.2 Oblate host star

We first consider the possibility that the TrES-2 host star is oblate. The motion of a planet around an oblate host star is equivalent to that of an artifical satellite orbiting the Earth, a problem intensely studied over the last decades and well understood Connon Smith (2005). The potential $U(r, \phi)$ of an axisymmetric body of mass M and radius R can be expressed as a power series involving the so-called harmonic coefficients. In second order one approximates the potential $U(r, \phi)$ as

$$U(r, \phi) = \frac{GM}{r}\left[1 - J_2\left(\frac{R}{r}\right)^2 \frac{1}{2}\left(3\sin^2\phi - 1\right)\right], \tag{3.4}$$

where r is the radial distance from the body's center, ϕ is latitude above the equator and G denotes the gravitational constant.

Clearly, the perturbing term in the potential is proportional to J_2 and a perturbation calculation yields as first order secular perturbation the angular velocity of the ascending node as

$$\frac{\mathrm{d}\Omega}{\mathrm{d}t} = -\frac{3}{2}\frac{J_2R^2}{(1-e^2)^2}\cos i\left(\frac{2\pi}{P}\right)^{7/3}\frac{1}{(GM_{\mathrm{total}})^{2/3}}, \tag{3.5}$$

where e and i denote the eccentricity and inclination of the orbiting body, P its period, M_{total} the sum of the masses of planet and host star and the validity of Kepler's third law has been assumed.

Interpreting the observed inclination change as nodal regression due to an oblate host star, we can compute a lower bound on the required harmonic coefficient J_2 assuming $e = 0$. Therefore, we combine Eqs. 3.3 and 3.5 to obtain an expression for J_2. Excluding pathological cases like $i, \Omega = 0$ and $\gamma = \pi/2$ and neglecting the planetary

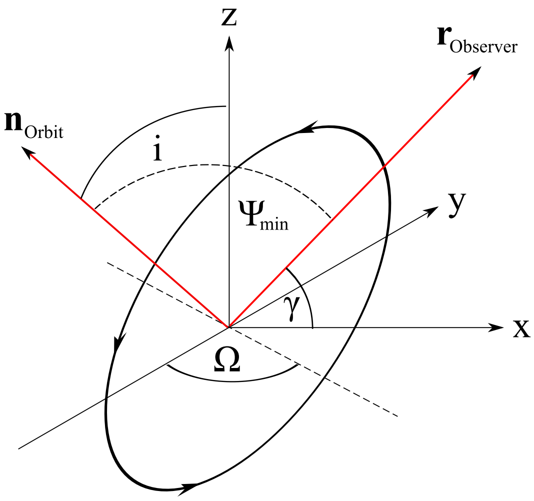

Figure 3.8: System geometry (see text for details): The orbit plane with normal vector $\vec{n}_{\rm Orbit}$ is inclined relative to the x-y plane by an inclination i, the observer (towards $\vec{r}_{\rm Observer}$) is within the x-z plane.

mass in Eq. 3.5 we find for any given set of parameters (Ω, γ, i)

$$J_2 \geq J_2^{\rm min} = \frac{2}{3}\frac{{\rm d}i_{\rm obs}}{{\rm d}t}\left(\frac{P}{2\pi}\right)^{7/3}\frac{(GM_{\rm host})^{2/3}}{R^2}\sin i_{\rm obs}, \tag{3.6}$$

where $M_{\rm host}$ denotes the mass of the host star. Mass, radius, inclination and period of the TrES-2 system are well known, and using the measured nodal regression we find $J_{2,{\rm TrES-2}} \approx 1.4 \times 10^{-4}$, i.e., a value smaller than that of the Earth ($J_{2,\oplus} = 0.00108$) by an order of magnitude, but considerably larger than that of the Sun, which is usually taken as $J_{2,\odot} \approx 3 - 6 \times 10^{-7}$ Rozelot et. al. (2001). Since the host star of TrES-2 is a slow rotator very similar to the Sun Sozzetti et. al. (2007), we expect similarly small J_2 values in contrast to our requirements. We therefore conclude that oblateness of the host star cannot be the cause for the observed orbit variations.

3.4.3 Perturbation by a third body

An alternative possibility to explain the observed orbit variations of the TrES-2 exoplanet would be the interaction with other planets in the system. Let us therefore assume the existence of such an additional perturbing planet of mass m_p, circling its host star of mass m_0 with period P_p at distance r_p located further out compared to the known transiting TrES-2 exoplanet. This three-body problem has been considered in past in the context of triple systems (Khaliullin et. al. 1991; Li 2006) and the problem of artificial Earth satellites, whose orbits are perturbed by the Moon. In lowest order, the perturbing gravitational potential R_2 onto the inner planet with mass m and distance r is given by the expression

$$R_2 = \frac{m_p}{m_p + m_o}\left(\frac{2\pi a}{P_p}\right)^2\left(\frac{a_p}{r_p}\right)^3\left(\frac{r}{a}\right)^2\frac{3\cos^2 S - 1}{2}, \tag{3.7}$$

where the angle S denotes the elongation between the perturbed and perturbing planet as seen from the host star, a and a_p denote their respective semi-major axes and the va-

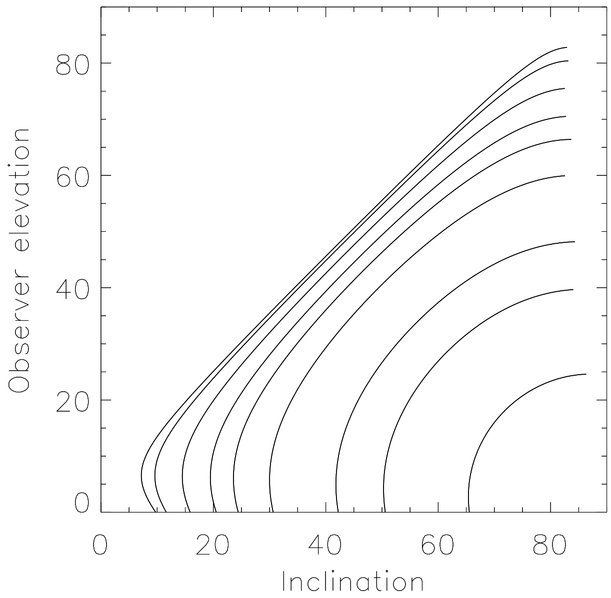

Figure 3.9: Linear coefficient of Eq. 3.3 between nodal regression and observed inclination change as a function of view geometry (cf., Eq. 3.3), computed for $i_{\rm obs} = 83.38°$ as applicable for TrES-2; the plotted contour levels denote values of 1.1, 1.3, 1.5, 2., 2.5, 5.,4.,6.,8. from right bottom up.

lidity of Kepler's third law has been assumed. Note that in this approach the perturbed body is assumed to be massless, implying that its perturbations onto the perturbing body are ignored. Next one needs to insert the orbital elements of the two bodies and, since we are interested only in secular variations, average over both the periods of the perturbed and perturbing planet. This is the so-called double-averaging method (Broucke 2003), which, however, in more or less the same form has also been applied by Li (2006) and Kovalevsky (1967). Denoting by e the eccentricity of the perturbed planet, by ω the longitude of the periastron and by i the angle between the two orbital planes, one obtains after some lengthy computation (see Kovalevsky 1967)

$$R_2 = \frac{m_p}{m_p + m_o} \left(\frac{\pi a}{2P_p}\right)^2 \times K_0(i, e, \omega), \tag{3.8}$$

with the auxiliary function $K_0(i, e, \omega)$ given by

$$K_0(e, i, \omega) = \left(6\cos^2 i - 2\right) + e^2\left(9\cos^2 i - 3\right) + 15e^2 \sin^2 i \cos 2\omega.$$

The partial derivatives of R_2 with respect to the orbital elements are needed in the so-called Lagrangian planetary equations to derive the variations of the orbital elements of the perturbed body. One specifically finds for the motion of the ascending node

$$\frac{\mathrm{d}\Omega}{\mathrm{d}t} = \frac{m_p}{m_p + m_o} \frac{3\pi}{4} \frac{P}{P_p^2} \frac{\cos i}{\sqrt{1 - e^2}} \times K_1(e, \omega), \tag{3.9}$$

where the auxiliary function $K_1(e, \omega)$ is defined through

$$K_1(e, \omega) = 5e^2 \cos 2\omega - 3e^2 - 2 \tag{3.10}$$

and for the rate of change of inclination

$$\frac{\mathrm{d}i}{\mathrm{d}t} = -e^2 \frac{m_p}{m_p + m_o} \frac{15\pi}{8} \frac{P}{P_p^2} \frac{1}{\sqrt{1-e^2}} \sin(2i) \sin(2\omega). \tag{3.11}$$

As is obvious from Eq. 3.11, the rate of change of inclination in low eccentricity systems is very small and we therefore set $e = 0$. Assuming next a near coplanar geometry, i.e., setting $\cos i \approx 1$, we can simplify Eq. 3.9 as

$$\frac{\mathrm{d}\Omega}{\mathrm{d}t} = -\frac{m_p}{m_p + m_o} \frac{3\pi}{2} \frac{P}{P_p^2}. \tag{3.12}$$

If we assume a host star mass and interpret the observed inclination change as the rate of nodal regression via Eq. 3.3, Eq. 3.12 relates the unknown planet mass m_p to its orbital period P_p.

Sanity check: Application to the Solar System

The use of Eq. 3.12 involves several simplifications. Thus, it is legitimate to ask, if we are justified in expecting Eq. 3.12 to describe reality. As a sanity check we apply Eq. 3.12 to our solar system. Consider first the motion of the Moon around the Earth, i.e., $P = 27.3$ d, which is perturbed by the Sun, i.e., $P_p = 365.25$ d. Since for that case our nomenclature requires $m_p \gg m_o$ and $i \sim 5.1°$, we find from Eq. 3.12 a time of 17.83 years for the nodes to complete a full circle, which agrees well with the canonical value of 18.6 years for the lunar orbit. In the lunar case it is clear that the Sun with its large mass and close proximity (compared to Jupiter) is by far the largest perturber of the Earth-Moon two-body system and this situation is exactly the situation described by theory.

Consider next the the perturbations caused by the outer planets of our solar system. Considering, for example, Venus, we can compute the perturbations caused by the planets Earth, Mars, Jupiter, Saturn and Uranus. Since the perturbation strength scales by the ratio $m_p P_p^{-2}$, we can set this value to unity for the Earth and compute values of 0.03, 2.26, 0.11 and 0.002 for Mars through Uranus respectively. So clearly, Venus is perturbed by several planets, but the perturbations by Jupiter are strongest. We therefore expect that our simple approach is not appropriate. We further note that among the outer solar system planets long period perturbations and resonances occur, which are not described by Eq. 3.12. If we nevertheless compute the nodal regression for Venus caused by Jupiter using Eq. 3.12, we find a nodal regression of 0.1°/cty for Venus, and 0.3°/cty for Mars. Using the orbital elements computed by Simon et. al. (1994) and calculating the nodal regressions of Venus and Mars in the orbit plane of Jupiter we find values smaller than the true values, but at least, they computed values in the right order of magnitude and do not lead to an overprediction of the expected effects.

Sanity check: Application to V 907 Sco

From archival studies Lacy et. al. (1999) report the existence of transient eclipses in the triple star V 907 Sco. According to Lacy et. al. (1999) this system is composed out of a short-period (P_{short} = 3.78 days) binary containing two main sequence stars of spectral type ~ A0 and mass ratio 0.9, orbited by a lower mass third companion (P_{long} = 99.3 days), of spectral type mid-K or possibly even a white dwarf. The close binary system showed eclipses from the earliest reported observations in 1899 until about 1918, when the eclipses stopped; eclipses reappeared in 1963 and were observed until about 1986. Interpreting the appearance of eclipses due to nodal regression, Lacy et. al. (1999) derive a nodal period of 68 years for V 907 Sco. Using Eq. 3.12 and assuming a mass of 2 $M_\odot$ for the host (m_o) and a mass of 0.5 $M_\odot$ for the companion (m_p), we compute a nodal regression period of 47.6 years, which agrees well with the nodal period estimated by Lacy et. al. (1999). We therefore conclude that Eq. 3.12 also provides a reasonable description of the transient eclipse observations of V 907 Sco.

Application to TrES 2

Applying now Eq. 3.12 to the TrES-2 exoplanet we express the period of the (unknown) perturbing planet as a function of its also unknown mass through

$$P_p = \sqrt{\frac{m_p}{m_p + m_o} \frac{3\pi P}{2} \frac{1}{\mathrm{d}\Omega/\mathrm{d}t}}. \tag{3.13}$$

Since the host star mass and the nodal regression are known, the perturbing mass is the only remaining unknown; we note that Eq. 3.13 should be correct, as long as there is only one dominant perturber in the system with a low-eccentricity orbit sufficiently far away from the known close-in transiting planet. In Fig. 3.10 we plot the expected perturber period P_p as a function of m_p (in Jupiter masses) for $m_o = 1\,M_\odot$ and the measured rate of nodal regression assuming a linear coefficient of unity in Eq. 3.3. Assuming *ad hoc* a mass of about one Jupiter mass for this perturber and taking into account that a factor of a few is likely (cf., Fig. 6.10), we find that periods of 50 to 100 days are required to explain the observed nodal regression in TrES-2. Such an additional planet should be relatively easily detectable with RV studies. Deamgen et. al (2009) report the presence of a faint companion about one arcsec away from TrES-2. Assuming this companion to be physical, a spectral type between K4.5 and K6, a mass of about 0.67 $M_\odot$ at a distance of 230 AU with a period of 3900 years follow. Computing with these numbers the maximally expected nodal regression from Eq. 3.12, one finds values a couple of orders of magnitude below the observed values. We thus conclude that this object cannot be the cause of the observed orbit variations. On the other hand, this companion, again if physical, makes TrES-2 particularly interesting because it provides another cases of a planet/planetary system in a binary system, and eventually the orbit planes of binary system and the planet(s) can be derived.

3.4.4 Transit timing variations by a putative perturber

A perturbing second planet capable of causing fast nodal precession on the transiting planet is also expected to induce short-term periodic variations of its orbital elements. In addition to the secular precession of the node of the orbit we would thus expect to see short-term transit timing variations (TTVs), periodic variations of the mid-transit times (Holman & Murray 2005; Agol et. al. 2005). Just as nodal regression, the TTV signal can be used to find and characterize planetary companions of transiting exoplanets. Rabus et. al. (2009) carefully analyzed eight transit light curves of TrES-2 over several years. However, they were unable to detect any statistically significant TTV amplitudes in the TrES-2b light curves above about 50 s; cf. their Fig. 3.11. Therefore, the existence of perturbing objects leading to TTVs on the scale of up to about 50 s are consistent with actual observations. Putting it differently, the orbital parameters

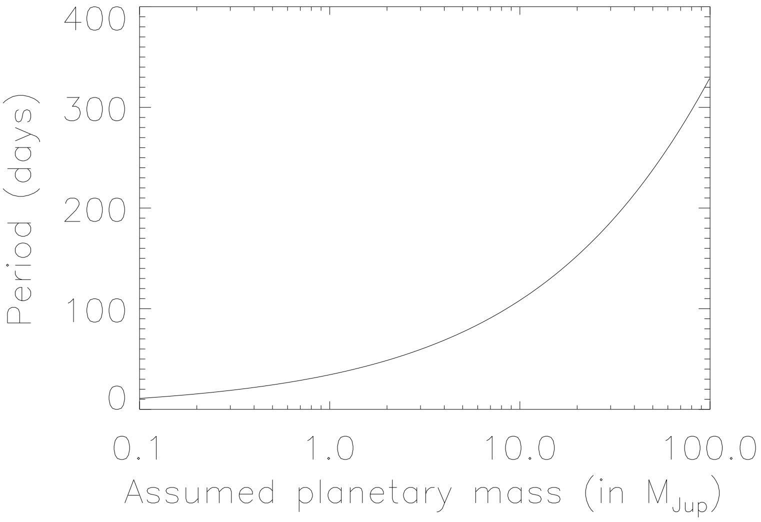

Figure 3.10: Period of hypothesized second planet vs. mass assuming a linear coefficient of unity in Eq. 3.3 and near coplanarity.

of any perturbing object causing the nodal precession of the orbit should yield a TTV amplitude below that and hence remain undetactable in the presently existing data.

To analyze the mutual gravitational influence of a perturbing second planet in the system on TrES-2, we have to treat the classical three-body problem of celestial mechanics. Instead of direct N-body integrations of the equations of motion we use an alternative method based on analytic perturbation theory developed and extensively tested by Nesvorný & Morbidelli (2008) and Nesvorný (2009). Outside possible mean-motion resonances their approach allows for a fast computation of the expected TTV amplitude given a combination of system parameters. As input we have to specify the orbital elements and masses of both planets. Consistent with the observations we assume TrES-2 to be in a circular orbit around its host star, while we allow for different eccentricities e_p and periods P_p of the perturber, which we assume to be of Jovian mass; since the TTV amplitudes scale nearly linearly with the perturber mass, we confine our treatment to $m_p = 1\ M_{\mathrm{Jup}}$; all other orbital elements are set to zero. This is justified as these parameters in most cases do not lead to a significant amplification of the TTV signal (see Nesvorný 2009, for a detailed discussion of the impact of these orbital elements). The resulting TTV amplitude for different reasonable orbit configurations (given the observed secular node regression as discussed above) of the system of P_{pert} = 30, 50 and 70 days is plotted vs. the assumed eccentricity in Fig. 3.11; the currently available upper limit to any TTV signal derived by Rabus et. al. (2009) is also shown. As is obvious from Fig. 3.11, a Jovian-mass perturber at a distance required to impose the observed secular changes (period of 50 – 100 days) leads to a TTV signal well below the current detection limit for all eccentricities e_p as long as $e_p \lesssim 0.4$. We therefore conclude that a putative perturbing Jovian-mass planet with a moderate eccentricity and with a period between 30 – 70 days would not yield any currently detectable TTV signal and would therefore be a valid explanation for the observed inclination change in the TrES-2 system.

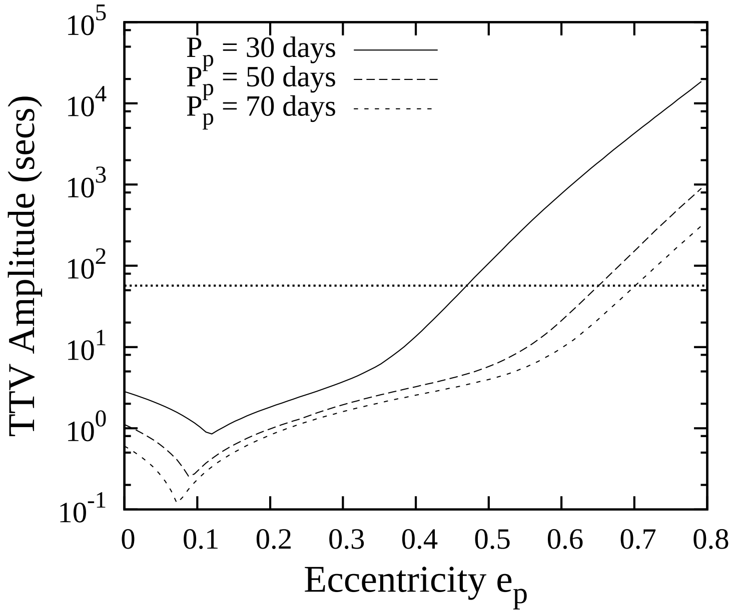

Figure 3.11: Amplitude of expected Transit Timing Variations (TTVs) in the TrES-2 system. The perturber is assumed to have $m_p = 1\ M_{\rm Jup}$. Its eccentricity e_p and period P_p are varied within plausible ranges. The orbit of TrES-2 is assumed to be circular. The vertical dotted line marks the best fitting TTV signal found by Rabus et. al. (2009) of 57 s.

3.5 Conclusions

In summary, our new observations taken in the spring of 2009 confirm the smaller transit durations reported in Paper I and suggest an even further decrease. With our simultaneously taken multicolor BUSCA data we demonstrate that the recorded multicolor lightcurves can be consistently modelled with a reasonable set of limb darkening coefficients, and that there is no need to fit the limb darkening coefficients to any particular light curve. An error in the description of the limb darkening therefore appears thus as an unlikely cause of the observed inclination changes. Also as expected, the obtained stellar radius is independent of the wavelength band used, demonstrating the internal self-consistency of our modelling.

As to the possible causes for the observed apparent orbit inclination change in TrES-2 we argue that the apparent observed inclination change is very likely caused by nodal regression. The assumption of an oblate host star leads to implausibly large J_2 coefficients, we therefore favor an explanation with a third body. We argue that Eq. 3.12 is a reasonable approximation for the interpration of the observed inclination changes; applying it to the TrES-2 system, we find that a planet of one Jovian mass with periods between $50 - 100$ days would suffice to cause the observed inclination changes, while at the same time yield TTVs with amplitudes well below the currently available upper limits.

The assumption of such an additional planet in the TrES-2 system is entirely plausible. First of all, if it is near coplanar with TrES-2b, it would not cause any eclipses and therefore remain undetected in transit searches. Next, an inspection of the exosolar planet data base maintained at *www.exoplanet.eu* reveals a number of exoplanet systems with properties similar to those postulated for TrES-2, i.e., a close-in planet together with a massive planet further out: In the Gl 581 system there is a 0.02 Jupiter-mass planet with a period of 66 days, and in fact a couple of similarly massive planets further in with periods of 3.1, 5.4 and 12.9 days respectively; in the system HIP 14810 there is a close-in planet with a 6.6 day period and a somewhat lighter planet with a period of 147 days, in the HD 160691 system the close-in planet has a period of 9.6 days and two outer planets with Jupiter masses are known with periods of 310 and 643 days. It is also clear that in these systems nodal regression changes must occur, unless these systems are exactly coplanar, which appears unlikely. Therefore on longer time scales the observed orbit inclination in these systems must change, but only in transiting systems the orbit inclination can be measured with sufficient accuracy. Because of its apparent inclination change TrES-2b is clearly among the more interesting extrasolar planets. If the system continues its behavior in the future the transits of TrES-2b will disappear. Fortunately, within the first data set of the Kepler mission ~ 30 transits should be covered. From our derived inclination change rate of $\Delta i \sim 0.075°/\mathrm{yr}$ this corresponds to an overall change of $\Delta i \sim 0.015°$ in this first data set, which ought to be detectable given the superior accuracy of the space-based Kepler photometry. As far as the detection of our putative second planet is concerned, RV methods appear to be more promising than a search for TTVs, unless the orbital eccentricities are very large.

3.6 Acknowledgements

The paper is based on observations collected with the 2.2 m telescope at the Centro Astronómico Hispano Alemán (CAHA) at Calar Alto (Almería, Spain), operated jointly by the Max-Planck Institut für Astronomie and the Instituto de Astrofísica de Andalucía (CSIC). The authors thank H.Poschmann and the BUSCA team for their tremendous work on the new controller and CCD system. DM was supported in the framework of the DFG-funded Research Training Group "Extrasolar Planets and their Host Stars" (DFG 1351/1). SS acknowledges DLR support through the grant 50OR0703.

3.7 References

Agol, E., Steffen, J., Sari, R., & Clarkson, W. 2005, MNRAS, 359, 567
Alonso, R., Barbieri, M., Rabus, M., et al. 2008, A& A, 487, L5
Broucke, R. A. 2003, Journal of Guidance Control Dynamics, 26, 27
Claret, A. 2004, A& A, 428, 1001
Connon Smith, R. 2005, The Observatory, 125, 341
Daemgen, S., Hormuth, F., Brandner, W., et al. 2009, A& A, 498, 567
Holman, M. J. & Murray, N. W. 2005, Science, 307, 1288
Holman, M. J., Winn, J. N., Latham, D. W., et al. 2007, ApJ, 664, 1185
Howell, S. B. & Everett, M. E. 2001, in Third Workshop on Photometry, p. 1, ed. W. J. Borucki & L. E. Lasher, 1
Khaliullin, K. F., Khodykin, S. A., & Zakharov, A. I. 1991, ApJ, 375, 314
Kovalevsky, J. 1967, in Les Nouvelles Mèthodes de la Dynamique Stellaire, 221
Lacy, C. H. S., Helt, B. E., & Vaz, L. P. R. 1999, AJ, 117, 541
Li, L. 2006, AJ, 131, 994

Miralda-Escudè, J. 2002, ApJ, 564, 60
Mislis, D. & Schmitt, J. H. M. M. 2009, A& A, 500, L45
Neckel, H. 1995, Sol. Phys., 156, 7
Nesvorný, D. 2009, ApJ, 701, 1116
Nesvorný, D. & Morbidelli, A. 2008, ApJ, 688, 636
ODonovan, F. T., Charbonneau, D., Harrington, J., et al. 2009, in IAU Symposium, Vol. 253, IAU Symposium, 536539
ODonovan, F. T., Charbonneau, D., Mandushev, G., et al. 2006, ApJ, 651, L61
Rabus, M., Deeg, H. J., Alonso, R., Belmonte, J. A., & Almenara, J. M. 2009, ArXiv e-prints
Raetz, S., Mugrauer, M., Schmidt, T. O. B., et al. 2009, Astronomische Nachrichten, 330, 459
Rozelot, J. P., Godier, S., & Lefebvre, S. 2001, Sol. Phys., 198, 223
Simon, J. L., Bretagnon, P., Chapront, J., et al. 1994, A& A, 282, 663
Sozzetti, A., Torres, G., Charbonneau, D., et al. 2007, ApJ, 664, 1190

Chapter 4

I. Sky maps for Hot Jupiters.

R. Heller, D. Mislis & J. Antoniadis,
Astronomy & Astrophysics, 508, 1509H, 2009

Transit detections of extrasolar planets around main-sequence stars. I. Sky maps for Hot Jupiters.

R. Heller[1], D. Mislis[1] & J. Antoniadis[2]

[1]Hamburger Sternwarte, Gojenbergsweg 112, D-21029 Hamburg, Germany
email : mdimitri@hs.uni-hamburg.de
[2]Aristotle University of Thessaloniki, Dept. of Physics, Section of Astrophysics, Astronomy and Mechanics, GR-541 24 Thessaloniki, Greece

Accepted : 03 October 2009

ABSTRACT

The findings of more than 350 extrasolar planets, most of them nontransiting Hot Jupiters, have revealed correlations between the metallicity of the main-sequence (MS) host stars and planetary incidence. This connection can be used to calculate the planet formation probability around other stars, not yet known to have planetary companions. Numerous wide-field surveys have recently been initiated, aiming at the transit detection of extrasolar planets in front of their host stars. Depending on instrumental properties and the planetary distribution probability, the promising transit locations on the celestial plane will differ among these surveys. We want to locate the promising spots for transit surveys on the celestial plane and strive for absolute values of the expected number of transits in general. Our study will also clarify the impact of instrumental properties such as pixel size, field of view (FOV), and magnitude range on the detection probability. We used data of the Tycho catalog for $\approx$ 1 million objects to locate all the stars with $0^{\mathrm{m}} \lesssim m_{\mathrm{V}} \lesssim 11.5^{\mathrm{m}}$ on the celestial plane. We took several empirical relations between the parameters listed in the Tycho catalog, such as distance to Earth, m_{V}, and $(B - V)$, and those parameters needed to account for the probability of a star to host an observable, transiting exoplanet. The empirical relations between stellar metallicity and planet occurrence combined with geometrical considerations were used to yield transit probabilities for the MS stars in the Tycho catalog. Magnitude variations in the FOV were simulated to test whether this fluctuations would be detected by BEST, XO, SuperWASP and HATNet. We present a sky map of the expected number of Hot Jupiter transit events on the basis of the Tycho catalog. Conditioned by the accumulation of stars towards the galactic plane, the zone of the highest number of transits follows the same trace, interrupted by spots of very low and high expectation values. The comparison between the considered transit surveys yields significantly differing maps of the expected transit detections. While BEST provides an unpromising map, those for XO, SuperWASP, and HATNet show FsOV with up to 10 and more expected detections. The sky-integrated magnitude distribution predicts 20 Hot Jupiter transits with orbital periods between 1.5 d and 50 d and $m_{\mathrm{V}} < 8^{\mathrm{m}}$, of which two are currently known. In total, we expect 3412 Hot Jupiter transits to occur in front of MS stars within the given magnitude range. The most promising observing site on Earth is at latitude $= -1$.

Keywords Stars: planetary systems – Occultations – Galaxy: solar neighborhood – Galaxy: abundances – Instrumentation: miscellaneous – Methods: observational

4.1 Introduction

A short essay by Otto Struve (Struve 1952) provided the first published proposal of transit events as a means of exoplanetary detection and exploration. Calculations for transit detection probabilities (Rosenblat 1971; Borucki & Summers 1984; Pepper & Gaudi 2006) and for the expected properties of the discovered planets have been done subsequently by many others (Gillon et. al. 2005; Fressin et al. 2007; Beatty & Gaudi 2008). Until the end of the 1990s, when the sample of known exoplanets had grown to more than two dozen (Castellano et al. 2000), the family of so-called 'Hot Jupiters', with 51 Pegasi as their prototype, was unknown and previous considerations had been based on systems similar to the solar system. Using geometrical considerations, Rosenblatt (1971) [1] found that the main contribution to the transit probability of a solar system planet would come from the inner rocky planets. However, the transits of these relatively tiny objects remain undetectable around other stars as yet.

The first transit of an exoplanet was finally detected around the sun-like star HD209458 (Charbonneau et al. 2000; Queloz et al. 2000). Thanks to the increasing number of exoplanet search programs, such as the ground-based Optical Gravitational Lensing Experiment (OGLE) (Udalski et al. 1992), the Hungarian Automated Telescope (HAT) (Bakos et al. 2002, 2004), the Super Wide Angle Search for Planets (SuperWASP) (Street et al. 2003), the Berlin Exoplanet Search Telescope (BEST) (Rauer et al. 2004), XO (McCullough et al. 2005), the Transatlantic Exoplanet Survey (TrES) (Alonso et al. 2007), and the Tautenburg Exoplanet Search Telescope (TEST) (Eigmüller & Eislöffel 2009) and the space-based missions 'Convection, Rotation & Planetary Transits' (CoRoT) (Baglin et al. 2002) and Kepler (Christensen-Dalsaard et al. 2007), the number of exoplanet transits has grown to 62 until September 1st 2009[2] and will grow drastically within the next years. These transiting planets have very short periods, typically < 10 d, and very small semimajor axes of usually < 0.1 AU, which is a selection effect based on geometry and Kepler's third law (Kepler et al. 1619). Transiting planets with longer periods present more of a challenge, since their occultations are less likely in terms of geometrical considerations and they occur less frequently.

Usually, authors of studies on the expected yield of transit surveys generate a fictive stellar distribution based on stellar population models. Fressin et al. (2007) use a Monte-Carlo procedure to synthesize a fictive stellar field for OGLE based on star counts from Gould et al. (2006), a stellar metallicity distribution from Nordström et al. (2004), and a synthetic structure and evolution model of Robin et al. (2003). The metallicity correlation, however, turned out to underestimate the true stellar metallicity by about 0.1dex, as found by Santos et al. (2004) and Fischer & Valenti (2005). In their latest study, Fressin et al. (2009) first generate a stellar population based on the Besançon catalog from Robin et al. (2003) and statistics for multiple systems from Duquennoy & Mayor (1991) to apply then the metallicity distribution from Santos et al. (2004) and issues of detectability (Pont et al. 2006). Beatty & Gaudi (2008) rely on a Galactic structure model by Bahcall & Soneira (1980), a mass function as suggested by Reid et al. (2002) based on Hipparcos data, and a model for interstellar extinction to estimate the overall output of the current transit surveys TrES, XO, and Kepler. In their paper on the number of expected planetary transits to be detected by the upcoming Pan-STARRS survey (Kaiser 2004), Koppenhoefer et al. (2009) also used a Besançon model as presented in Robin et al. (2003) to derive a brightness distribution of stars in

---

[1] A correction to his Eq. (2) is given in Borucki & Summers (1984).

[2] Extrasolar Planets Encyclopedia (EPE): `www.exoplanet.eu`. Four of these 62 announced transiting planets have no published position.

the target field and performed Monte-Carlo simulations to simulate the occurrence and detections of transits. These studies include detailed observational constraints such as observing schedule, weather conditions, and exposure time and issues of data reduction, e.g. red noise and the impact of the instrument's point spread function.

In our study, we rely on the extensive data reservoir of the Tycho catalog instead of assuming a stellar distribution or a Galactic model. We first estimate the number of expected exoplanet transit events as a projection on the complete celestial plane. We refer to recent results of transit surveys such as statistical, empirical relationships between stellar properties and planetary formation rates. We then use basic characteristics of current low-budget but high-efficiency transit programs (BEST, XO, SuperWASP, and HATNet), regardless of observational constraints mentioned above, and a simple model to test putative transits with the given instruments. With this procedure, we yield sky maps, which display the number of expected exoplanet transit detections for the given surveys, i.e. the transit sky as it is seen through the eyeglasses of the surveys.

The Tycho catalog comprises observations of roughly 1 million stars taken with the Hipparcos satellite between 1989 and 1993 (ESA 1997; Hoeg 1997). During the survey, roughly 100 observations were taken per object. From the derived astrometric and photometric parameters, we use the right ascension (α), declination (δ), the color index ($B - V$), the apparent visible magnitude m_{V}, and the stellar distance d that have been calculated from the measured parallax. The catalog is almost complete for the magnitude limit $m_{\mathrm{V}} \lesssim 11.5^{\mathrm{m}}$, but we also find some fainter stars in the list.

4.2 Data analysis

The basis of our analysis is a segmentation of the celestial plane into a mosaic made up of multiple virtual fields of view (FsOV). In a first approach, we subdivide the celestial plane into a set of $181 \times 361 = 65\,341$ fields. Most of the current surveys do not use telescopes, which typically have small FsOV, but lenses with FsOV of typically $8^\circ \times 8^\circ$. Thus, we apply this extension of $8^\circ \times 8^\circ$ and a stepsize of $\Delta\delta = 1^\circ = \Delta\alpha$, with an overlap of 7° between adjacent fields, for our automatic scanning in order to cover the complete sky. We chose the smallest possible step size in order to yield the highest possible resolution and the finest screening, despite the high redundancy due to the large overlap. A smaller step size than 1° was not convenient due to limitations of computational time. An Aitoff projection is used to fold the celestial sphere onto a 2D sheet.

4.2.1 Derivation of the stellar parameters

One key parameter for all of the further steps is the effective temperature T_{eff} of the stars in our sample. This parameter is not given in the Tycho catalog but we may use the stellar color index ($B - V$) to deduce T_{eff} by

$$T_{\mathrm{eff}} = 10^{[14.551-(B-V)]/3.684}\,\mathrm{K} \ , \tag{4.1}$$

which is valid for main-sequence (MS) stars with $T_{\mathrm{eff}} \lesssim 9\,100\,\mathrm{K}$ as late as type M8 (Reed 1998). Although we apply this equation to each object in the catalog, of which a significant fraction might exceed $T_{\mathrm{eff}} = 9\,100\,\mathrm{K}$, this will not yield a serious challenge since we will dismiss these spurious candidates below. From the object's distance to Earth d and the visible magnitude m_{V}, we derive the absolute visible magnitude M_{V} via

$$M_{\mathrm{V}} = m_{\mathrm{V}} - 5^{\mathrm{m}} \log\left(\frac{d}{10\,\mathrm{pc}}\right) \quad , \tag{4.2}$$

where we neglected effects of stellar extinction. In the next step, we compute the stellar radius $R_\star$ in solar units via

$$\frac{R_\star}{R_\odot} = \left[\left(\frac{5\,770\,\mathrm{K}}{T_{\mathrm{eff}}}\right)^4 10^{(4.83-M_{\mathrm{V}})/2.5}\right]^{1/2} \tag{4.3}$$

and the stellar mass $M_\star$ by

$$M_\star = (4\pi R_\star^2 \sigma_{\mathrm{SB}} T_{\mathrm{eff}}^4)^{1/\beta} \quad , \tag{4.4}$$

where σ_{SB} is the Stefan-Boltzmann constant. The coefficient β in the relation $L \propto M^\beta$ depends on the stellar mass. We use the values and mass regimes that were empirically found by Cester et al. (1983), which are listed in Table 4.1 (see also Smith 1983).

Table 4.1: Empirical values for β in the mass-luminosity relation Eq. (4.4) as given in Cester et al. (1983).

β	STELLAR MASS REGIME
3.05 ± 0.14	$M_\star \lesssim 0.5\,M_\odot$
4.76 ± 0.01	$0.6\,M_\odot \lesssim M_\star \lesssim 1.5\,M_\odot$
3.68 ± 0.05	$1.5\,M_\odot \lesssim M_\star$

We deduce the stellar metallicity $[\mathrm{Fe/H}]_\star$ from the star's effective temperature T_{eff} and its color index $(B-V)$ by

$$[\mathrm{Fe/H}]_\star = \frac{1}{411}\left(\frac{T_{\mathrm{eff}}}{\mathrm{K}} - 8\,423 + 4\,736\,(B-V) - 1\,106\,(B-V)^2\right) \quad , \tag{4.5}$$

as given in Santos et al. (2004). This relation, however, is only valid for stars with $0.51 < (B-V) < 1.33$, $4\,495\,\mathrm{K} < T_{\mathrm{eff}} < 6\,339\,\mathrm{K}$, $-0.7 < [\mathrm{Fe/H}]_\star < 0.43$, and $\log(g) > 4$. We reject those stars from the sample that do not comply with all these boundary conditions. On the one hand we cleanse our sample of non-MS stars, on the other hand the sample is reduced seriously. While our original reservoir, our 'master sample', consists of 1 031 992 stars from the Tycho catalog, all the restrictions mentioned above diminish our sample to 392 000 objects, corresponding to roughly 38 %.

4.3 Transit occurrence and transit detection

4.3.1 Transit occurrence

Now that we derived the fundamental stellar parameters, we may turn towards the statistical aspects of planetary occurrence, geometric transit probability and transit detection. We start with the probability for a certain star of the Tycho catalog, say the i^{th}

star, to host an exoplanet. For F, G, and K dwarfs with $-0.5 < [\mathrm{Fe/H}]_i < 0.5$, Fischer & Valenti (2005) found the empirical relationship

$$\wp_{\exists\,\mathrm{planet},i} = 0.03 \cdot 10^{2 \cdot [\mathrm{Fe/H}]_i} \tag{4.6}$$

for a set of 850 stars with an analysis of Doppler measurements sufficient to detect exoplanets with radial velocity (RV) semiamplitudes $K > 30\,\mathrm{m\,s^{-1}}$ and orbital periods shorter than 4 yr (see Marcy et al. 2005; Wyatt et al. 2007 for a discussion of the origin of this formula and its implications for planet formation). These periods are no boundary conditions for our simulations since we are only interested in surveys with observing periods of $\leq 50\,\mathrm{d}$. The additional constraint on the metallicity does not reduce our diminished sample of 392 000 stars since there is no star with $-0.7 < [\mathrm{Fe/H}]_i < -0.5$ in the Tycho catalog. Similar to the correlation we use, Udry & Santos (2007) found a metallicity distribution of exoplanet host stars equivalent to $\wp_{\exists\,\mathrm{planet},i} = 0.044 \cdot 10^{2.04 \cdot [\mathrm{Fe/H}]_i}$. However, this fit was restricted to stars with $[\mathrm{Fe/H}]_\star > 0$ since they suspect two regimes of planet formation. Sozzeti et al. (2009) extended the uniform sample of Fischer & Valenti (2005) and found the power-law $\wp_{\exists\,\mathrm{planet},i} = 1.3 \cdot 10^{2 \cdot [\mathrm{Fe/H}]_i} + C$, $C \in \{0, 0.5\}$, to yield the best data fit. These recent studies also suggest that there exists a previously unrecognized tail in the planet-metallicity distribution for $[\mathrm{Fe/H}]_\star < 0$. Taking Eq. (4.6) we thus rather underestimate the true occurrence of exoplanets around the stars from the Tycho catalog. The metallicity bias of surveys using the RV method for the detection of exoplanets is supposed to cancel out the bias of transit surveys (Could et al. 2006; Beatty & Guadi 2008).

In the next step, we analyze the probability of the putative exoplanet to actually show a transit. Considering arbitrary inclinations of the orbital plane with respect to the observer's line of sight and including Kepler's third law, Gilliland et al. (2000) found the geometric transit probability to be

$$\wp_{\mathrm{geo},i} = 23.8 \left(\frac{M_i}{M_\odot}\right)^{-1/3} \left(\frac{R_i}{R_\odot}\right) \left(\frac{P}{\mathrm{d}}\right)^{-2/3} \quad , \tag{4.7}$$

where P is the orbital period. A more elaborate expression – including eccentricity, planetary radius, the argument of periastron and the semi-major axis instead of the orbital period – is given by Seagroves et al. (2003). Note that $\wp_{\mathrm{geo},i}$ in Eq. (4.7) does not explicitly but implicitly depend on the semi-major axis a via $P = P(a)$! The probability for an exoplanetary transit to occur around the i^{th} star is then given by

$$\wp_{\mathrm{occ},i} = \wp_{\exists\,\mathrm{planet},i} \cdot \wp_{\mathrm{geo},i} \quad , \tag{4.8}$$

where P is the remaining free parameter, all the other parameters are inferred from the Tycho data. Since we are heading for the expectation value, i.e. the number of expected transits in a certain field of view (FOV), we need a probability density for the distribution of the orbital periods of extrasolar planets. On the basis of the 233 exoplanets listed in the EPE on July 6th 2007, Jiang et al. (2007) used a power-law fit $\delta(P) = C(k) \cdot (P/\mathrm{d})^{-k}$, with $C(k)$ as the normalization function, and the boundary condition for the probability density $\int_0^\infty \mathrm{d}P\, \delta(P) = 1$ to get

$$\delta(P) = \frac{1-k}{B^{1-k} - A^{1-k}} \left(\frac{P}{\mathrm{d}}\right)^{-k} \tag{4.9}$$

with $A = 1.211909\,\mathrm{d}$ and $B = 4517.4\,\mathrm{d}$ as the lower and upper limits for the period distribution and $k = 0.9277$. This function is subject to severe selection effects and bases on data obtained from a variety of surveys and instruments. It overestimates short-period planets since Jiang et al. (2007) included transiting planets and the associated selection effects. While the function presumably does not mirror the true distribution of orbital periods of exoplanets, it is correlated to the period distribution to which current instruments are sensitive, in addition to geometric selection effects as given by Eq. (4.7).

We now segment the celestial plane into a mosaic made up of multiple virtual FsOV, as described at the beginning of Sect. 4.2, to calculate the number of expected transits in that field. In Sect. 4.3.2 we will attribute the FOV of the respective instrument to that mosaic and we will also consider the CCD resolution. The number of stars comprised by a certain FOV is n. The number of expected transits around the i^{th} star in that field, N_i, with periods between P_1 and P_2 is then given by

$$\begin{aligned} N_i &= \int_{P_1}^{P_2} \mathrm{d}P \; \delta(P) \; \wp_{\mathrm{occ},i} \qquad (4.10) \\ &= \wp_{\exists\,\mathrm{planet},i} \cdot 23.8 \left(\frac{M_i}{M_\odot}\right)^{-1/3} \left(\frac{R_i}{R_\odot}\right) \frac{1-k}{B^{1-k} - A^{1-k}} \\ &\quad \times \frac{1}{1/3-k} \left(P_2^{1/3-k} - P_1^{1/3-k}\right) \mathrm{d}^{2/3} \quad \Big|_{A<P_1<P_2<B} \; , \end{aligned}$$

and the number of expected transits in the whole FOV is

$$N = \sum_{i=1}^{n} N_i \; . \qquad (4.11)$$

We emphasize that this is not yet the number of expected transit detections within a certain FOV (see Sect. 5.4) but the number of expected transits to occur within it.

A graphical interpretation of this analysis is presented in Fig. 4.1, where we show a sky map of the expected number of exoplanet transits around MS stars with $m_{\mathrm{V}} \lesssim 11.5^{\mathrm{m}}$ for orbital periods between $P_1 = 1.5\,\mathrm{d}$ and $P_2 = 50\,\mathrm{d}$. This map bases on several empirical relationships and on substantial observational bias towards close-in Jupiter-like planets, but nevertheless it represents the transit distribution to which current instrumentation has access to. The pronounced bright regions at the upper left and the lower right are the anti-center and the center of the Milky Way, respectively. The absolute values of $0.5 \lesssim N \lesssim 5$ for the most of the sky are very well in line with the experiences from wide-field surveys using a 6° × 6° field. Mandushev et al. (2005) stated 5 to 20 or more exoplanet transit candidates, depending on Galactic latitude, and a ratio of $\approx 25 : 1$ between candidates and confirmed planets, which is equivalent to $0.2 \lesssim N \lesssim 1$. Our values are a little higher, probably due to the slightly larger FOV of 8° × 8° used in Fig. 4.1 and due to the effect of blends and unresolved binaries (see discussion in Sect. 5.5).

In the left panel of Fig. 4.2, we show the distribution of expected transits from our simulation as a function of the host stars' magnitudes compared to the distribution of the observed transiting exoplanets. The scales for both distributions differ about an order of magnitude, which is reasonable since only a fraction of actual transits is observed as yet. For $m_{\mathrm{V}} < 8^{\mathrm{m}}$, only HD209458b and HD189733b are currently know to show transits whereas we predict 20 of such transits with periods between 1.5 d and 50 d to occur in total. We also find that the number of detected transiting planets does not follow the shape of the simulated distribution for $m_{\mathrm{V}} > 9^{\mathrm{m}}$. This is certainly

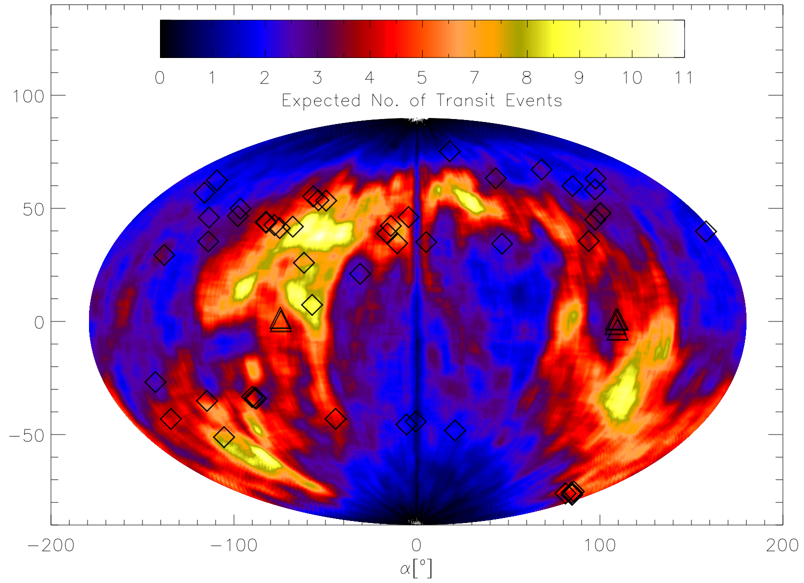

Figure 4.1: Sky map of the expected number of exoplanet transit events, N, with orbital periods between $P_1 = 1.5\,\mathrm{d}$ and $P_2 = 50\,\mathrm{d}$ on the basis of 392 000 objects from the Tycho catalog. The published positions of 58 transiting planets from the EPE as of September 1st 2009 are indicated with symbols: 6 detections from the space-based CoRoT mission are labeled with triangles, 52 ground-based detections marked with squares. The axes only refer to the celestial equator and meridian.

induced by a lack of instruments with sufficient sensitivity towards higher apparent magnitudes, the much larger reservoir of fainter stars that has not yet been subject to continuous monitoring, and the higher demands on transit detection pipelines.

Our transit map allows us to constrain convenient locations for future ground-based surveys. A criterion for such a location is the number of transit events that can be observed from a given spot at latitude l on Earth. To yield an estimate, we integrate N over that part of the celestial plane that is accessable from a telescope situated at l. We restrict this observable fan to $l - 60° < \delta < l + 60°$, implying that stars with elevations $> 30°$ above the horizon are observable. The number of the transit events with $m_{\mathrm{V}} \lesssim 11.5^{\mathrm{m}}$ that is observable at a certain latitude on Earth is shown in the right panel of Fig. 4.2. This distribution resembles a triangle with its maximum almost exactly at the equator. Its smoothness is caused by the wide angle of 120° that flattens all the fine structures that can be seen in Fig. 4.1.

4.3.2 Transit detection

So far, we have computed the sky and magnitude distributions of expected exoplanet transits with orbital periods between 1.5 d and 50 d, based on the stellar parameters from the Tycho data and empirical relations. In order to estimate if a possible transit

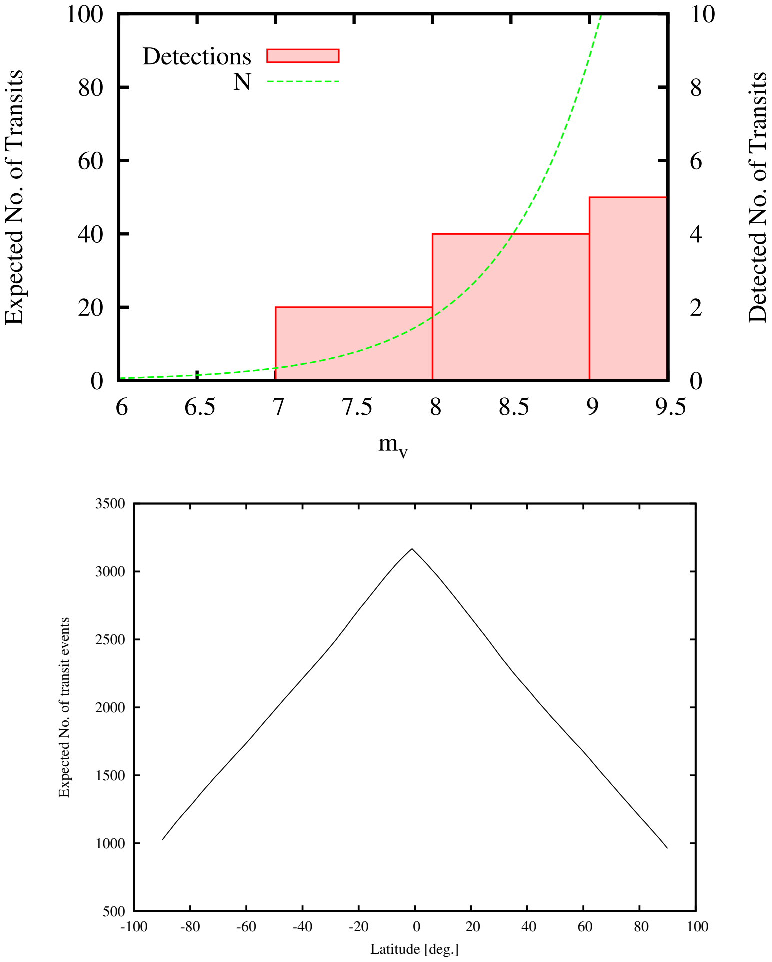

Figure 4.2: Sky-integrated number of transits per magnitude (top panel) and as a function of latitude (bottom panel). *Top*: While the green line represents our simulations, the rosy bars show the number of transiting planets per magnitude bin discovered so far. Note the different scales at the left and right ordinates! *Bottom*: The triangle represents the expected number of transits that can be seen at elevations higher than 30° over the horizon at a given latitude on Earth.

can actually be observed, one also has to consider technical issues of a certain telescope as well as the efficiency and the selection effects of the data reduction pipelines. The treatment of the pipeline will not be subject of our further analysis. The relevant aspects for our concern are the pixel size of the CCD, its FOV, the $m_{\rm V}$ range of the CCD-telescope combination, and the declination fan that is covered by the telescope.

To detect a transit, one must be able to distinguish the periodic transit pattern within a light curve from the noise in the data. Since the depth of the transit curve is proportional to the ratio $A_P/A_\star$, where A_P and $A_\star$ are the sky-projected areas of the planet and the star, respectively, and $R_P/R_\star = \sqrt{A_P/A_\star}$, with R_P as the planetary radius, the detection probability for a certain instrument is also restricted to a certain regime of planetary radii. Assuming that the transit depth is about 1 %, the planetary radius would have to be larger than $\approx R_\star/10$. We do not include an elaborate treatment of signal-to-noise in our considerations (see Aigrain & Pont 2007). Since our focus is on MS stars and our assumptions for planetary occurrence are based on those of Hot Jupiters, our argumentation automatically leads to planetary transits of exoplanets close to $\approx R_\star/10$.

We also do not consider observational aspects, such as integration time and an observer on a rotating Earth with observation windows and a finite amount of observing time (see Fleming et al. 2008 for a review of these and other observational aspects). Instead, we focus on the technical characteristics of four well-established transit surveys and calculate the celestial distribution of expected exoplanet transit detections in principle by using one of these instruments. The impact of limited observing time is degraded to insignificance because the span of orbital periods we consider in Eq. (4.10) reaches only up to $P_2 = 50\,$d. After repeated observations of the same field, such a transiting companion would be detected after $\lesssim 3\,$yr, which is the typical duty cycle of current surveys.

Our computations are compared for four surveys: BEST, XO, SuperWASP, and HATNet. This sample comprises the three most fruitful surveys in terms of first planet detections and BEST – a search program that used a telescope instead of lenses. While observations with BEST have been ceased without any confirmed transit detection, XO has announced detections and SuperWASP and HATNet belong the most fruitful surveys to date. An overview of the relevant observational and technical properties of these surveys is given in Table 4.1. For each survey, we first restrict the Tycho master sample to the respective magnitude range, yielding an $m_{\rm V}$-restricted sample. In the next step, we virtually observe the subsample with the fixed FOV of the survey telescope, successively grazing the whole sky with steps of 1° between adjacent fields. The FOV is composed of a number of CCD pixels and each of these pixels contains a certain number of stars, whose combined photon fluxes merge into a count rate. Efficient transit finding has been proven to be possible from the ground in crowded fields, where target objects are not resolved from neighbor stars. To decide whether a hypothetical transit around the $i^{\rm th}$ star in the pixel would be detected, we simulate the effect of a transiting object that reduces the light flux contribution l_i of the $i^{\rm ht}$ star on the combined flux $\sum_k^n l_k$ of the stars within a pixel. If the $i^{\rm th}$ magnitude variation on the pixel-combined light is $\Delta m_{{\rm V},i} \geq 0.01^{\rm m}$, which is a typical accuracy limit of current ground-based surveys, then we keep this star for further analysis of the transit detection as described in Sects. 4.2 and 4.3.1, otherwise it is rejected. The fluxes, however, are not listed in the Tycho catalog; instead, we can use the visible magnitude $m_{{\rm V},i}$ of a star and calculate its relative flux f_i/f_0 with respect to a reference object with flux f_0 at magnitude $m_{{\rm V},0}$:

$$\frac{f_i}{f_0} = 10^{(m_{\mathrm{V},0} - m_{\mathrm{V},i})/2.5} \quad . \tag{4.12}$$

The magnitude variation can then be computed via

$$\begin{aligned} 0.01 \overset{!}{\leq} \Delta m_{\mathrm{V},i} &= -\,2.5 \cdot \log \left(\frac{0.99 \cdot f_i + \sum\limits_{k \neq i}^{n} f_k}{\sum\limits_{k}^{n} f_k} \right) \\ &= -\,2.5 \cdot \log \left(\frac{0.99 \cdot \frac{f_i}{f_0} + \sum\limits_{k \neq i}^{n} \frac{f_k}{f_0}}{\sum\limits_{k}^{n} \frac{f_k}{f_0}} \right) \quad . \end{aligned} \tag{4.13}$$

Without loss of generality we chose $m_{\mathrm{V},0} = 30^{\mathrm{m}}$ as reference magnitude.

Table 4.2: Instrumental properties of the treated surveys.

Survey	δ range	FOV	CCD Pixel Size	m_{V} Range [Mag.]
BEST	$-16^o < \delta < 90^o$	3.1^o	5.5″/mm	$8 < m_{\mathrm{V}} < 14$
XO	$-39^o < \delta < 90^o$	7.2^o	25.4″/mm	$9 < m_{\mathrm{V}} < 12$
SuperWASP	$-44^o < \delta < 90^o$	7.8^o	13.8″/mm	$7 < m_{\mathrm{V}} < 12$
HATNet	$-28^o < \delta < 90o$	8.3^o	14.0″/mm	$7 < m_{\mathrm{V}} < 12$

	δ & m_{V} Limited Sample	δ, m_{V} & Δm_{V} Limited Sample	δ, m_{V}, Δm_{V} & MS Limited Sample
BEST	546 382 (52.94 %)	516 524 (50.05 %)	222 854 (21.59 %)
XO	620 477 (60.12 %)	597 842 (57.93 %)	263 213 (25.51 %)
SuperWASP	745 227 (72.21 %)	703 707 (68.19 %)	311 404 (30.18 %)
HATNet	721 473 (69.91 %)	686 927 (66.56 %)	283 350 (27.46 %)

In the last three columns we list the reduced Tycho master sample of 1 031 992 stars after we applied the subsequent boundary conditions: the survey's sky-coverage (δ range), its m_{V} limitation, magnitude variation $\Delta m_{\mathrm{V}} > 0.01^{\mathrm{m}}$ for the transit of a Jupiter-sized object around the i^{th} star in a pixel, and the boundary conditions for MS stars, for which the empirical relationships hold (see Sect. 4.2.1). In braces we indicate the portion of the Tycho master sample.

4.4 Results

We develop a procedure for the calculation of the number of expected transit events to *occur* around MS stars based on empirical relations between the stars and planets.

This procedure is then applied to more than 1 million stars from the Tycho catalog to visualize the transit probability for all stars with $m_{\mathrm{V}} \lesssim 11.5^{\mathrm{m}}$ as a sky map. We also compute the celestial distribution of the number of expected transit *detections* for four different, well-established wide-field surveys.

In Fig. 4.3 we present the number of expected transit detections for the technical properties of BEST, XO, SuperWASP, and HATNet. As a general result from these maps, we find that the size of the FOV governs the detection efficiency of a camera. For the method applied here, the CCD resolution, i.e. the pixel size, has almost no impact since we neglect effects of noise, whereas in general the detection limits for transiting planets depend on the CCD resolution in terms of noise (Kovács et al. 2005; Tamuz et al. 2005; Pont et al. 2006). In Table 4.2 you see that the restriction of $\Delta m_{\mathrm{V}} > 0.01^{\mathrm{m}}$ almost doesn't reduce the sample. A large FOV, collecting the light of relatively many stars, outweighs a lower CCD resolution – at least for the range of pixel sizes considered here. Even for the zones around and in the galactic center and anti-center where the stellar density increases drastically, the number of detectable transit events reaches its maximum. This was not foreseeable since blending, simulated by Eq. (4.13), could have reduced the efficiency of transit detection within the crowded zones.

The four survey sky maps portray the very distinct efficiencies of the telescopes. The map of BEST reflects the stellar distribution of the Tycho data best due to the relatively high resolution of the CCD. However, the small FOV leads to very few expected transit detections. BEST's visible magnitude cut at the upper end is 14^{m} while the Tycho catalog is complete only up to 11.5^{m}. Thus, a significant contribution of stars inside this range is excluded in Fig. 4.3**a**. BEST also covers the smallest portion of the sky, compared to the other surveys. The XO project yields a much more promising sky map, owed to the larger FOV of the lenses. But due to the relatively large pixel size and an adverse magnitude cut of $9 < m_{\mathrm{V}}$, XO achieves lower densities of expected detections than SuperWASP and HATNet. As for SuperWASP and HATNet, the difference in the magnitude cuts with respect to the Tycho catalog is negligible for XO but tends to result in an underestimation of the expected detections. That part of the SuperWASP map that is also masked by HATNet looks very similar to the map of the latter one. While HATNet reaches slightly higher values for the expected number of detections at most locations, the covered area of SuperWASP is significantly larger, which enhances its efficiency on the southern hemisphere.

The total of expected transiting planets in the whole sky is 3412 (see Fig. 4.1). By summing up all these candidates within an observational fan of 30° elevation above the horizon, we localize the most convenient site on Earth to mount a telescope for transit observations (see right panel in Fig. 4.2): it is situated at geographical latitude $l = -1^{\circ}$. Given that the rotation of the Earth allows a ground-based observer at the equator, where both hemispheres can be seen, to cover a larger celestial area than at the poles, where only one hemisphere is visible, this result could have been anticipated. Due to the non-symmetric distribution of stars, however, the shape of the sky-integrated number of expected transits as a function of latitude is not obvious. Fig. 4.2 shows that the function is almost symmetric with respect to the equator, with slightly more expected transits at the northern hemisphere. Furthermore, the number of expected transits to be observable at the equator is not twice its value at the poles, which is due to the inhomogeneous stellar distribution. In fact, an observer at the equator triples its number of expected transits with respect to a spot at the poles and can survey almost all of the 3412 transiting objects.

Based on the analysis of the magnitude distribution (left panel in Fig. 4.2), we

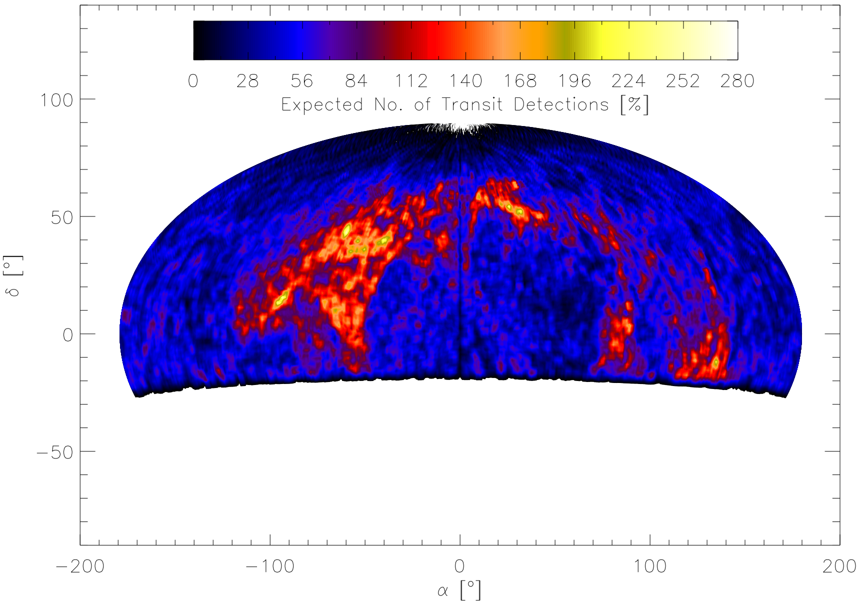
0
28
56
84
112
140
168
196
224
252
280
Expected No. of Transit Detections [%]
100
50
0
−50
δ [°]
−200
−100
0
100
200
α [°]

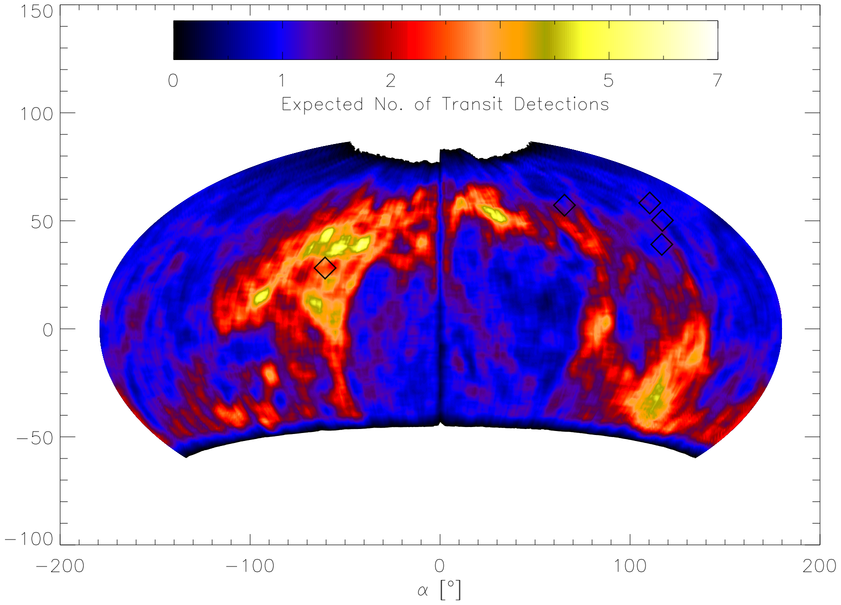
0
1
2
4
5
7
Expected No. of Transit Detections
150
100
50
0
−50
−100
δ [°]
−200
−100
0
100
200
α [°]

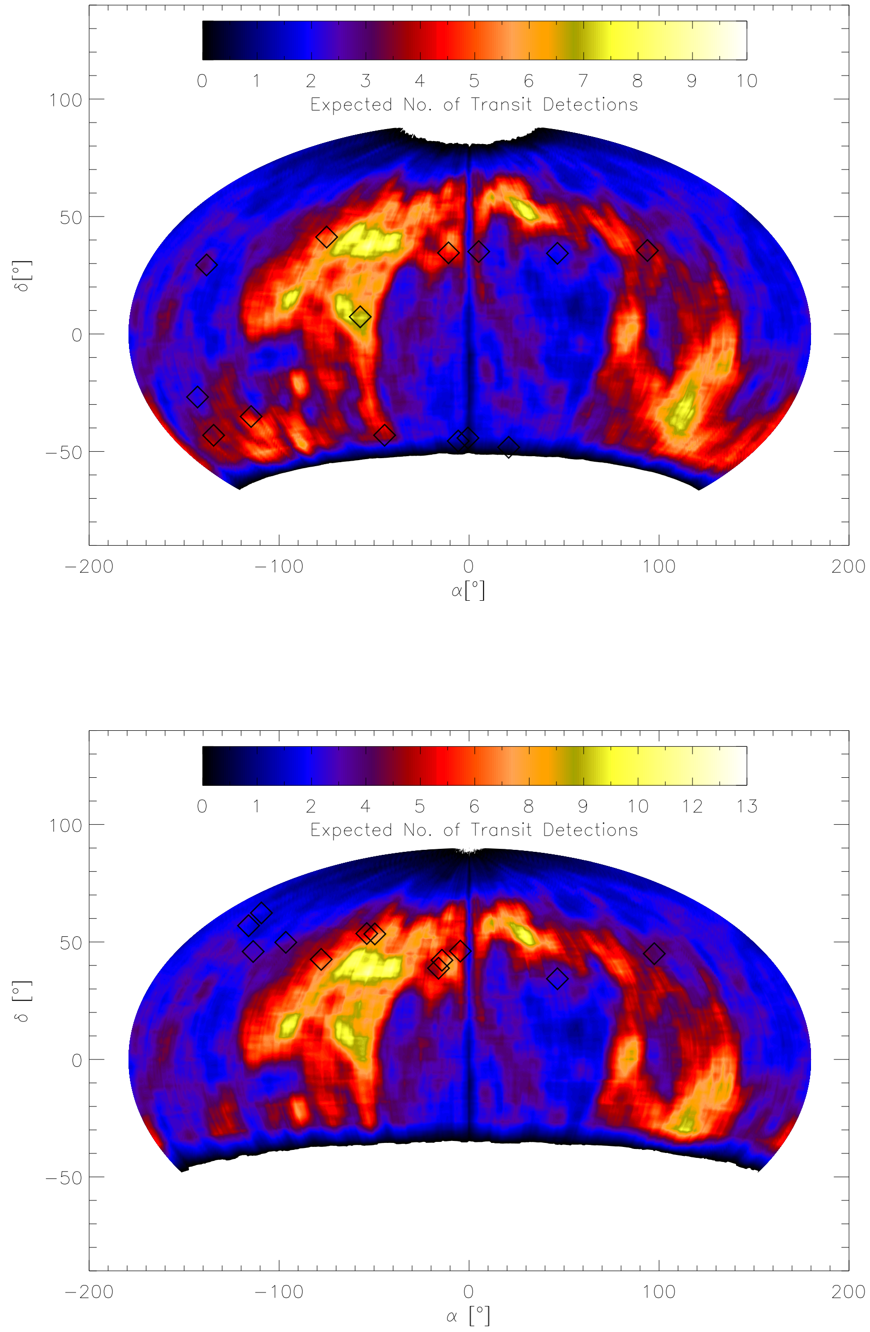

Figure 4.3: Sky maps with expected number of transit detections for BEST (**a**), XO (**b**), SuperWASP (**c**), and HATNet (**d**). Note the different scales of the color code! The published detections of the surveys, taken from the EPE as of September 1st 2009, are indicated with symbols.

predict 20 planets with $m_V < 8$ to show transits with orbital periods between 1.5 d and 50 d, while two are currently known (HD209458b and HD189733b). These objects have proven to be very fruitful for follow-up studies such as transmission spectroscopy (Charbonneau et al. 2002; Vidal-Madjar et al. 2004; Knutson et al. 2007; Sing et al. 2008; Grillmair et al. 2008; Pont et al. 2008) and measurements of the Rossiter-McLaughlin effect (Holt et al. 2006, 2007; Wolf et al. 2007; Narita et al. 2007; Cochran et al. 2008; Winn et al. 2009). Our analysis suggests that a significant number of bright transiting planets is waiting to be discovered. We localize the most promising spots for such detections.

4.5 Discussion

Our values for the XO project are much higher than those provided by Beatty & Gaudi (2008), who also simulated the expected exoplanet transit detections of XO. This is due to their much more elaborate inclusion of observational constraints such as observational cadence, i.e. hours of observing per night, meteorologic conditions, exposure time, and their approach of making assumptions about stellar densities and the Galactic structure instead of using catalog-based data as we did. Given these differences between their approach and ours, the results are not one-to-one comparable. While the study of Beatty & Gaudi (2008) definitely yields more realistic values for the expected number of transit detections considering all possible given conditions, we provide estimates for the celestial distribution of these detections, neglecting observational aspects.

In addition to the crucial respects that make up the efficiency of the projects, as presented in Table 4.2, SuperWASP and HATNet benefit from the combination of two observation sites and several cameras, while XO also takes advantage of twin lenses but a single location. Each survey uses a single camera type and both types have similar properties, as far as our study is concerned. The transit detection maps in Fig. 4.3 refer to a single camera of the respective survey. The alliance of multiple cameras and the diverse observing strategies among the surveys (McCullough et al. 2005; Cameron et al. 2009) bias the speed and efficiency of the mapping procedure. This contributes to the dominance of SuperWASP (18 detections, 14 of which have published positions)[3] over HATNet (13 detections, all of which have published positions)[3], XO (5 detections, all of which have published positions)[3], and BEST (no detection)[3].

It is inevitable that a significant fraction of unresolved binary stars within the Tycho data blurs our results. The impact of unresolved binaries without physical interaction, which merely happen to be aligned along the line of sight, is significant only in the case of extreme crowding. As shown by Gillon & Magain (2007), the fraction of planets not detected because of blends is typically lower than 10 %. The influence of unresolved physical binaries will be higher. Based on the empirical period distribution for binary stars from Duquennoy & Mayor (1991), Beatty & Gaudi (2008) estimate the fraction of transiting planets that would be detected despite the presence of binary systems to be $\approx$ 70 %. Both the contribution of binary stars aligned by chance and physically interacting binaries result in an overestimation of our computations of $\approx$ 40 %, which is of the same order as uncertainties arising from the empirical relationships we use. Moreover, as Willens et al. (2006) have shown, the density of eclipsing stellar binary systems increases dramatically towards the Galactic center. To control the fraction of false alarms, efficient data reduction pipelines, and in particular data analysis algorithms, are necessary (Schwarzenberg-Czerny & Beaulieu 2006).

---

[3] EPE as of September 1st 2009

Recent evidence for the existence of ultra-short period planets around low-mass stars (Sahu et al. 2009), with orbital periods < 1 d, suggests that we underestimated the number of expected transits to occur, as presented in Sect. 4.3.1. The possible underestimation of exoplanets occurring at $[\mathrm{Fe/H}]_\star < 0$ also contributes to a higher number of transits and detections than we computed here. Together with the fact that the Tycho catalog is only complete to $m_\mathrm{V} \lesssim 11.5^\mathrm{m}$, whereas the surveys considered here are sensitive to slightly fainter stars (see Table 4.2), these trends towards higher numbers of expected transit detections might outweigh the opposite effect of unresolved binary stars.

A radical refinement of both our maps for transits occurrence and detections will be available within the next few years, once the 'Panoramic Survey Telescope and Rapid Response System' (Pan-STARRS) (Kaiser et al. 2002) will run to its full extent. Imaging roughly 6000 square degrees every night with a sensitivity down to $m_\mathrm{V} \approx 24$, this survey will not only drastically increase the number of cataloged stars – thus enhance our knowledge of the localization of putative exoplanetary transits – but could potentially detect transits itself (Dupuy & Liu 2009). The Pan-STARRS catalog will provide the ideal sky map, on top of which an analysis presented in this paper can be repeated for any ground-based survey with the aim of localizing the most appropriate transit spots on the celestial plane. The bottleneck for the verification of transiting planets, however, is not the localization of the most promising spots but the selection of follow-up targets accessible with spectroscopic instruments. The advance to fainter and fainter objects thus won't necessarily lead to more transit confirmations. Upcoming spectrographs, such as the ESPRESSO @ VLT and the CODEX @ E-ELT (Pepe & Lovis 2008), can be used to confirm transits around fainter objects. These next-generation spectrographs that will reveal Doppler fluctuations on the order of $\mathrm{cm \cdot s^{-1}}$ will also enhance our knowledge about Hot Neptunes and Super-Earths, which the recently discovered transits of GJ 436 b (Butler et al. 2004), HAT-P-11 b (Bakos et al. 2009), and CoRoT-7b (Leger et al. 2009) and results from Lovis et al. (20099) predict to be numerous.

Further improvement of our strategy will emerge from the findings of more exoplanets around MS stars and from the usage of public data reservoirs like the NASA Star and Exoplanet Database[4], making assumptions about the metallicity distribution of planet host stars and the orbital period distribution of exoplanets more robust.

4.6 Acknowledgements

R. Heller and D. Mislis are supported by a PhD scholarship of the DFG Graduiertenkolleg 1351 "Extrasolar Planets and their Host Stars". We thank J. Schmitt, G. Wiedemann and M. Esposito for their advice on the structure and readability of the paper. The referee deserves our honest gratitude for his comments on the manuscript which substantially improved the scientific quality of this study. This work has made use of Jean Schneiders exoplanet database `www.exoplanet.eu` and of NASA's Astrophysics Data System Bibliographic Services.

---

[4] `http://nsted.ipac.caltech.edu`

4.7 References

Aigrain, S., & Pont, F. 2007, MNRAS, 378, 741
Alonso, R., Brown, T. M., Charbonneau, D., et al. 2007, in Transiting Extrapolar Planets Workshop, ed. C. Afonso, D. Weldrake, & T. Henning, ASP Conf. Ser., 366, 13
Baglin, A., Auvergne, M., Barge, P., et al. 2002, in Stellar Structure and Habitable Planet Finding, ed. B. Battrick, F. Favata, I. W. Roxburgh, & D. Galadi, ESA SP, 485, 17
Bahcall, J. N., & Soneira, R. M. 1980, ApJS, 44, 73
Bakos, G. Á., Lázár, J., Papp, I., Sári, P., & Green, E. M. 2002, PASP, 114, 974
Bakos, G., Noyes, R. W., Kovács, G., et al. 2004, PASP, 116, 266
Bakos, G. ., Torres, G., Pál, A., et al. 2009, ApJ
Beatty, T. G., & Gaudi, B. S. 2008, ApJ, 686, 1302
Borucki, W. J., & Summers, A. L. 1984, Icarus, 58, 121
Butler, R. P., Vogt, S. S., Marcy, G. W., et al. 2004, ApJ, 617, 580
Cameron, A. C., Pollacco, D., Hellier, C., et al. the WASP Consortium, & the SOPHIE & CORALIE Planet-Search Teams 2009, in IAU Symp., 253, 29
Castellano, T., Jenkins, J., Trilling, D. E., Doyle, L., & Koch, D. 2000, ApJ, 532, L51
Cester, B., Ferluga, S., & Boehm, C. 1983, Ap& SS, 96, 125
Charbonneau, D., Brown, T. M., Latham, D. W., et al. 2000, ApJ, 529, L45
Charbonneau, D., Brown, T. M., Noyes, R. W., et al. 2002, ApJ, 568, 377
Christensen-Dalsgaard, J., Arentoft, T., Brown, T. M., et al. 2007, Commun. Asteroseismol., 150, 350
Cochran, W. D., Redfield, S., Endl, M., et al. 2008, ApJ, 683, L59
Dupuy, T. J., & Liu, M. C. 2009, ApJ, 704, 1519
Duquennoy, A., & Mayor, M. 1991, AetA, 248, 485
Eigmüller, P., & Eislöffel, J. 2009, in IAU Symp., 253, 340 ESA 1997, VizieR Online Data Catalog, 1239, 0
Fischer, D. A., & Valenti, J. 2005, ApJ, 622, 1102
Fleming, S. W., Kane, S. R., McCullough, P. R., et al. 2008, MNRAS, 386, 1503
Fressin, F., Guillot, T., Morello, V., et al. 2007, AetA, 475, 729
Fressin, F., Guillot, T., & Nesta, L. 2009, AetA, 504, 605
Gilliland, R. L., Brown, T. M., Guhathakurta, P., et al. 2000, ApJ, 545, L47
Gillon, M., & Magain, P. 2007, in Transiting Extrapolar Planets Workshop, ed. C. Afonso, D. Weldrake, & T. Henning, ASP Conf. Ser., 366, 283
Gillon, M., Courbin, F., Magain, P., et al. 2005, AetA, 442, 731
Gould, A., Dorsher, S., Gaudi, B. S., et al. 2006, Acta Astron., 56, 1
Grillmair, C. J., Burrows, A., Charbonneau, D., et al. 2008, Nature, 456, 767
Hoeg, E. 1997, in ESA SP, 402, Hipparcos - Venice '97, 25
Holt, J. R. 1893, AetA, 12, 646
Jiang, I.-G., Yeh, L.-C., Chang, Y.-C., et al. 2007, AJ, 134, 2061
Kaiser, N., Aussel, H., Burke, B. E., et al. 2002, in SPIE Conf. Ser. 4836, ed. J. A. Tyson, & S. Wolff, 154
Kaiser, N. 2004, in SPIE Conf. Ser. 5489, ed. J. M. Oschmann, Jr., 11
Kepler, J., Ptolemaeus, C., & Fludd, R. 1619
Knutson, H. A., Charbonneau, D., Allen, L. E., et al. 2007, Nature, 447, 183
Koppenhoefer, J., Afonso, C., Saglia, R. P., et al. 2009, AetA, 494, 707
Kovács, G., Bakos, G., & Noyes, R. W. 2005, MNRAS, 356, 557
Leger, A., Rouan, D., Schneider, J., et al. 2009, AetA, 506, 287

Lovis, C., Mayor, M., Bouchy, F., et al. 2009, in IAU Symp., 253, 502
Mandushev, G., Torres, G., Latham, D. W., et al. 2005, ApJ, 621, 1061
Marcy, G., Butler, R. P., Fischer, D., et al. 2005, Progr. Theor. Phys. Suppl., 158, 24
McCullough, P. R., Stys, J. E., Valenti, J. A., et al. 2005, PASP, 117, 783
McLaughlin, D. B. 1924, ApJ, 60, 22
Narita, N., Enya, K., Sato, B., et al. 2007, PASJ, 59, 763
Nordström, B., Mayor, M., Andersen, J., et al. 2004, AetA, 418, 989
Pepe, F. A., & Lovis, C. 2008, Phys. Scrip. Vol. T, 130, 014007
Pepper, J., & Gaudi, B. S. 2006, Acta Astron., 56, 183
Pont, F., Zucker, S., & Queloz, D. 2006, MNRAS, 373, 231
Pont, F., Knutson, H., Gilliland, R. L., Moutou, C., & Charbonneau, D. 2008, MNRAS, 385, 109
Queloz, D., Eggenberger, A., Mayor, M., et al. 2000, AetA, 359, L13
Rauer, H., Eislöffel, J., Erikson, A., et al. 2004, PASP, 116, 38
Reed, B. C. 1998, JRASC, 92, 36
Reid, I. N., Gizis, J. E., & Hawley, S. L. 2002, AJ, 124, 2721
Robin, A. C., Reylé, C., Derrière, S., et al. 2003, AetA, 409, 523
Rosenblatt, F. 1971, Icarus, 14, 71
Rossiter, R. A. 1924, ApJ, 60, 15
Sahu, K. C., Casertano, S., Valenti, J., et al. 2009, in IAU Symp., 253, 45
Santos, N. C., Israelian, G., & Mayor, M. 2004, AetA, 415, 1153
Schwarzenberg-Czerny, A., & Beaulieu, J.-P. 2006, MNRAS, 365, 165
Seagroves, S., Harker, J., Laughlin, G., et al. 2003, PASP, 115, 1355
Sing, D. K., Vidal-Madjar, A., Désert, J.-M., Lecavelier des Etangs, A., & Ballester, G. 2008, ApJ, 686, 658
Smith, R. C. 1983, The Observatory, 103, 29
Sozzetti, A., Torres, G., Latham, D. W., et al. 2009, ApJ, 697, 544
Street, R. A., Pollaco, D. L., Fitzsimmons, A., et al. 2003, in Scientific Frontiers in Research on Extrasolar Planets, ed. D. Deming, & S. Seager, ASP Conf. Ser., 294, 405
Struve, O. 1952, The Observatory, 72, 199
Tamuz, O., Mazeh, T., & Zucker, S. 2005, MNRAS, 356, 1466
Udalski, A., Szymanski, M., Kaluzny, J., Kubiak, M., & Mateo, M. 1992, Acta Astron., 42, 253
Udry, S., & Santos, N. C. 2007, ARAetA, 45, 397
Vidal-Madjar, A., Dsert, J.-M., Lecavelier des Etangs, A., et al. 2004, ApJ, 604, L69
Willems, B., Kolb, U., & Justham, S. 2006, MNRAS, 367, 1103
Winn, J. N., Johnson, J. A., Marcy, G. W., et al. 2006, ApJ, 653, L69
Winn, J. N., Johnson, J. A., Peek, K. M. G., et al. 2007, ApJ, 665, L167
Winn, J. N., Johnson, J. A., Fabrycky, D., et al. 2009, ApJ, 700, 302
Wolf, A. S., Laughlin, G., Henry, G. W., et al. 2007, ApJ, 667, 549
Wyatt, M. C., Clarke, C. J., & Greaves, J. S. 2007, MNRAS, 380, 1737

Chapter 5

II. Extrasolar planets in the habitable zones of their host stars.

D. Mislis, R. Heller, J.H.M.M. Schmitt, E. W. Guenther & J. Antoniadis

Astronomy & Astrophysics, submitted : 19 February 2010

Transit detections of extrasolar planets around main-sequence stars.
II. Extrasolar planets in the habitable zones of their host stars.

D. Mislis[1], R. Heller[1], J.H.M.M. Schmitt[1], E. W. Guenther[2] & J. Antoniadis[3]

[1]Hamburger Sternwarte, Gojenbergsweg 112, D-21029 Hamburg, Germany
email : mdimitri@hs.uni-hamburg.de
[2]Thüringer Landessternwarte Tautenburg, Sternwarte 5, D-07778 Tautenburg, Germany
[3]Max Planck Instutute fuer Radioastronomie, Auf dem Huegel 69, 53121 Bonn, Germany

Submitted : 19 February 2010

ABSTRACT

Recent discoveries of transiting Super-Earths and transiting extrasolar planets at the edge or even far outside the traditional habitable zone (THZ) prove the existence and accessability of such objects. Since their formation process is not yet understood and their occurrence has only recently become subject to science the question about their detection probability remains obscure. Using simple but reasonable assumptions about planetary occurrence, we want to assess the prospects of current transit surveys – ground-based as well as space-based. We also aspire to classify the basic observational properties of the planets and stars that will most likely be found to be transiting systems. We first evaluate the chances of success for ground based transit surveys. Therefore, we employ the data of roughly 1 million stars from the Tycho catalog to derive the location and the fundamental physical parameters of almost all the stars on the celestial plane with $m_{\rm V} < 11.5$. We then use geometrical considerations and an assumption of the planetary occurrence in a star's THZ to derive a sky map of the probability distribution for the occurrence of transits from exoplanet in the THZ of their host stars. Finally, we use data from the CoRoT field IR01 to simulate the detection probabilities of planets in the THZs of their host stars for CoRoT depending on stellar and planetary features, such as the radii of both constituents and the visible stellar magnitude. The sky map for ground-based observations of exoplanet transits in the THZ of their host stars shows dismal prospects of success. Within a field of view of a typical ongoing survey, the detection probability does not exceed 1.4 %. A common value for the celestial plane is 0.2 % per field of view. Current space-based missions, on the other hand, will presumably discover transiting planets in their THZs. Assuming each star in IR01 hosts one planet of at least eight times the size of the Earth in its THZ, it is very likely that at least one of them will be detected by CoRoT.

Keywords Stars: planetary systems – Occultations – Astrobiology – Methods: statistical – Techniques: photometric – Methods: observational

5.1 Introduction

Transiting extrasolar planets are promising targets for the field of astrobiology since they offer direct measurements of the atmospheric composition of potentially inhabited worlds (Webb & Wormleaton 2001; Ehrenreich et al. 2006; Selsis et al. 2007a; Kaltenegger & Traub 2009). The recent detections of the transiting Super-Earths CoRoT-7b (Léger et al. 2009, space-based discovery) and GJ1214b ((Charbonneau et al. 2009, ground-based detection) have shown that today's technology is mature for the exploration of terrestrial planets and their habitability. While most of the transiting planets have been discovered with ground-based instruments, the two space-based missions CoRoT (Deleuil et al. 1997) and Kepler (Borucki et al. 1997) have so far discovered a handful of transiting planets (see Barge et al. (2008); Alonso et al. (2008); Deleuil et al. (2008); Aigrain et al. (2008); Rauer et al. (2009); Léger et al. (2009); Dvorak et al. (2009) for CoRoT and Borucki et al. (2010b); Koch et al. (2010); Dunham et al. (2010); Latham et al. (2010); Jenkins et al. (2010); Borucki et al. (2010a) for Kepler). All of these planets, except for the two mentioned above, are Jupiter-like in terms of mass and radius, and none of them is located in the habitable zone (HZ) of its host star. Thus, none of the currently known transiting planets can be regarded as habitable.

In this paper, we examine the statistical prospects of ground-based as well as space-based surveys for the detection of planets in the HZs of their host stars. In terms of ground-based instrumentation, we rely on a method described in Heller et al. (2009, paper I in the following), where we used the data of roughly one million objects listed in the Tycho catalog, taken with the Hipparcos satellite between 1989 and 1993 (ESA 1997; Hoeg 1997). For the analysis of the space-based perspectives, we simulate exoplanet transits in front of the 14 007 stars located in the CoRoT field IR01, and also examine the impact of the planetary radius on the detection probability in the field; this part will also include terrestrial planets.

5.2 Derivation of stellar properties

5.2.1 Habitable zones around the stars

The method for the derivation of the stellar properties such as T_{eff}, $R_\star$, and $M_\star$ from the parameters given in the Tycho catalog are described in paper I. In this recent study, we use a relationship stated by Fischer & Valenti (2005) between $(B-V)$, as provided by the Tycho catalog, and the stellar metallicity $[\mathrm{Fe/H}]_\star$ to firstly derive $[\mathrm{Fe/H}]_\star$ and finally the probability for planetary occurrence around the stars in the Tycho sample. However, this approach is inappropriate for the calculation of planetary existence in HZs since the empirical relationships are strongly biased towards Hot Jupiters, i.e., planets in orbits with semi-major axes of mostly < 0.1 AU. Up to now, no exoplanet has been discovered that is unambiguously located in the HZ of its host star[1], conection between stellar properties and occurrence of planetary companions in the HZs is not yet assessable. For the following calculations, we thus assume a scenario in which each star has one extrasolar planet in its HZ. Although this approach is rather optimistic, reasonable arguments in favor for this assumption are given in Grether & Lineweaver (2006) and our existence shows that this setting is not totally irrational. If this approximation is too optimistic, our results for the transit probabilities will serve as upper limits.

---

[1] There is ongoing discussion about whether Gl581d is located inside or outside its HZ, owed to different concepts of a HZ, uncertainties in the planetary parameters and the planet's non-circular orbit: The apoastron is situated outside the HZ whereas the periastron is located inside (Selsis et al. 2007b; von Bloh et al. 2007; Beust et al. 2008; Barnes et al. 2009; Mayor et al. 2009, and this paper).

For the calculations of the transit probability $\wp_{\rm geo}$ of a given exoplanet within the HZ, we do not include any assumptions about the habitability times of the putative systems. Since the distances of the stars in our sample are typically of order 300 pc, we also do not take into account effects of the Galactic habitable zone (Gonzalez 2005; Prantzos 2008). We rely on the Eq. (1) from Seagroves et al. (2003) and assume that the planetary radius R_P is small compared to the stellar radius $R_\star$, thus $R_\star - R_P \approx R_\star$. Then the formula transforms into an upper limit for the geometric transit probability:

$$\wp_{\rm geo} \lesssim 0.0045 \, \frac{1\,{\rm AU}}{a} \frac{R_\star}{R_\odot} \frac{1 + e\cos(\pi/2 - \varpi)}{1 - e^2} \quad , \tag{5.1}$$

which includes eccentricity e, the argument of periastron ϖ and the semi-major axis a. Since we are looking for planets within the stellar HZ, a will be given by the range of relevant orbits at orbital distances $d_{\rm THZ}^{\rm in} < a < d_{\rm THZ}^{\rm out}$, with $d_{\rm THZ}^{\rm in}$ and $d_{\rm THZ}^{\rm out}$ as the critical inner and outer radius of the traditional habitable zone (THZ). A simple and established expression for its extent, only as a function of the stellar luminosity $L_\star$, is given by Kasting et al. (1993):

$$d_{\rm THZ} = 1\,{\rm AU} \left(\frac{L_\star / L_\odot}{S_{\rm eff}} \right)^{0.5} \quad , \tag{5.2}$$

where $S_{\rm eff}$ is the effective solar flux, necessary to maintain a certain surface temperature on a planet, in dimensionless units. The latter parameter depends on the planetary albedo and the atmospheric composition of the planet.

Refinements of this THZ include formation and orbital stability of extrasolar planets, geologic activity, abundant water and the planet's atmospheric composition and structure (for a review see Gaidos et al. 2005). A more elaborate definition of a HZ is given by Selsis et al. (2007b), which includes different, putative atmospheric compositions on the planet, i.e. cloud coverage and albedo. Furthermore, the presence of other planets may render planets in the THZ inhabitable due to gravitational perturbations, which slingshot the potentially habitable planet (Dvorak et al. 2003; Schwarz et al. 2005; Sándor et al. 2007). Tidal processes, raised by the host star, can lead to tidal heating on the planet, which can be strong enough as to drive plate tectonics and global volcanism (Jackson et al. 2008; Barnes et al. 2009), or they may generate subsurface oceans analogous to Europa's (Greenberg 2005), thus customizing the HZ to the individual orbital and physical parameters of the planet. Tides may also drive a significant evolution of a planet's orbit and lead to tidal locking (Barnes et al. (2008)). We confine ourselves to using the less complex description by Kasting et al.(1993) since the planetary parameters are unknown.

To obtain an extent of the THZ, we take the values for $S_{\rm eff}$ as provided by Kasting et al. (1993) for a Venus-like planet to maintain liquid water at the inner edge of the THZ ($S_{\rm eff}^{\rm in} = 1.9114$) and a Martian planet at the outer edge, modified to exhibit a maximum greenhouse effect ($S_{\rm eff}^{\rm out} = 0.36$). These two values for $S_{\rm eff}$ define an inner and an outer boundary $d_{\rm THZ}^{\rm in}$ and $d_{\rm THZ}^{\rm out}$ of the THZ around a star as a function of $L_{\star,S_{\rm eff}}$. To translate it into a function of $(B-V)_{S_{\rm eff}}$, we use the relationship given in Parenago (1958) to derive $M_{\rm V}$ from the given color index. Using Eq. (3) from paper I, we then deduce the stellar radius and finally, by means of Eq. (4) in that paper, the stellar mass based on several empirical relations. Using Kepler's 3rd law and assuming $M_{\rm p} \ll M_\star$, the radial boundaries for the THZ can then be converted into limits in terms of orbital period, independent of the planetary radius or mass. In Fig. 5.1 we show the borders of the THZ, i.e. the period limits as a function of the stellar color index $(B-V)$. While the

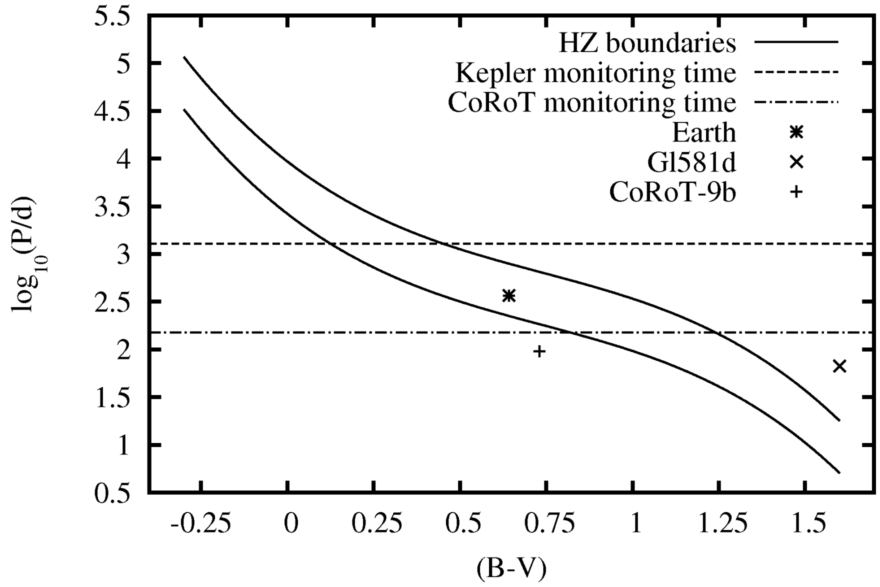

Figure 5.1: Extent of the THZ as given by Eq. (5.2) with $S^{\text{in}}_{\text{eff}} = 1.9114$ for the inner limit and $S^{\text{out}}_{\text{eff}} = 0.36$ for the outer bound. Transiting planets with P less than the Kepler or CoRoT monitoring time will show at least one transit, higher periods leading to smaller detection probabilities. The positions of the Earth, Gl581d, and CoRoT-9b are indicated.

Earth, with $(B-V)_\odot = 0.642$ (Holmberg et al. 2006), is situated well inside the THZ, Gl581d is slightly too far away from its host star. The only known transiting rocky planet so far, CoRoT-7b (Léger et al. 2009), is far too close to its star.

5.2.2 Constraints of eccentricity on the habitability

Now that we can infer the extent of the THZ on the basis of the parameters as provided by the Tycho data, we still have the two free parameters e and ϖ for the computation of $\wp_{\text{geo}}$, which are not known for a certain, putative system. We denote the transit probability for circular orbits with $\wp^{\text{circ}}_{\text{geo}}$. To eliminate the dependence on the stellar radius and the semi-major axis in Eq. (5.1), we present a plot of $\wp_{\text{geo}}(e,\varpi)/\wp^{\text{circ}}_{\text{geo}}$ in Fig. 5.2, which shows that any given eccentricity $\neq 0$ increases the detection probability for the most part of the orbit. With rising eccentricity, the fraction of the orbit that yields detection probabilities higher than for the circular case increases gently. For an arbitrary but fixed eccentricity, say $\tilde{e}$, the geometric transit probability $\wp^{\tilde{e}}_{\text{geo}}(\varpi)$ reaches its minimum at $\varpi_{\text{min}} = \pi$, while the maximum is at $\varpi_{\text{max}} = 0 \vee 2\pi$.

Of course, for the planetary orbit to be fully situated within the THZ, the eccentricity cannot take arbitrary values. For $e = 0$, it is clear that this circle can be well located within the THZ, however, for the other extreme of $e = 1$, this line will cross the inner and the outer edges of the THZ. Obviously, there does exist a highest value e_{max} for the eccentricity at which the whole orbit of the planet still is embedded in the THZ. Using the relation of a being centered within the inner and the outer edge of the THZ, $a = (d^{\text{in}}_{\text{THZ}} + d^{\text{out}}_{\text{THZ}})/2$, and constraining that the closest orbital approximation $d^{\text{close}} = a(1-e)$ between the host star and the planet remains larger than the extent of

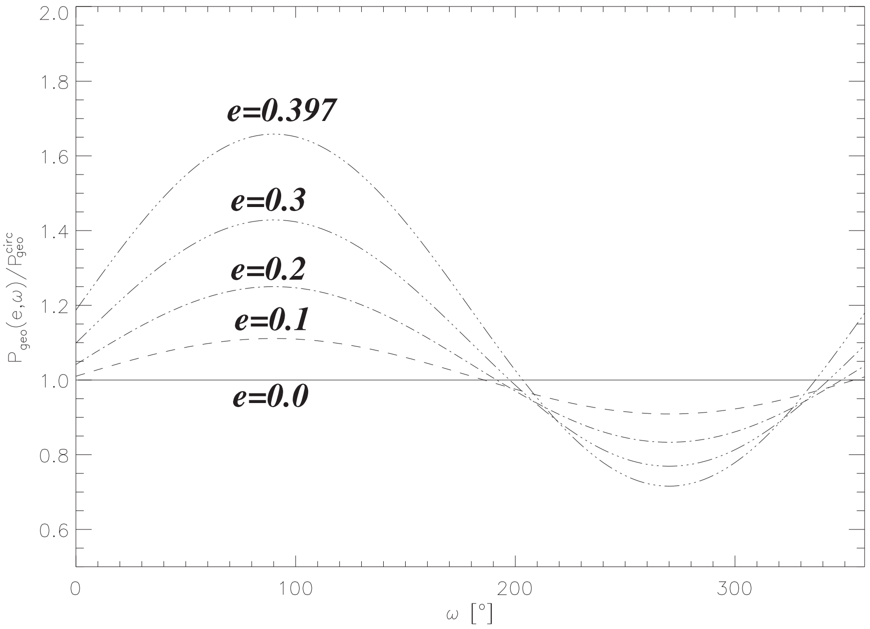

Figure 5.2: Geometric transit probability from Eq. (5.1) as function of ϖ for five different values of *e*. The highest eccentricity of 0.397 is the theoretical maximum value for an orbit to be fully located in the THZ.

the inner edge of the THZ, $d^{\rm close} \geq d^{\rm in}_{\rm THZ}$, we derive

$$e \leq \frac{d^{\rm out}_{\rm THZ} - d^{\rm in}_{\rm THZ}}{d^{\rm out}_{\rm THZ} + d^{\rm in}_{\rm THZ}} \quad , \tag{5.3}$$

and, applying Eq. (5.2), we find

$$e \leq \frac{\sqrt{1/S^{\rm out}_{\rm eff}} - \sqrt{1/S^{\rm in}_{\rm eff}}}{\sqrt{1/S^{\rm out}_{\rm eff}} + \sqrt{1/S^{\rm in}_{\rm eff}}} \quad . \tag{5.4}$$

For the values $S^{\rm in}_{\rm eff} = 1.9114$ and $S^{\rm out}_{\rm eff} = 0.36$ this yields $e_{\rm max} = 0.397$. Thus, the maximum eccentricity for a planet to remain within the THZ of its host star, as defined by Kasting et al. (1993), is independent of any stellar properties.

5.3 Application to survey data

To compute the the probability for the detection of a plant in the THZ, we break this likeliness into three contributions: instrumental probability, observing time probability, and the geometrical probability from Sec. 5.2.1.

5.3.1 Instrumental probability

The instrumental probability specifies the likeliness of an instrumental setup to obtain a high enough signal-to-noise ratio (S/N) to allow for a transit detection. To estimate this probability, we virtually build a common instrument for transit detection, which is composed of a CCD and a lense similar to a ground-based wide field of view (FOV), like those of SuperWASP and HATNet. The CCD equation for the peak value in analog-to-digital units (ADUs), $A_{\rm peak}$, is given by

$$A_{\rm peak} = (876.4\, t_{\rm exp} + 2587.75)\, 10^{(11.41 - m_v)/2.5}\, D^2, \tag{5.5}$$

where m_v is the magnitude of the star, D is the aperture of the lense (or telescope) in units of meters, and $t_{\rm exp}$ is the exposure time. After we derive the peak of the star, we compute and integrate the Gaussian distribution to calculate the total flux from the star with a typical seeing of $S = 0.8''$ and a dynamical photometric radius. We then derive the S/N using the equation from Howell (2008)

$$S/N = \frac{N_*}{\sqrt{N_* + n_{\rm pix}(N_S + N_D + N_R^2)}}, \tag{5.6}$$

with N_* as the total number of counts, $n_{\rm pix}$ as the number of pixels of the photometric aperture and N_S as the sky backgound, N_D as the dark current, and N_R as the readout noise, per pixel respectively. The instrumental probability then is derived as the probability that the given star shows a S/N larger than the transit depth of the planet. The instrumet, the site and observing time specifications of our procedure are given in Table 5.1.

Table 5.1: Specifications of the virtual instrument and the hypothetical observational run

INSTRUMENT (CCD)	
Gain	1.33 ADU/e$^-$
Readout Noise	16.37 e^-
Pixel size	13 μm
CCD measure	3K×3K
Mean Dark	136.7 ADUs/pixel
INSTRUMENT (LENSE)	
Focal length	180 mm
Aperture	60 mm
OBSERVING CONDITIONS	
Seeing	0.80″
m_v of the sky	20.0$^{\mathrm{m}}$
Exposure time	120-3600 s
Total running time	150 d

5.3.2 Observing time probability

Habitable planets have much larger periods that the Hot Jupiters (Fig. 5.1). That leads us to the observing time probability, which we define as the likeliness to detect three transit events in our temporal observing window. We assume an observation window of 150 d aiming at the best case scenario for planets in the THZ. The observing time probability is connected to the S/N ratio, which increases with the square root of the number of measurements.

5.3.3 Geometric probability

We now apply our method to the Tycho data and produce a sky map of the transit probability of exoplanets in the THZs of their host stars. We combine the geometric considerations expressed in Eq. (5.1) with the assumption of one exoplanet in the THZ of the respective host star[2]. With the premise of one planet in the center of the THZ around each star, the probability for a planet to exits around a certain star, $\wp_{\exists\,\mathrm{planet}}$, takes the value 1. Hence, the overall probability for a transit to occur, $\wp_{\mathrm{occ}}$, coincides with the geometric probability:

$$\wp_{\mathrm{occ}} = \wp_{\exists\,\mathrm{planet}} \cdot \wp_{\mathrm{geo}} = \wp_{\mathrm{geo}} \quad . \tag{5.7}$$

5.3.4 Tycho catalog

In the next step, as described in paper I, we scan the sky with a fixed FOV from our instrument, with an overlap of 5° between adjacent fields for a smooth distribution, and calculate the transit probability for each of these FsOV. Due to the magnitude cut of the

---

[2] In paper I we described how these probabilities of transit occurrence are related to the actual transit detection probabilities for certain instruments.

Tycho catalog at $m_\mathrm{V} \lesssim 11.5^\mathrm{m}$ and the chosen technique, the results will be adaptive to current ground-based wide-field surveys, e.g. SuperWASP and HATNet.

There is a tendency in the Tycho data towards more giant stars and early-type main sequence (MS) stars, caused by the magnitude cut at $m_\mathrm{V} \lesssim 11.5^\mathrm{m}$. Planetary transits in front of these stars will not be detectable with ground-based instruments due to the limited accuracy achievable from the ground. In addition to our optimistic assumption of one planet in the THZ of each star, this bias leads to an upper limit for the transit probabilities.

To plot $\wp_\mathrm{occ}$ for each FOV as a function of the right ascension α and declination δ, e and ϖ must be fixed for each putative planet. We assume circular orbits, thus $e = 0$, for a planet located in the inner part of the THZ of its host star in order to – as mentioned above – derive the most optimistic scenario. We run four our program with four different exposure times, namely 120 s, 680 s, 1240 s and 1800 s.

5.3.5 CoRoT field

As an example for the prospects of space-based transit surveys, we refer to CoRoT, one of the two current space-based missions aiming at the detection of extrasolar planet transits. We base our analysis on real data[3], i.e., the light curves (LCs) of 14 007 stars observed with CoRoT in the 'initial run' field IR01, which is located at $\alpha = 06^\mathrm{h}57^\mathrm{m}18^\mathrm{s}, \delta = -01°42'00''$ (J2000.0) (Kabath et al. 2007). The stellar color index $(B-V)$ and the star's visible magnitude m_V are known properties. We first derive the stellar effective temperature T_eff from $(B-V)$ (see paper I) and then calculate $R_\star$ from a fit to the data given in Habets & Heintze (1981),

$$\frac{R_\star}{R_\odot} = -7.52082 + 2.2959 \cdot \log_{10}(T_\mathrm{eff}) \ , \tag{5.8}$$

assuming that the stars in the CoRoT sample are all on the MS. We used a sample of 1000 non-variable LCs, to calculate the standard deviation σ. Given that m_V is known, we then apply a fit to the correlation between m_V and σ and deduce the lower limit for the apparent brightness, or in mathematical terms: an upper limit for the visible magnitude $m_\mathrm{V}^\mathrm{min}$, that is necessary for CoRoT to discern the transit. This correlation is given by

$$m_\mathrm{V}^\mathrm{min} = 11.761 + 0.170 \cdot \left(\frac{R_\mathrm{p}}{R_\star}\right)^2 \quad . \tag{5.9}$$

We now use $\sigma(m_\mathrm{V}) = 1.00921{-}7.8{\cdot}10^{-4} m_\mathrm{V}$ to simulate CoRoT LCs. Therefore, we model the transit of an extrasolar planet for the two cases of a circular orbit at the inner edge of the THZ as well as at its outer border. To test whether the transit depth D is larger than the standard deviation, we grasp a range of planetary radii $0 < R_\mathrm{p} < 10\,R_\mathrm{E}$ and stellar radii $0.1\,R_\odot < R_\star < 1.5\,R_\odot$, corresponding to spectral types between F0 and M6 (Habets & Heintze 1981). R_E and $R_\odot$ are the radius of the Earth and the Sun, respectively. If a LC for a certain R_p-$R_\star$ combination shows $D > \sigma$, then we assume the transit can be detected. In that case we calculate the individual probability for transit occurrence of that star with Eq. (5.7).

As an example, we exhibit a very promising configuration of a relatively bright ($m_\mathrm{V} = 13$) K5 star, transited by a planet in a circular orbit at the inner edge of the THZ and an unfavorable system where an apparently dim ($m_\mathrm{V} = 15$) F5 star shows

---

[3] http://idoc-corot.ias.u-psud.fr

occultations of a planet located at the outer border of the THZ (Fig. 5.4). For each of these two configurations, we show the three cases of a $2\,R_\mathrm{E}$, a $3\,R_\mathrm{E}$, and a $4\,R_\mathrm{E}$ planet. The upper row in Fig. 5.4 shows the favorable star-planet configuration. In all the three LCs the transit is clearly distinguished from the noise. For the transits of the unfavorable system, however, the transit can only be detected in the case of a planet with $4\,R_\mathrm{E}$ radius.

Finally, we take into account the geometric concerns of the transit probability as given by Eq. (5.7). Although $\wp_\mathrm{occ}$ is only a function of $R_\star$ and a, since we assume $e = 0$, and not a function of R_p, the result of our procedure will depend on the planetary radius. This is due to the perceptibility of the transit, which strongly depends on R_p. Only if the respective transit of a certain R_p-$R_\star$ duet yields $D > \sigma$, this pair will be selected for the computation of $\wp_\mathrm{occ}$ via Eq. (5.7), otherwise $\wp_\mathrm{occ} = 0$ by default. Another dependence of $\wp_\mathrm{occ}$ on $R_\star$ arises from Eq. (5.2). We study the case of a planet transiting at the inner limit of the THZ, thus $a = d_\mathrm{THZ}^\mathrm{in}$, and the case of a transit at the outer periphery where $a = d_\mathrm{THZ}^\mathrm{out}$. And as expressed in Eq. (5.2), these boundaries depend on $L_\star$ and thus on $R_\star$.

5.4 Results

5.4.1 Prospects for ground-based surveys

The sky map for the occurrence probability of extrasolar planet transits in the THZ of their MS host star is shown in Fig. 5.3. Circular orbits in the center of the THZ are assumed. To apply a certain eccentricity and orientation of periastron for all stars, this map has to be multiplied with the corresponding factor provided by Fig. 5.2. Of course, the distributions of eccentricity values and orbital orientations will not be uniform in the sky but they will follow some statistical functions. Most of the eccentricities will be close to 0 due to the proximity of transiting planets to their host stars and consequential orbital decay due to tidal interactions on time scales much shorter than the typical life time of a MS star. However, an non-zero average eccentricity might emerge in the future for planets in the THZ of their host stars. Then our map must be multiplied with the respective factor provided by Fig. 5.2.

The Galactic plane is clearly visible in the sky map. Obviously, its path yields the highest transit probabilities, which is simply due to the increased stellar density in the FOV. The absolute values for $\wp_\mathrm{occ}$ are typically around 1 % in the Galactic zone, but only about 2 permil for the most part of the sky. These values are upper limits, based on the likely overestimate that each star hosts a planet in its THZ and on a bias in the Tycho data towards giants and early-type stars.

5.4.2 Prospects for space-based surveys

In Fig. 5.5 we highlight the radii of the prospective transiting exoplanets and their host stars to be discovered by CoRoT. For the left panel we assumed that each star in IR01 entails a transiting planet at the inner border of its THZ, $d_\mathrm{THZ}^\mathrm{in}$, whereas the planet is assumed to be at the outer edge $d_\mathrm{THZ}^\mathrm{out}$ in the right panel. Both plots show the color-coded contours of the R_p-$R_\star$-projected probability that at least one transit would be observed in IR01 if each of the stars in the field hosted a planet with the respective radius, $\wp_\mathrm{IR01}$. The differences in the absolute values between the left and the right panel are as high as 0.5 in some regions but the general shapes of the probability distributions for these

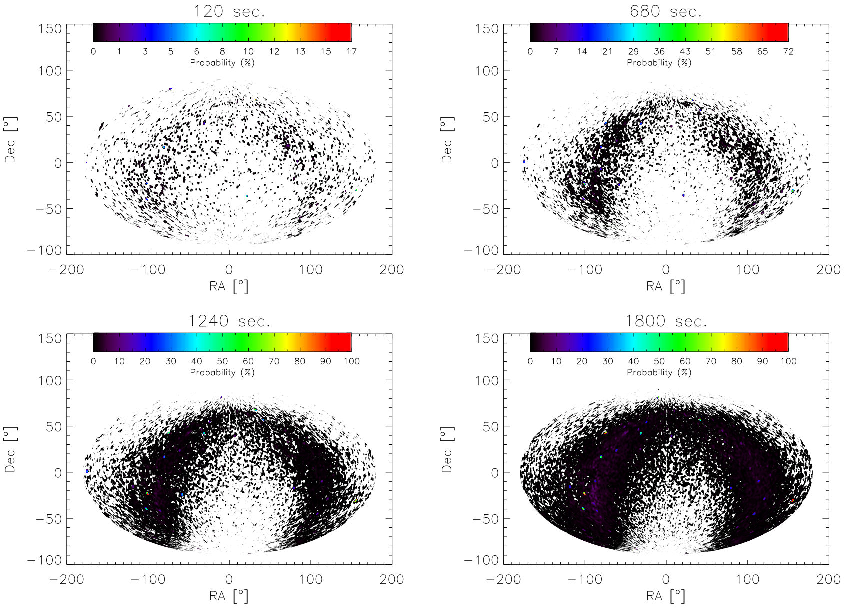

Figure 5.3: Sky maps of the transit probability $\wp_{\rm occ}$ for extrasolar planets in the center of the THZs of their host stars, using varius exposure times (120, 680, 1240 and 1800 seconds respectively). It is obvious from maps that the probability do discover habitabe transiting planet using ground based surveys is very small. To include e and ϖ, these color maps have to be multiplied by the respective values from Fig. 5.2. The white parts of the maps mean saturation or S/N lower than 10^{-3}.

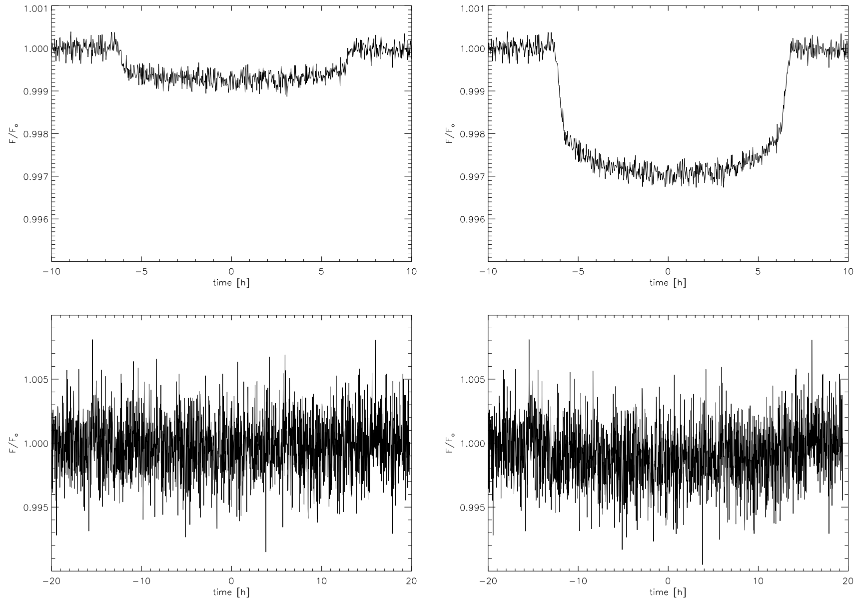

Figure 5.4: Simulated CoRoT LCs of stars with transiting planets of 2, and $4\,R_\oplus$ (from left to right). F/F_0 is the relative flux with F as the number of photons and F_0 as the mean photon flux outside the transit. *Upper row:* These transits occur around a K5 star at $m_{\rm V} = 13$, while the transiting planet is at the inner edge of the THZ. *Lower row:* Here, we consider an F5 star at $m_{\rm V} = 15$ and for the planetary orbit we assume the outer edge of the THZ. Only for $R_{\rm p} = 4\,R_\oplus$ the transit becomes distinguishable from the noise between ≈ -1.5 and ≈ 1.5 d around the center.

putative planets in the CoRoT field IR01 are similar. The comparison of both panels visualizes the fact that, due to the geometrical aspects, the detection probabilities for transiting planets at the inner edge of the THZ are higher than for bodies at the outer edge.

Planets with radii larger than 10 times the radius of the Earth could easily be detected in the THZs of all the stars that we took into account, i.e. $\wp_{\mathrm{IR01}} = 100\,\%$ for $0 \leq R_\star \leq 1.5\,R_\odot$. The interesting limits for the transit detectability appear for Super Earths with $R_\mathrm{p} < 10\,R_\mathrm{E}$. Down to $R_\mathrm{p} \approx 8\,R_\mathrm{E}$ we find $\wp_{\mathrm{IR01}} = 100\,\%$, whereas an Earth-like planet with $R_\mathrm{p} = 1\,R_\mathrm{E}$ could only be detected around very small MS stars. Nevertheless, the search for an Earth twin in the THZs of IR01 stars will succeed if these planets are common.

The magnitude cuts for CoRoT are indicated with lines. An R_p-$R_\star$ combination below a certain magnitude line could not be detected as a transiting system, provided that the host star shows the respective apparent magnitude.

5.5 Discussion

For ground-based surveys, the values for the occurrence probability of exoplanets in the THZ of their hosts stars are small compared to the transit probabilities of hot Jupiters (see paper I). While exoplanet transits in the THZs of their host stars would be observed with probabilities $\lesssim 1\,\%$, passages of hot Jupiters turned out to appear typically on the order of 15 % outside the Galactic plane and $\approx 80\,\%$ inside within a comparable FOV. To increase the chances of success for the detection of an exoplanet in the THZ, one would have to observe a large amount of stars and moreover, the respective field would have to be monitored for a relatively long time due to the relatively long periods of the planets of $\gtrsim 100\,\mathrm{d}$ (see Fig. 5.1). The method we present here to compute the probabilities for transit *occurrence* of extrasolar planets around MS stars in the THZs does not invoke all observational constraints. Although we construct a virtual telescope similar to those currently in use for wide-field surveys, we do not consider the observing schedule and weather conditions. We also neglect issues of data reduction, e.g. red noise, the impact of the instrument's point spread function, and efficiency and selection effects of the data reduction pipelines. A consideration of these parameters would allow for the calculation of the actual *detection* probabilities of such transits and these values will be much smaller than those presented here. Moreover, we sticked to use rather optimisitic assumptions throughout the issue of ground-based observations. More realsitic conditions would render our probabilities to even smaller values. This context makes ground-based surveys an inappropriate tool for the detection of transit events in the THZ.

Fortunately, there are two ongoing space-based missions that come into consideration for the detection of such planets: CoRoT and Kepler. Planets in the THZs to be discovered by the former mission will most likely be located in the inner part of the zones and will show radii larger than $\approx 8\,R_\mathrm{E}$. Smaller planets down to the size of the Earth might also be detected and would orbit stars of the size of the Sun and smaller. The probability distribution in Fig. 5.5 shows that, if exoplanets with $R_\mathrm{p} \gtrsim R_\mathrm{E}$ in the THZ are common, then they are very likely to be detected with CoRoT. As long as their non-detections are not due to flaws in the data reduction and if they do not have systematic origin, their absence around stars with THZs that are covered by CoRoT in terms of orbital and observational period (see Fig. 5.1) constrains the occurrence of Earth-like planets.

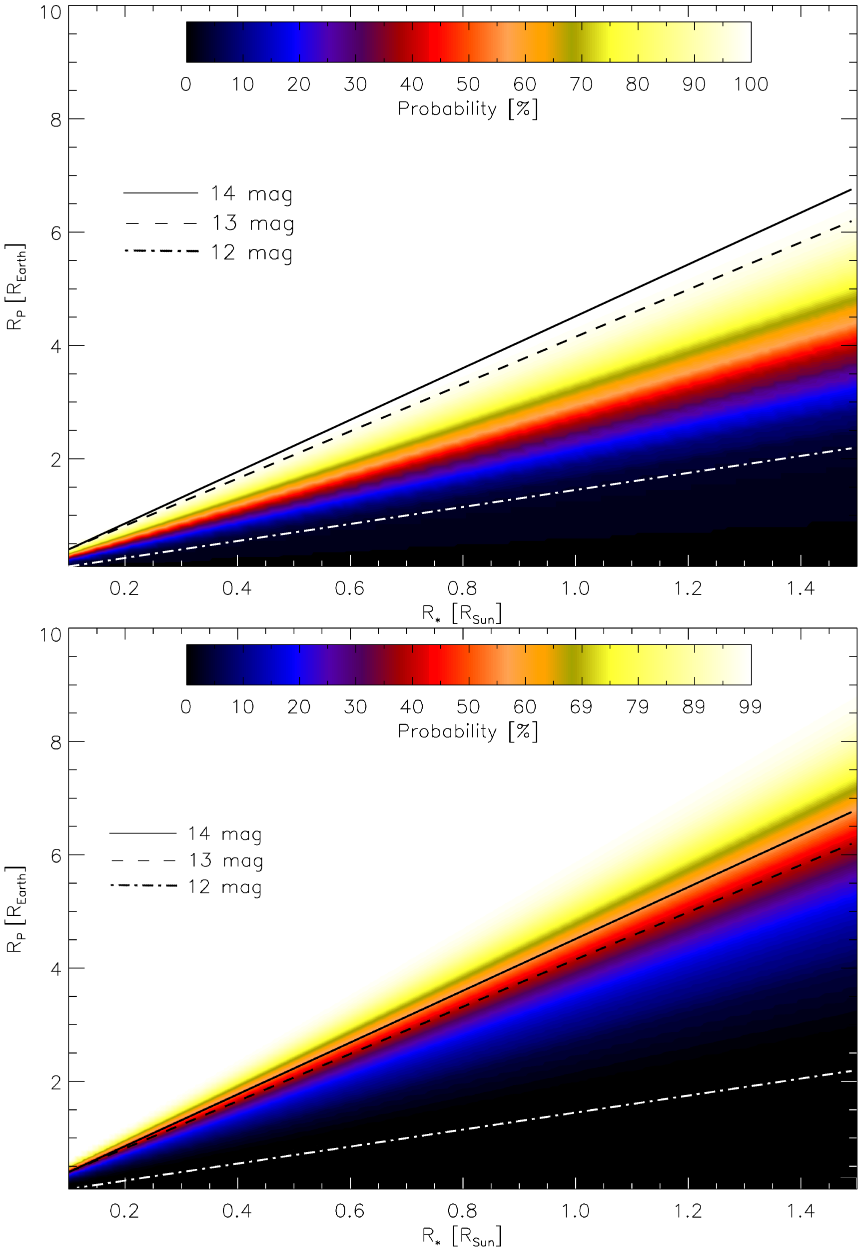

Figure 5.5: Transit detection probability of CoRoT for field IR01 ($\wp_{\rm IR01}$) as a function of stellar and planetary radius. Limits for the visible magnitudes are overplotted. *Top*: The transiting planets are assumed to have a circular orbit at the inner edge $d_{\rm THZ}^{\rm in}$ of the THZ. This corresponds to the highest geometrical detection probabilities. *Bottom*: The transiting planets are assumed to have a circular orbit at the outer edge $d_{\rm THZ}^{\rm out}$ of the THZ, yielding lower probabilities.

5.6 Acknowledgements

D. Mislis and R. Heller are supported by a PhD scholarship of the DFG Graduiertenkolleg 1351 “Extrasolar Planets and their Host Stars”.

5.7 References

Aigrain, S., Collier Cameron, A., Ollivier, M., et al. 2008, A&A, 488, L43
Alonso, R., Auvergne, M., Baglin, A., et al. 2008, A&A, 482, L21
Barge, P., Baglin, A., Auvergne, M., et al. 2008, A&A, 482, L17
Barnes, R., Jackson, B., Greenberg, R., & Raymond, S. N. 2009, ApJ, 700, L30
Barnes, R., Raymond, S. N., Jackson, B., & Greenberg, R. 2008, Astrobiology, 8, 557
Beust, H., Bonfils, X., Delfosse, X., & Udry, S. 2008, A&A, 479, 277
Borucki, W. J., Koch, D., Basri, G., et al. 2010a, in AASMA, Vol. 215, AASMA, 101.01
Borucki, W. J., Koch, D. G., Brown, T. M., et al. 2010b, ArXiv e-prints
Borucki, W. J., Koch, D. G., Dunham, E. W., & Jenkins, J. M. 1997, in ASPC, Vol. 119
Charbonneau, D., Berta, Z. K., Irwin, J., et al. 2009, Nature, 462, 891
Deleuil, M., Barge, P., Leger, A., & Schneider, J. 1997, in ASPC, Vol. 119
Deleuil, M., Deeg, H. J., Alonso, R., et al. 2008, A&A, 491, 889
Dunham, E. W., Borucki, W. J., Koch, D. G., et al. 2010, ArXiv e-prints
Dvorak, R., Pilat-Lohinger, E., Funk, B., & Freistetter, F. 2003, A&A, 410, L13
Dvorak, R., Schneider, J., Lammer, H., Barge, P., & Wuchterl, G. 2009, ArXiv e-prints
Ehrenreich, D., Tinetti, G., Lecavelier Des Etangs, A., Vidal-Madjar, A., & Selsis, F. 2006, A&A, 448, 379
ESA. 1997, VizieR Online Data Catalog, 1239, 0
Fischer, D. A. & Valenti, J. 2005, ApJ, 622, 1102
Gaidos, E., Deschenes, B., Dundon, L., et al. 2005, Astrobiology, 5, 100
Gonzalez, G. 2005, Origins of Life and Evolution of the Biosphere, 35, 555
Greenberg, R. 2005, Europa - the Ocean Moon : search for an alien biosphere
Grether, D. & Lineweaver, C. H. 2006, ApJ, 640, 1051
Habets, G. M. H. J. & Heintze, J. R. W. 1981, A&AS, 46, 193
Heller, R., Mislis, D., & Antoniadis, J. 2009, A&A, 508, 1509
Hoeg, E. 1997, in ESA Special Publication, Vol. 402, Hipparcos - Venice 97, 2530
Holmberg, J., Flynn, C., & Portinari, L. 2006, MNRAS, 367, 449
Howell, S. B. 1989, PASP, 101, 616 Jackson, B., Barnes, R., & Greenberg, R. 2008, MNRAS, 391, 237
Jenkins, J. M., Borucki, W. J., Koch, D. G., et al. 2010, ArXiv e-prints
Kabath, P., Eigmüller, P., Erikson, A., et al. 2007, AJ, 134, 1560
Kaltenegger, L. & Traub, W. A. 2009, ApJ, 698, 519
Kasting, J. F., Whitmire, D. P., & Reynolds, R. T. 1993, Icarus, 101, 108
Koch, D. G., Borucki, W. J., Rowe, J. F., et al. 2010, ArXiv e-prints
Latham, D. W., Borucki, W. J., Koch, D. G., et al. 2010, ArXiv e-prints
Léger, A., Rouan, D., Schneider, J., et al. 2009, A&A, 506, 287
Mayor, M., Bonfils, X., Forveille, T., et al. 2009, A&A, 507, 487
Parenago, P. P. 1958, Soviet Astronomy, 2, 151
Prantzos, N. 2008, Space Science Reviews, 135, 313
Rauer, H., Queloz, D., Csizmadia, S., et al. 2009, A&A, 506, 281

Sándor, Z., Süli, Á., Érdi, B., Pilat-Lohinger, E., & Dvorak, R. 2007, MNRAS, 375, 1495
Schwarz, R., Pilat-Lohinger, E., Dvorak, R., Erdi, B., & Sándor, Z. 2005, Astrobiology, 5, 579
Seagroves, S., Harker, J., Laughlin, G., Lacy, J., & Castellano, T. 2003, PASP, 115, 1355
Selsis, F., Chazelas, B., Bordé, P., et al. 2007a, Icarus, 191, 453
Selsis, F., Kasting, J. F., Levrard, B., et al. 2007b, A&A, 476, 1373
von Bloh, W., Bounama, C., Cuntz, M., & Franck, S. 2007, A&A, 476, 1365

Chapter 6

An Algorithm for correcting CoRoT raw light curves

D. Mislis, J.H.M.M. Schmitt, L. Carone, E. W. Guenther, & M. Pätzold

Astronomy & Astrophysics, accepted : 5 April 2010

An Algorithm for correcting CoRoT raw light curves

D. Mislis[1], J.H.M.M. Schmitt[1], L. Carone[2], E. W. Guenther[3], & M. Pätzold[2]

[1]Hamburger Sternwarte, Gojenbergsweg 112, D-21029 Hamburg, Germany
email : mdimitri@hs.uni-hamburg.de
[2] Rheinisches Institut für Umweltforschung, Abteilung Planetenforschung, an der Universität Köln, Aachener Str. 209, 50931 Köln, Germany
[3]Thüringer Landessternwarte Tautenburg, Sternwarte 5, D-07778 Tautenburg, Germany

Accepted : 5 April 2010

ABSTRACT

We introduce the CoRoT Detrend Algorithm (*CDA*) for detrending CoRoT stellar light curves. *CDA* has the capability to remove random jumps and systematic trends encountered in typical CoRoT data in a fully automatic fashion. Since huge jumps in flux can destroy the information content of a light curve, such an algorithm is essential. From a study of 1030 light curves in the CoRoT IRa01 field we developed three simple assumptions CDA is based upon. In this paper we describe analytically the algorithm and we provide some examples of how it works. We demonstrate its functionality of the algorithm in the cases of CoRoT0102702789, CoRoT0102874481, CoRoT0102741994 and CoRoT0102729260. Using CDA in the specific case of CoRoT0102729260 we detect a candidate exoplanet around the host star of spectral type G5, which remains undetected in the raw light curve; the estimated planetary parameters are $R_p = 6.27R_E$ and $P = 1.6986$ days.

Keywords methods: data analysis, surveys, planetary systems, stars: variables

6.1 Introduction

The CoRoT satellite was successfully launched in 2006. On board CoRoT there is a small 27cm telescope feeding two science channels to study astroseismology and transits respectively (Baglin et al. 2000). The CoRoT has a field of view (FOV) of $\sim 2.7^o$ *x* 3.05^o. In its first field (IRa01 - $\alpha = 6^h46^m53^s$ & $\delta = -00^o12^{'}00$”), CoRoT had observed continuously for 60 days, producing uninterrupted light curves for the first time. The data from the IRa01 have been public since December 2008 and the astronomical community has access to these data. Unfortunately, the CoRoT light curves are affected by a variety of instrumental problems, which severely hamper the data interpretation. In order to overcome these difficulties we have developed the CoRot Detrend Algorithm (*CDA*). In this paper the algorithm is presented and demonstrate its function on some typical CoRoT data sets.

6.2 CoRoT data: The problems

The CoRoT data files contain multi-color light curves, produced by inserting a low-resolution dispersing prism into the telescope beam. With this set-up it is intended

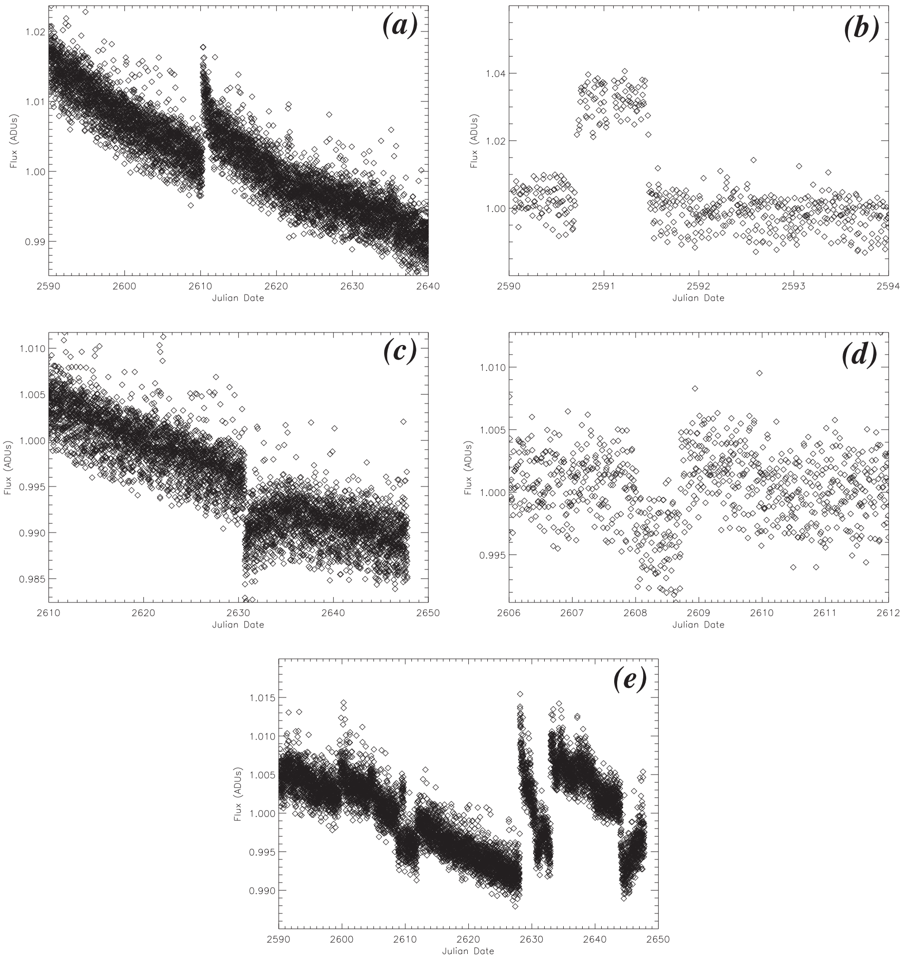

Figure 6.1: Jumps and trends in CoRoT light curves. CoRoT01027-21492 **(a)** -24482 **(b)** -40879 **(c)** -49307 **(d)** - 27431 **(e)**.

to provide simultaneous light curves in the red (R), green (G) and blue (B) bands, however, these bands do not correspond to true photometric filters and, in fact, the bands may differ from star to star. We study the multi-color data in this paper, but also consider the total (white) flux obtained by summing up the individual light curves through $W = R + G + B$.

Fig. 6.1 are typical CoRoT light curves from IRa01. The first panel of Fig. 6.1 shows a typical exponential jump very similar to a flare star. A trend is also evident. In the second light curve there appears a box-shape jump, in the third and fourth light curves one finds features similar as in the first and second light curves, except that the jumps are downwards. We note that the downward jump in the third light curve is very similar to a transit event, thus making the detection of true transits difficult. Combinations of all the above features appear, in fact a rather typical CoRoT light curve. Essentially, two basic instrumental problems appear in all CoRoT light curves: First, there is a long-term trend, forcing a secular decrease of the light curve intensity over the full observing period of 60 days. The strengths of the trends in different sources may be different; the physical cause of these trends is not well understood. The second and even more serious problem is the instrumental jumps in the light curves. The term “jump” refers to a sudden variation of intensity without any obvious reason. Many of these jumps do in fact look like stellar flares, however, the vast majority of these features is clearly instrumental. The physical explanation for these jumps could be, cosmic radiation and the time evolution of bright pixels (Pinheiro da Silva et al. 2008). These jumps are a random phenomenon and affect each filter differently. An inspection of hundreds of CoRoT light curves similar to those presented in Fig. 6.1 allows to classify the observed shapes of jumps into five groups:

- Sudden intensity increase and exponentially decrease (Fig. 6.1 - panel a)
- Sudden intensity increase and decreases (box shape, Fig. 6.1 - panel b)
- Sudden intensity decrease and exponentially increase afterwards (Fig. 6.1 - panel c)
- Sudden intensity decrease and increase (negative box shape, Fig. 6.1 - panel d)
- All of the combinations above (Fig. 6.1 - panel e)

A statistical analysis of IRa01 field (visual inspection) shows that only a small minority (Table 6.1) of all jumps is so powerful that they simultaneously appear in each colour. Most of the light curves are affected not only by one single jump, but by many jumps occurring in the different filters at different times. In Table 6.1 we show the results of a statistical study of the appearance and the shapes of jumps using data form IRa01. The three first columns of Table 6.1 show the number of light curves which suffer from jumps in the respective filter filter and the fourth column shows the total amount.

6.3 The CDA Algorithm

6.3.1 General features

It is quite difficult to describe all the features perturbing CoRoT light curve with a given function, since there are many different shapes of jumps with many different functional

Table 6.1: Statistical results for the jumping light curves. Our sample has 1030 CoRoT light curves from IRa01 field. Jumps appear in more than 50% of all light curves in all filters; in 0.82% of all light curves jumps in all filters occur at the same time.

$R\ filter$	$G\ filter$	$B\ filter$	$Total$
38.14%	14.4%	15.1%	67.6%

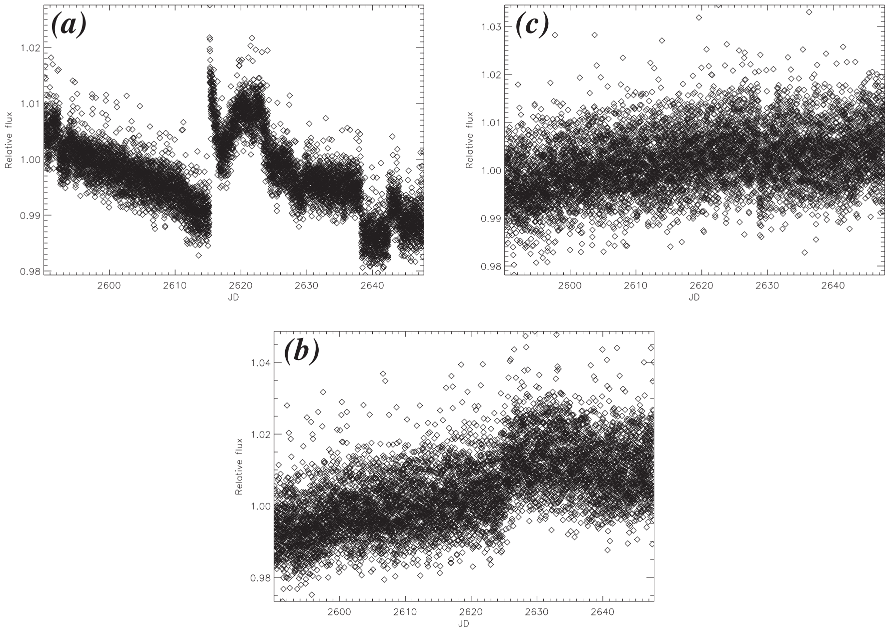

Figure 6.2: CoRoT0102729260. Three filter light curves (R **(a)**, B **(b)** ,G **(c)**) from a data set. The jumps in red light curve does not appear in the other filters and vice versa.

forms. Furthermore, the problem is complex, because we do not know which of light curve features are real signals (real transits, real flares etc.) or instrumental effects. The algorithm is based on three assumptions: (a) trends appear in almost all light curves and both flux increases and decreases can occur. The trends are not periodic and we assume them to be a long-term phenomenon (Aigrain et al. 2009). (b) The second assumption also accrues from the statistical analysis of the data. The study of 1030 light curves from IRa01 field shows that only 0.82 % of them are affected by a jump in all three filters at the same time. In these cases the jump is very large and affects all bands with the same temporal pattern, however, in most cases the jumps affect only one band at any given time (Fig. 6.2), and we therefore ignore those cases where jumps occur simultaneously in all three bands. (c) Real transits must appear in all three filters, while, of course, the intensity and transit depth can vary from filter to filter. In summary, for the *CDA* we assume that

- Long term trends appear in all CoRoT light curves
- Jumps are random phenomena appearing in different filters at different times.

- The real signals from transits appear in all three bands

We emphasize that *CDA* works only for events (like transits), which appear in two or more bands; *CDA* does not work for stellar flares, since most stellar flares do not show any flux enhancements in the red and green band, but in the blue band. Under these circumstances *CDA* will destroy real signals, unless the flare is so powerful to appear in all bands.

6.3.2 The algorithm

CDA uses all the colour light curve simultaneously of each star to remove the instrumental features. The basic idea of *CDA* is to use the cleanest filter band as a proxy for the whole light curve. The raw data files of each CoRoT light curve have a quality flag (CoRoT files - column 4), indicating the quality of each data point (Mazeh et al. 2009). We first remove all these ”bad points” (points with high noise flagged by CoRoT); note that these ”bad points” are same for all the filters per star. In this paper we will use light curves with all ”bad points” already removed (as in Fig. 6.1). As noted above in our first assumption, trends are a long-term phenomenon. A 3^{rd} degree polynomial is fit to the entire light curve in order to remove the trend in each filter per star. Because each CoRoT light curve typically has thousands of data points, the polynomial does not fit short-term variations and real short-term events like transits. We thus write

$$Flux = a + b \cdot JD + c \cdot JD^2 + d \cdot JD^3, \tag{6.1}$$

where JD is the Julian date (normalized to range $-1 \leq JD \leq 1$) and a, b, c and d are the fit parameters for the third degree polynomial. At the end of this procedure, we have a detrended light curve per filter for each star.

After this step *CDA* proceeds to remove the jumps. In order to identify the cleanest light curve for a reliable jump removal we create ”sub-light curves”, which we typical take with a duration of a day. Thus, for the IRa01 field we create 60 ”sublight” curves, called simply light curves in the following. These 60 blocks were selected after we checked various combinations. If the number of blocks are too large, then transit signals are reduced, and if the number of blocks are too small, the probability to include a jump in the ”sublight” curve increases. Let us assume that there are three full light curves for a given star in each band with N points per light curve; denote by $F_{R,i}$, $F_{G,i}$ and $F_{B,i}$ with $i = 1, N$ the individual data values in the red, green and blue filters, respectively. Then we divide each color light curve in 60 sub-light curves (one sub-light curve per day for IRa01 - 60 days). For each sub-light curve we calculate the mean value MR, MG and MB and normalize each sub-light curve by its mean value; we compute new, normalized sub-light curves NF through

$$NF_{R,G,B,i} = \frac{F_{R,G,B,i}}{M_{R,G,B}} \tag{6.2}$$

for each filter band and it is clear that all of these light curves have a mean of unity. This normalization is necessary since otherwise the whole process would be dominated by the light curve with the highest signal, which is usually the red light curve. As a side effect, *CDA* normalizes the depth of a possible transit in all filters using equation 6.2, so when the algorithm continues with its next steps, all transit events in each filter will have the same depth and thus *CDA* does not destroy real signals from the transits.

The normalized light curves have now the same mean, their dispersions will, however, differ. Our next goal is to identify the instrumental scatter, caused, for example by jumps, in each light curve and disentangle this instrumental scatter from statistical noise. In order to achieve this, *CDA* extracts five random packages of twenty adjacent points each from all colour bands and calculates the standard deviation of each package per filter; the result should represent a good estimate of the correct light curve value at that time. If we use many packages the probability to include jumps increases. The correct combination packages-points is a function of the duration of the jumps which is a random value, thus there is no a fix combination. We define as the mean standard deviation (MSD), the mean value of these five packages of each filter

$$MSD_{R,G,B} = \frac{1}{5}\sum_{j=1}^{5}\frac{1}{20}\sqrt{\sum_{i=k_j}^{k_j+20}(NF_{R,G,B,i} - Mean_{min})^2}, \tag{6.3}$$

where the induces k_j denotes 5 different random data points of the light curve and $Mean_{min}$ is the mean value of the flux of each package. In general, each filter has a different MSD value, which is compared with the standard deviation of each filter TSD defined through

$$TSD_{R,G,B} = \frac{1}{N}\sqrt{\sum_{i=1}^{N}(NF_{R,G,B,i} - Mean_{min})^2} \tag{6.4}$$

Finally, the relative standard deviation of each filter *RSD* is computed and defined by

$$RSD_{R,G,B} = \frac{TSD_{R,G,B}}{MSD_{R,G,B}}. \tag{6.5}$$

At the end of this process we have three normalized light curves $NF_{R,i}$ $NF_{G,i}$ and $NF_{B,i}$, and three values for the relative standard deviation RSD_R, RSD_G and RSD_B for each filter light curve respectively. *CDA* compares these three numbers and calls the light curve with the minimum *RSD* the base and the light curve with the maximum *RSD*, target. To make the procedure more understandable we continue with an example: Suppose the base is the blue light curve ($NF_{B,i}$) and the target is the red ($NF_{R,i}$) light curve. Using base and target *CDA* calculates a new mean light curve (AF_i); in our example *CDA* computes

$$AF_i = \frac{1}{2}(NF_{R,i} + NF_{B,i}). \tag{6.6}$$

and then it recalls the AF_i as the light curve with the maximum *RSD* (in this example recall AF_i as $NF_{R,i}$). According to assumptions 2 and 3, in the AF_i light curve remains any possible real signal but all the fake (jumps) tend to be reduced, because jumps appear only at specific times in each filter. As a final result we will have a red light curve reduced and two others (green and blue) untouched. If we try to run the algorithm again we will notice that the new values of *RSD* have changed because one light curve has changed. This means that every time we run the previous step of the algorithm, *CDA* removes a part of a fake signal (Fig. 6.3).

When these loops end, we re-normalize the final light curve of the red channel to the raw mean value,

$$NFR_{final} = NR \cdot NF_{R,i} \tag{6.7}$$

and the procedure has been completed. NFR_{final} is the final sub-light curve. The final step is to put all the 60 sub-light curves together. This is the final light curve and we are ready to search for exoplanets (Fig. 6.3). Of course we use many loops for procedure, but if we use too many, *CDA* starts to destroy the light curve because it is obvious that after some loops there is a "saturation" in the procedure. To avoid this effect, we do not use the same loop number of each light curve. We calculate the standard deviation of each light curve after each loop and *CDA* stops when the standard deviation starts to increases.

6.3.3 Simulations

In order to verify the functionality of CDA, we simulated CoRoT light curves as shown in Fig. 6.3. We specifically simulated a light curve in three filters (R,G,B), where jumps and trends appear at different times in each filter; also a long-term trend is included. In these light curve a transit pattern with period P=520 time units and a relative depth $\Delta Flux = 0.01$ is included. The transits are masked by the high noise. As can be seen in Fig. 6.3, all jumps are removed and the resulting output light curve shows some regions with higher noise and some others with lower noise, but this does not affect the real signal. Applying transit detection algorithms (e.g. Box Least Squares - BLS Kovács et al. 2002), the included transit pattern is also detected.

6.4 Results

In order to illustrate the algorithm with real light curves, *CDA* is applied to four CoRoT light curves, i.e., CoRoT0102702789, CoRoT0102874481, CoRoT0102741994 and CoRoT0102729260.

6.4.1 The case of CoRoT0102702789

In Fig. 6.4 we show the raw red light curve which includes a trend and jumps and the final light curve after applying *CDA* with 5 loops. The light curve of CoRoT012702789 has one huge jump around $JD \sim 2614$ and many other smaller jumps. The RSD_R value of the raw light curve is 5.048 and the final light curve is 0.95. Table 6.2 shows analytically the values of *RSD* from the total light curves, in these 10 loops of each filter. The green filter has the minimum value and thus *CDA* uses it as a base. The red filter on the other hand has the maximum value and we call it target, but in principal *CDA* defines different filters as base or target in each loop. For this reason in the first four loops the target is the red filter and base the green filter, then target changes to blue and green remains as base etc.; as already mentioned, the red light curve as the most common filter to search for transits.

The example of CoRoT012702789 shows us how *CDA* works and how it removes jumps from a distorted light curve. As far as we can tell from out reconstructed light curve, there are no clear flares or transits in the light curve of CoRoT012702789. The critical question at this point is how *CDA* works if the raw light curve has real events like transits.

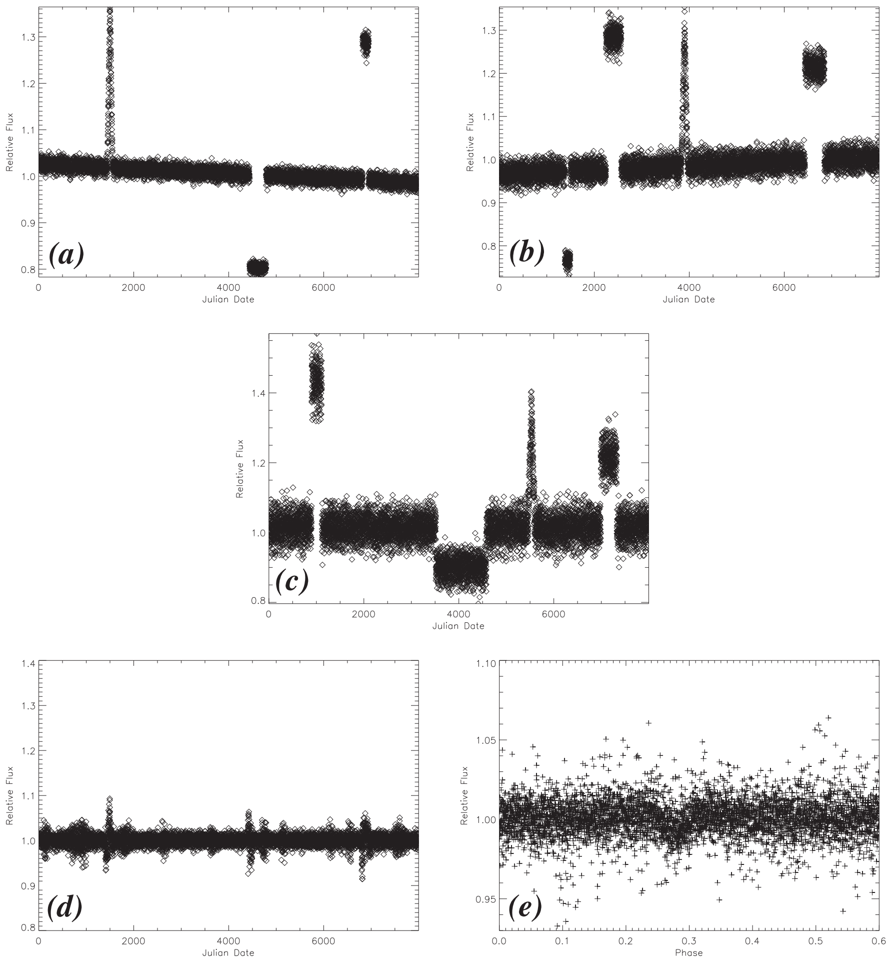

Figure 6.3: Simulated data. R - **(a)**, G - **(b)** and B -**(c)** color respectively. Plot **(d)** is the final light curve after CDA and the plot **(e)** is the phase diagram of the transit after CDA & BLS.

6.4.2 The case of CoRoT0102874481

An even more extreme case is CoRoT0102874481. The light curve of which is affected by many jumps; the raw (red) light curve of CoRoT0102874481 is shown in Fig. 6.5. In the raw data it is very difficult to distinguish real from instrumental events. As demonstrated in Fig. 6.5, *CDA* corrects all the jumps except for a real transit around $JD \sim 2612$. The standard deviation before and after *CDA* is 2203.13 and 336.44 ADUs, respectively. Only a small jump from green and blue filters remains at the end of light curve.

Because this transit is the only transit in the light curve, we cannot determine the period and the nature of the transiting object. Fig. 6.6 shows that *CDA* does not reduce the depth of the transit, which is $\sim$ 0.036. According to the CoRoT team (http://idoc-corot.ias.u-psud.fr), the host star's spectral type is A0IV. Assuming the typical radius and mass of such a star as $R_s = 4.4R_o$ and $M_s = 2.8M_o$ and assuming the transiting

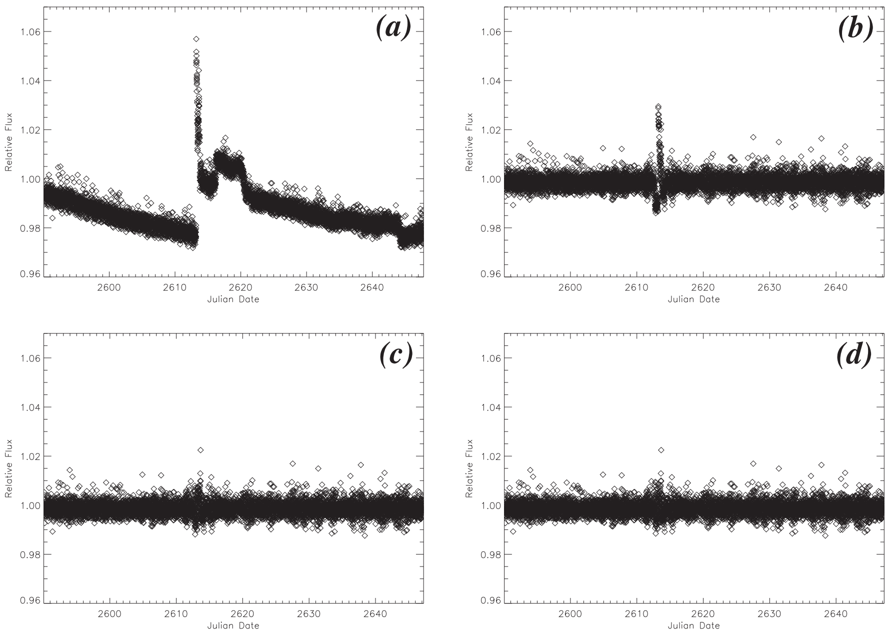

Figure 6.4: CoRoT012702789 red light curve and *CDA* results. Figure shows how *CDA* affects the light curve. Raw data - **(a)**, after 1 - **(b)**, 3 - **(c)**, 5 - **(d)** loops respectively. Almost all jumps are removed. Only one small jump remains at the end of the light curve.

object to be a true exoplanet, we determine the planet's radius as $R_p = 4.28R_J$ by using the relation between radius and transit depth (Seager & Mallén-Ornelas 2003).

$$R_p = R_s \cdot \sqrt{\Delta Flux}, \tag{6.8}$$

where R_s is the radius of the star and R_p is the radius of the planet. From Kepler's 3^{rd} law the semi-major axis of the orbit is $\alpha > 0.78AU$, because the period is $P > 60$ days.

6.4.3 The case of CoRoT0102741994

CoRoT0102741994 seems to be a binary system. Our main interest in this example is not to check if *CDA* can remove the jump but to check how the algorithm conducts the eclipses and the flux of the light curve. Fig. 6.7 shows how the algorithm converts the light curve. The light curve is affected only by a week jump ($\Delta Flux \sim 1.25\%$) around $JD \sim 2615$. The flux depth of the primary and secondary eclipse is 9% and 7%, respectively.

At the top figure is the light curve of the star before the application of *CDA*. The two eclipses are obvious, while the bottom figure shows the light curve after application of *CDA*. Clearly, the jump is removed completely. The depth of the primary and secondary eclipses now are 9.5% and 6.5% respectively. As a general result we can say that *CDA* does not remove the real signal but corrects the jumps.

Table 6.2: CoRoT01270289. Table 6.2 shows how *RSD* is changing in each loop. In the first four loops, red filter is the target and green the base. In loop five this situations has changed. Blue is the target now and green is the base. These values refers to the *RSD* values of the full light curve of each filter.

Loop No	RSD_R	RDS_G	RDS_B
♯1	**5.0485**	**0.9497**	1.0658
♯2	**1.8632**	**0.9497**	1.0658
♯3	**1.0665**	**0.9497**	1.0658
♯4	**0.9688**	**0.9497**	1.0658
♯5	0.9688	**0.9497**	**0.9868**

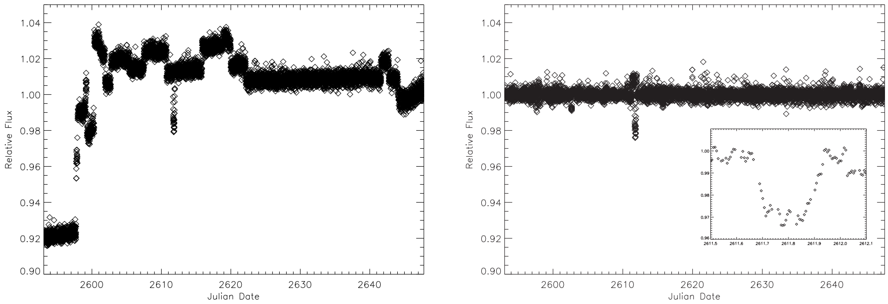

Figure 6.5: CoRoT012874481 - red filter Left : Raw data. Jumps do not let us decide which feature is a real event and which is not. Right: The same light curve after *CDA*. Almost all the jumps are removed from the raw data. A clear transit is appearing. The subframes is a zoom-in plot.

6.4.4 The case of CoRoT0102729260

Finally, the case of CoRoT0102729260, is a combination of strong and weak jumps and trends. The raw light curve of CoRoT0102729260 does not show any transits. It is interesting to note that a transit detection algorithm like BLS does not detect any transit event in this light curve (Fig. 6.9, left panel). However, having applied *CDA* to remove all jumps, we implement again BLS on the final light curve and a possible transit appears (Fig. 6.8, right panel).

This transit is only detectable after applying *CDA*, but not in the raw data. Our analysis of the phased light curve suggests are period of $P = 1.6986$ days. The photometry by the CoRoT team (http://idoc-corot.ias.u-psud.fr) provides some information for the parameter of the host star, which appears to be a main sequence star (G5V) of apparent brightness $m_V = 14.772$ mags. Assuming the spectral type to be correct, we can estimate the radius of the star $R_s \sim 0.91 R_o$. With a transit depth of $\Delta Flux = 0.004$, we deduce a planetary radius of $R_p = 6.27 R_E$ applying Eq. 6.8. Fig. 6.10 shows the phase folded light curves. Also Table 6.3 gives some additional information of the system.

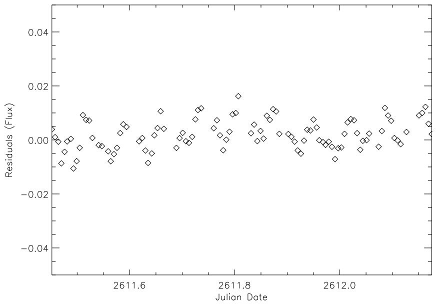

Figure 6.6: CoRoT012874481 residuals before minus after *CDA*. The signal from the real transit is not reduced by the algorithm.

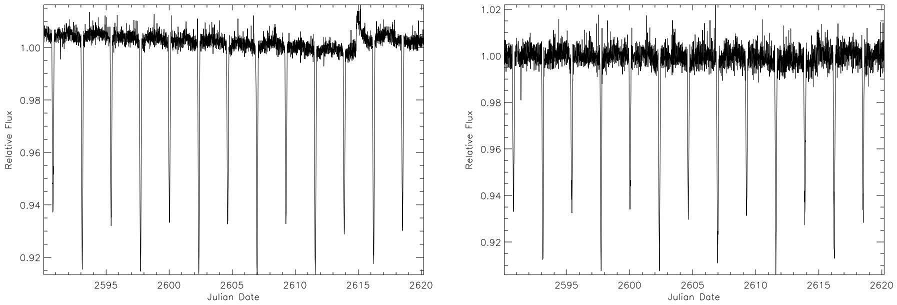

Figure 6.7: CoRoT012741994 - red filter Left: Raw data. We just remove all the “bad points”. The light curve suffers from one jump around $JD \sim 2615$ and a trend. Right: The same light curve after *CDA*. The jumps is reduced. *CDA* does not effects the transit depth.

6.5 Conclusions

We have introduced and presented a method dubbed *CDA* that removes instrumental artefacts from CoRoT data and demonstrated its usefulness in some practical applications. We emphasize that the *CDA* algorithm prepares CoRoT data for any transit detection; it should not be used for transit analysis since it is contingent to remove some real signal. Of course this is not a problem for the detection inasmuch instrumental jumps destroy much more the light curve. From our study of 1030 light curves in the first CoRoT field (IRao01) we found that only very few light curves have no instrumentally caused features and remain as they are, while the vast majority of light curves are appreciably improved. We present some examples which show how the algorithm affects the light curves. Our main theme is that instrumental jumps substantially affect the CoRoT light curves, making a transit detection in fainter stars impossible. We prove our case with the example of CoRoT0102729260, a possible candidate exoplanet which is detected only after applying *CDA* on the raw data.

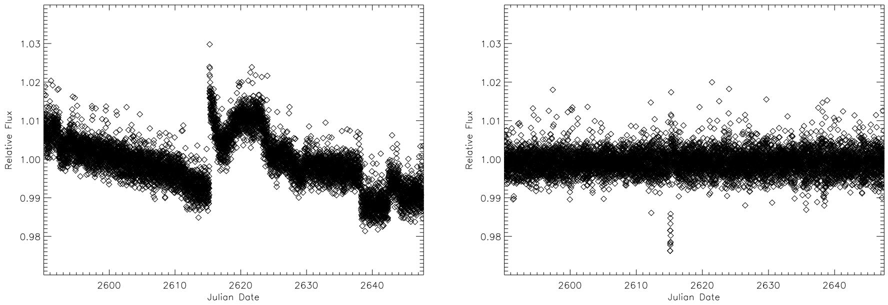

Figure 6.8: CoRoT0102729260 - red filter. Left: Raw data before *CDA*. Right: Final light curve after *CDA*. The algorithm succeed to remove all the jumps and trends and improve the light curve enough to detect the “concealed” transit.

Table 6.3: Physical Parameters of CoRoT0102729260.

Color Index	0.752
Star Radius R_s	$0.91R_o$
Period	1.6986 *days*
Planet Radius R_p	$6.27R_E$
Depth (*Flux*)	0.004

6.6 Acknowledgements

DM was supported in the framework of the DFG-funded Research Training Group ”Extrasolar Planets and their Host Stars” (DFG 1351/1).

6.7 References

Aigrain, S., Pont, F., Fressin, F., et al. 2009, A&A, 506, 425
Baglin, A., Vauclair, G., & CoRoT team, 2000, Journal of Astrophysics and Astronomy, 21, 319
Ulrich, E. J. Rhodes, Jr., & W. Dappen, 426
Kovács, G., Zucker, S., & Mazeh, T. 2002, A& A, 391, 369
Pinheiro da Silva, L., Rolland, G., Lapeyrere, V., & Auvergne, M. 2008, MNRS, 384, 1337
Seager, S. & Mallén-Ornelas, G. 2003, ApJ, 585, 1038

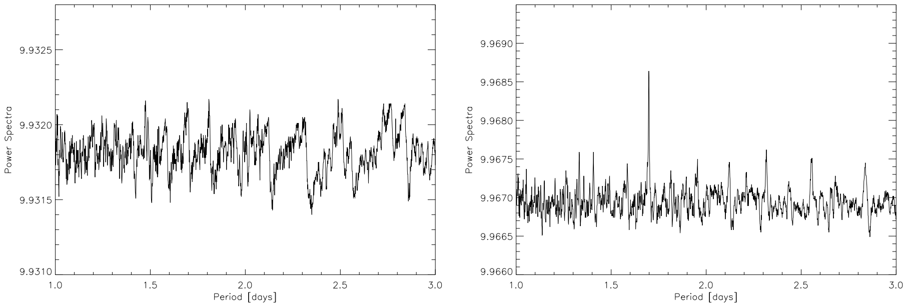

Figure 6.9: CoRoT0102729260 - red filter. Left: Periodogramm of the raw light curve before *CDA* without any obvious signal. Right: Same plot after *CDA*. A clear periodic signal ($P \sim 1.698$) is detected.

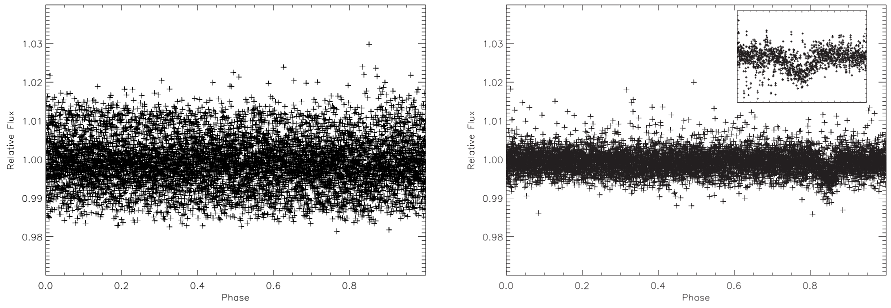

Figure 6.10: CoRoT0102729260. Left: A Phase folded light curve before *CDA*. Right: A phase folded light curve after *CDA*. A transit event around phase $\sim$ 0.85 clearly appears.

Chapter 7

Planetary albedo and eccentricity determination of exoplanets

D. Mislis, R. Heller & J.H.M.M. Schmitt

Astronomy & Astrophysics, submitted : 4 May, 2010

LETTER TO THE EDITOR

Planetary albedo and eccentricity determination of exoplanets

D. Mislis[1], R. Heller[1] & J.H.M.M. Schmitt[1]

[1]Hamburger Sternwarte, Gojenbergsweg 112, D-21029 Hamburg, Germany
email : mdimitri@hs.uni-hamburg.de

ABSTRACT

We present a new approach to estimate the parameters of transiting extrasolar planetary systems using photometric light curves (LCs). The first results of the current space-based missions CoRoT and Kepler reveal a previously unknown wealth of details in the LCs. An analysis that combines a treatment of various phenomena in these LCs, such as primary and secondary eclipses, as well as the overall shape of a LC between the occultations, allows for a derivation of orbital and physical parameters. The complete decryption of a LC yields information about eccentricity, orientation of periastron, and the planet's albedo. These parameters were impossible to be extracted from low-accuracy data of ground-based surveys. Here, we give a self-contained set of equations for the determination of orbital and planetary parameters and present simulations for high-accuracy LCs. For our procedure, we do not use the timing of the primary and secondary eclipses to constrain the eccentricity. Our analysis shows that the minimum accuracy of the observational data to be useful for an application of our method is 10^{-4}, which coincides with the accuracy of the Kepler mission. Future space missions, such as the James Webb Space Telescope, with photometric accuracies of about 10^{-7} can reduce the error in all parameters.

Keywords Stars: Planetary systems, flares

7.1 Introduction

As yet, two observational methods have dominated the studies of extrasolar planets: radial velocity (RV) measurements and transit light curve (LC) analyses. Both have advantages and disadvantages. While the RVs provides estimates of the planetary mass ($M_{\rm p}$), the eccentricity (e) and the semi-major axis (a), it does not constrain the inclination of the orbital plane with respect to the observer (i), thus only lower limits to $M_{\rm p}$ can be determined. The transit method, on the other hand, provides information on i, the ratio of the planetary radius and the stellar radius ($R_{\rm p}/R_{\rm s}$), and the duration of the transit (D). So far, only a combination of both strategies yielded a full set of orbital and physical parameters for extrasolar planets.

Currently, there are two space missions aiming at the detection of extrasolar planet transits in front of their host stars: CoRoT launched in 2006 (Deleuil et al. 1997) and Kepler launched in 2009 (Borucki et al. 1997). Their instruments are monitoring thousands of stars, supposed to yield hundreds of transit events, whose RV follow-up could take years. Since only RV measurements allow planetary mass determinations, the most fundamental parameter of an extrasolar planet remains undetermined; the is the crucial parameter classifying an object as a planet, brown dwarf or a star. Some transiting planets have been subject to detailed studies and various observational techniques, such as transmission spectroscopy during the primary transit and infrared observations of the secondary eclipse (Snellen et al.2009). In addition, high-accuracy photometry

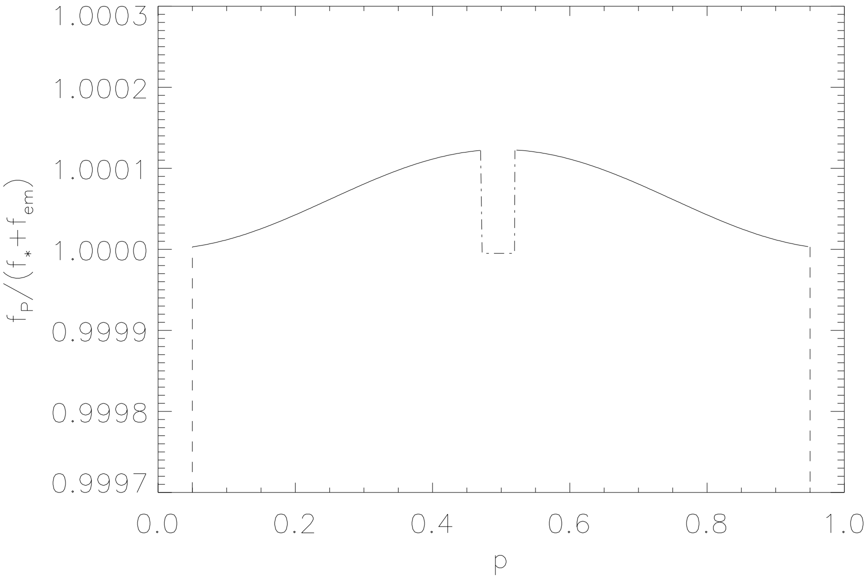

Figure 7.1: The current transit model includes the primary transit f_1 (dashed line centered at orbital phase $p = 0$), the secondary eclipse f_2 (dashed-dotted line around $p = 0.5$) and the reflected light from the planet f_3 (solid line).

has proven that the planetary thermal emission as well as the reflection of the stellar light from the planet are detectable. In this study, we demonstrate the wealth of information that is hidden in high-accuracy LCs and show that a lot of information that is normally obtained from RV follow-up can actually be obtained from high-precision photometry.

7.2 Theoretical background

7.2.1 Transiting Planets

Standard models of LCs that have been used before the advent of space missions based on a flat curve out of transit and a limb darkening during the transit. Seager & Mallen-Ornelas (2002) proved analytically that each transiting system shows a unique LC. Analyses of high-accuracy data from space required a revision of this simple approach. Nowadays, models incorporate the reflected light from the planet, which deforms the overall shape of the LC, and the secondary eclipse (Fig. 7.1).

In Fig. 7.2 we show the geometry of an arbitrary transiting system assuming an elliptical orbit. Let i denote the angle between the observers's line of sight and the orbit plane normal, the angle between the observer's line of sight projected onto the orbit plane and the periastron is labeled ω. The star is in the center of the reference frame and d is the distance between the star and the planet; the distance between the star and the planet during the primary transit is denoted by $d_{\star,\mathrm{p}}^{\mathrm{PT}}$, during the secondary eclipse both bodies are separated by the distance $d_{\star,\mathrm{p}}^{\mathrm{SE}}$.

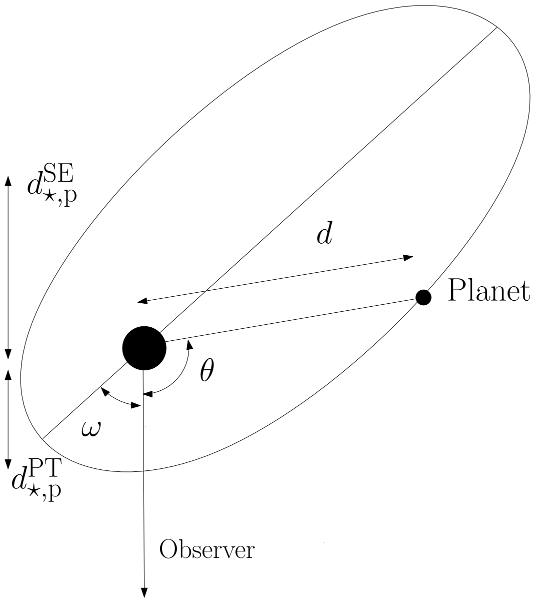

Figure 7.2: This sketch of the transiting planetary system as seen from above explains the variables used in our calculations.

To decode the geometry of the system from the LC we split it into three sub LCs. The light curve f_1 describes the course of the primary transit, when the star blockes the planet's light, f_2 describes the form of the secondary eclipse, when the star blocks and planetary light, and f_3 the rest of the light curve, when both star and planet contribute to the total light.

$$D \simeq \frac{PR_\star}{\pi a^2} \frac{d_{\star,\mathrm{p}}^{\mathrm{PT}}}{\sqrt{1-e^2}} \sqrt{\left(1+\frac{R_\mathrm{p}}{R_\star}\right)^2 - b^2}, \tag{7.1}$$

where P is the orbital period, $R_\star$ and R_p are the radius of the star and the planet, respectively, e is the orbital eccentricity, i is the inclination of the orbital plane with respect to the observer's line of sight, and $b = d_{\star,\mathrm{p}}^{\mathrm{PT}} \cos i / R_\star$ is the impact parameter. To model the shape of the primary transit, f_1, we use Eq. 7.1 (Ford et al. 2008) and the limb darkening equation

$$\frac{I_\mu}{I_0} = 1 - u_1(1-\mu) - u_2(1-\mu)^2, \tag{7.2}$$

with u_1 and u_2 as the two limb darkening coefficients (Claret 2004; Sozzeti et al. 2007), μ as the cosine of the angle between the surface normal and the observer, and I_0 and I_μ as the intensities at the stellar disk center and at μ, respectively. Once the period is known from observations, one can fit the model to the observations to deduce $R_\star$, R_p, i, and $d_{\star,\mathrm{p}}^{\mathrm{PT}}$. The transit of the secondary eclipse, f_2, is fitted with the same model but without effects of limb darkening.

The total light curve f_3 contains a contributions from the star, which we assume to be constant, a contribution from reflected light, which is phase dependent, and possibly contributions from intrinsic planetary emission, which depends sensitively on the spectral range considered. The phase pattern of the reflected stellar flux depends on the phase angle α, i.e., the angle between star and observer as seen from the planet. Counting the orbital phase θ from primary minimum, the angles α, i and θ are related through

$$\cos(\alpha) = -sin(i)\cos(\theta). \tag{7.3}$$

The reflected flux f_{ref} can then be expressed as

$$f_{\mathrm{ref}}(\alpha) = \alpha_{\mathrm{g}} f_{\star} \left(\frac{R_{\mathrm{P}}}{2d}\right)^2 \Phi(\alpha), \tag{7.4}$$

where α_{g} is the geometric albedo of the planet, $f_{\star}$ is the stellar flux at a distance d from the star, and $\Phi(\alpha)$ the so-called phase function. It is not entirely clear what phase functions should be used for the description of extrasolar planets. A popular choice is to assume

$$\Phi_L(\alpha) = \frac{1}{\pi}\left(\sin\alpha + (\pi - \alpha)\cos\alpha\right), \tag{7.5}$$

which models the planet as a Lambert sphere, assuming that the intensity of the reflected light is constant. An alternative choice would be

$$\Phi_C(a) = \frac{1}{2}\left(1 + \cos(\alpha)\right), \tag{7.6}$$

which assumes that the reflected light is simply proportional to the size of the star-lit crescent, and many other choices of phase functions are possible.

We next note that the combination $\omega + \theta$ is related to the eccentric anomaly E through

$$\omega + \theta = 2\tan^{-1}\left(\frac{\sqrt{1+e}}{\sqrt{1-e}}\tan(E/2)\right), \tag{7.7}$$

and E is related to the meam anomaly M through Kepler's equation

$$E = M - e\cos(E). \tag{7.8}$$

We normalise - as usual - the LC by the stellar flux, which can be determined as the minimum flux observed during secondary transit:

$$f_3(\theta) = \frac{f_{\star} + f_{\mathrm{ref}} + f_{\mathrm{em}}}{f_{\star}}. \tag{7.9}$$

The question of intrinsic emission from extrasolar planets is a bit more complicated. Clearly we expect those planets just like the solar system planets to be in equilibrium in the sense that the absorbed stellar flux must be re-emitted. If we assume a fast rotating planet this reemission should take place more or less homogeneously over its entire surface and this thermal flux should be almost constant with phase. If, on the other hand, we consider the case of a rotationally locked planet, one expects significant temperature changes between day and night side and hence the emitted thermal flux should show a phase dependence similar to the the reflected star light.

Combining Eqs. (7.4) - (7.9), we can derive the equation for the total flux from the planet ($f_{em} = 0$).

$$f_3(\alpha) = 1 + \frac{a_{\mathrm{g}}\Phi(\alpha)R_{\mathrm{p}}^2}{4(r_{\star} + r_{\mathrm{p}})^2}. \tag{7.10}$$

While R_p and $\sin i$ are known from the primary transit, Eq. (7.10) can be used to draw five more parameters from a model fit to the observations: e, a_1, a_2, ω, and α_g. So far, we have constructed models that can be fitted to the observed curves of the primary transit f_1, to the secondary eclipse f_2, and to the overall shape f_3. But there is more information hidden in the LC. In the last moments before (or after) the secondary eclipse $\alpha = \alpha_S$ $(\theta = \pi)$, so that the normalized total flux becomes

$$f_3(\alpha_S) = 1 + \frac{1}{4}\left(\frac{R_\mathrm{p}}{d^{\mathrm{SE}}_{\star,\mathrm{p}}}\right)^2 \left(a_\mathrm{g}\Phi(\alpha_S)\right). \tag{7.11}$$

In the ideal, noiseless case $f_3(\alpha_S)$ is the last data point before the ingress of the secondary eclipse as well as the first data point afterwards. Using Eqs. (7.10) - (7.11) we rewrite Eq. (7.10) as

$$f_3(\alpha) = 1 + (f_3(\alpha_S) - 1)\left(\frac{1 + e\cos(\omega + \theta)}{1 - e\cos(\omega)}\right)^{-2} \frac{\Phi(\alpha)}{\Phi(\alpha_S)} \tag{7.12}$$

From the equation above we are able to measure eccentricity and ω of the planetary orbit and using information from the primary transit modeling ($\gamma = \alpha/R_\mathrm{p}$) we could re-write Eq. 7.11 as the planet.

$$a_\mathrm{g} = \gamma^2\left(\frac{1 - e^2}{1 - e\cos(\omega)}\right)^2 \left(\frac{f_3(\alpha_S) - 1}{\Phi(\alpha_S)}\right) \tag{7.13}$$

This system of equations shows that LCs of transiting extrasolar planetary systems alone already provide access to some more physical and orbital parameters such e, ω and α_g.

7.2.2 Non-Transiting Planets

Clearly, if photometric accuracy is high enough to detect the reflected light from the planet, many non-transiting planets will be discovered. From a non-transiting planet LC we can expect many information but using equation Eq. 7.12 we are able to measure eccentricity, ω and the inclination of the orbit because inclination is a function of the orbital phase α (Eq. 7.3). For R_p (and for the mass) RV follow-up observations are nessesery. The next section will be devoted to the observational accuracy that is necessary to yield robust parameterizations.

7.3 Simulations - Results

To test our model, we simulate two LCs using the equations above. One of the underlying planetary systems is an analog to the transiting hot Jupiter HAT-P-2b (Pál et al. 2009), whereas the other one resembles the transiting Super-Earth CoRoT-7b (Queloz et al. 2009) (Table 7.1). We customized these models in terms of the geometric albedo, for which we optimistically applied $\alpha_\mathrm{g} = 0.3$ in both cases (Sudarsky et al. 2000). Though observations of CoRoT-7b are reconcilable with $e = 0$, we chose $e = 0.05$. After all, we are not heading for a reconstruction of these systems but we want to estimate how accurate comparable systems could be parameterized and, as an example, if a putative eccentricity of CoRoT-7b could be determined.

Table 7.1: Physical parameters of our two models.

Stellar parameter	hot Jupiter	Super-Earth
$R_\star$	$1.64\,R_\odot$	$0.87\,R_\odot$
$M_\star$	$1.36\,M_\odot$	$0.93\,M_\odot$
$T_{\mathrm{eff},\star}$	6290 K	5275 K

Planetary parameter	hot Jupiter	Super-Earth
R_p	$1.16\,R_\mathrm{J}$	$0.15\,R_\mathrm{J}$
M_p	$9.08\,M_\mathrm{J}$	$0.0151\,M_\mathrm{J}$
α_g	0.30	0.30
u_1	0.34	0.20
u_2	0.35	0.57

Orbital parameter	hot Jupiter	Super-Earth
P	5.63347 d	0.85360 d
i	86.72°	80.10°
e	0.52	0.05
ω	185°	5°

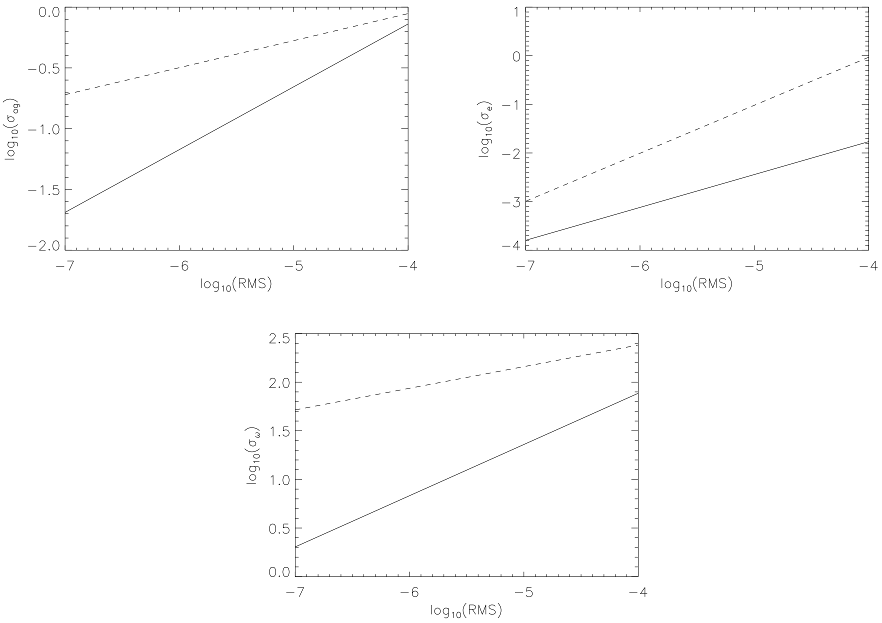

Figure 7.3: Errors in a_g, e, and ω as functions of data accuracy. The solid line denotes the HAT-P-2b twin while the dashed line labels the CoRoT-7b analog.

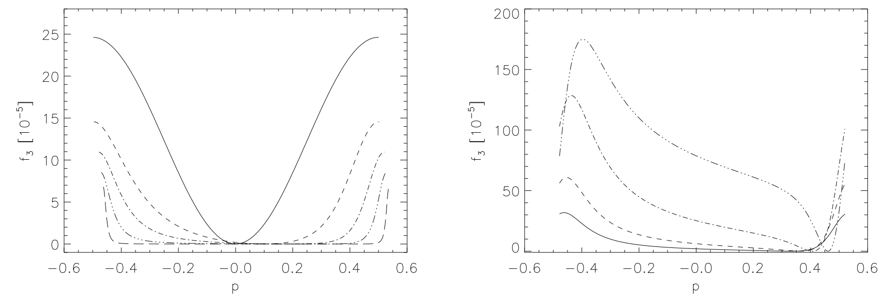

Figure 7.4: Contribution of the phase-dependent flux f_3 to LCs without transits. *Left:* f_3 for various eccentricities (from above: $e = 0.0,\ 0.3,\ 0.5,\ 0.7,\ 0.9$) while ω is fixed to 0. *Right:* f_3 for various orientations of periastron (from above: $\omega = 50°,\ 70°,\ 100°,\ 140°$) while e is fixed to 0.5.

To these models, we add increasingly more noise to simulate a data accuracy between 10^{-7} and 10^{-4}. The phase effect in the LCs, i.e. the contribution of f_3, is significant only for accuracies $\lesssim 10^{-4}$, which is why this phenomenon could not be detected in the LCs of CoRoT (Costes et al. 2004). We then fit the noiseless model from Sect. 7.2.1 to each of these – more or less – noisy LCs and use 1000 Monte Carlo simulations to calculate the standard deviations for each parameter in each fit. For the transit fits we use the model of Pál (2008). With this procedure, we simulate the standard deviation as a function of data accuracy.

In Fig. 7.3 we show the standard deviations resulting from these fits for the planetary geometrical albedo a_g (σ_{a_g}), eccentricity (σ_e), and orientation of periastron (σ_ω) as a function of the root mean square (RMS) of the data. With an accuracy provided by the current Kepler mission of 10^{-4}, the eccentricity of a CoRoT-7b-like planet could merely be determined with a useless standard deviation of roughly 0.8. For a planet similar to HAT-P-2b, however, the standard deviation in e is only about 0.08. The orientation of periastron for the CoRoT-7b twin could be constrained to approximately ±50° while for the HAT-P-2b analog the accuracy is as low as 5°. Restrictions of the geometrical albedo a_g are ±0.02 in the best case (Hot jupiter - RMS 10^{-7}) to ± 1.0 in the worst case (Earth like - RMS 10^{-4}) with no physical meaning.

High-accuracy LCs of transiting systems, as shown in Fig. 7.1, provide a complete set of orbital and physical parameters. For the case of a non-transiting exoplanet one still might be able to detect variations in the overall shape of the LC, f_3. In this case, two more parameters, namely f_2 and Δf, would have to be fitted since they cannot be inferred directly from the LC and furthermore RV follow-up would be necessary for an assessment of the companion's nature – whether it would be a star or a substellar object. But anyway, e and ω can nevertheless be estimated from observations of f_3 alone. In Fig. 7.4 we show the contribution of f_3 to the LC (for HAT-P-2b system) in a system with high inclination and without a transit for various values of e and ω.

We applied our model to Kepler's TrES-2b light curve (http://archive.stsci.edu). TrES-2b light curve does not show any reflacted light or secondary eclipse. We found an upper limit for the TrES-2b albedo equal $a_g = 0.04$ which confirms Cowan & Agol (2010) and the value of $a_g = 0.03$.

7.4 Conclusions

The mathematical tools presented in this article can be used for a complete parametrization of transiting exoplanet systems on the basis of high-accuracy LCs. In our model, RV measurements are not necessary to constrain the eccentricity (e), the orientation of periastron (ω) and the geometric albedo of the planet (α_{g}). Our model also incorporates the characterization of the ratio of planetary and stellar radius ($R_{\mathrm{p}}/R_{\star}$), orbital period (P), and the orbital inclination (i).

The current space missions Kepler could provide the first transiting planets to which our procedure can suitably applied. Our technique will benefit from future space missions such as the James Webb Space Telescope (Deming et al. 2009) with RMS $\lesssim 10^{-6}$.

7.5 Acknowledgements

D. Mislis and R. Heller are supported in the framework of the DFG-funded Research Training Group ”Extrasolar Planets and their Host Stars” (DFG 1351/1).

7.6 References

Borucki, W. J., Koch, D. G., Dunham, E. W., & Jenkins, J. M. 1997, in Astronomical Society of the Pacific Conference Series, Vol. 119
Claret, A. 2004, A&A, 428, 1001
Costes, V., Bodin, P., Levacher, P., & Auvergne, M. 2004, in ESA Special Publication, Vol. 554, 281284
Cowan, N. B. & Agol, E. 2010, ArXiv e-prints
Deleuil, M., Barge, P., Leger, A., & Schneider, J. 1997, in Astronomical Society of the Pacific Conference Series, Vol. 119
Deming, D., Seager, S., Winn, J., et al. 2009, PASP, 121, 952
Ford, E. B., Quinn, S. N., & Veras, D. 2008, ApJ, 678, 1407
Pál, A. 2008, MNRAS, 390, 281
Pál, A., Bakos, G. A., Torres, G., et al. 2009, MNRAS, 1781
Queloz, D., Bouchy, F., Moutou, C., et al. 2009, A&A, 506, 303
Seager, S. & Mallen-Ornelas, G. 2002, in Bulletin of the American Astronomical Society, Vol. 34
Snellen, I. A. G., de Mooij, E. J. W., & Albrecht, S. 2009, Nature, 459, 543
Sozzetti, A., Torres, G., Charbonneau, D., et al. 2007, ApJ, 664, 1190
Sudarsky, D., Burrows, A., & Pinto, P. 2000, ApJ, 538, 885

Chapter 8

The Photometric Software for Transits (PhoS-T)

D. Mislis, J. Fernandez, R. Heller & U. Seemann

Astronomy & Astrophysics, submitted 23 March 2010

The Photometric Software for Transits (PhoS-T). Precise transit timing for the extrasolar planet XO-2b[1]

D. Mislis[1], J. Fernandez[2], R. Heller[1] & U. Seemann[2]

[1]Hamburger Sternwarte, Gojenbergsweg 112, D-21029 Hamburg, Germany
email : mdimitri@hs.uni-hamburg.de
[2]Institut für Astrophysik, Georg-August-Universität Göttingen, 37077 Göttingen, Germany

Submitted : 23 March 2010

ABSTRACT

We present the Photometric Software for Transits (Phos-T), a user-friendly stand-alone astronomical software built to study in detail photometric data of transiting extra-solar planets. Through a simple and clean graphical environment, PhoS-T can perform data calibration, point-source differential photometry, and transit light curve modeling. The software also includes a special mode optimized to analyze public data from the CoRoT mission. Here we present a detailed description of the software, together with the analysis of a recent transit of the extra-solar planet XO-2b, observed with the MONET robotic telescope. The results obtained using PhoS-T are in good agreement with previous works, and provide a precise time-of-transit for XO-2b.

Keywords Methods: data analysis – Techniques : photometry – Stars : planetary systems

8.1 Introduction

Transiting extra-solar planets provide an enormous amount of information if compared to non-transiting systems, like mass, radius, chemical composition, surface temperature, orbit-rotation inclination, etc. (Charbonneau et al. 2007). In the past 10 years, several research groups have invested a significant amount of resources in order to detect transiting systems (Udalski et al. 1992, McCullough et al. 2004, Street et al. 2003, Bakos et al. 2002). Dedicated space telescopes have been put in orbit to detect more of these systems (Deleuil et al. 1997, Borucki et al. 1997), and follow-up observing programs using ground- and space-based instruments have been crucial for our understanding of these distant worlds (McDowell 2001, Gehrz et al. 2004).

An interesting development in the field of transiting extrasolar planets is the participation of several small observatories in the follow-up programs (e.g. the Fred L. Whipple Observatory, FLWO in the following). Most of the systems discovered by TrES, XO, WASP and HAT have magnitudes between $V = 10^{\mathrm{m}}$ and 13^{m}, a range where millimagnitude relative photometry can be achieved with 1m-class telescopes. This level of photometric precision allows a detailed modeling of the transit light curves, and precise measurements of the duration and time of the transits ($\sim 30\,\mathrm{s}$ for events longer than 2 hrs). Significant differences between observed and expected values for timings and duration of transits could indicate the presence of an additional object in

---

[1] PhoS-T is an open-source software, available at `http://www.hs.uni-hamburg.de/grk/phost`.

a planetary system, which can have a mass as low as the Earth. The potential of 1m-class telescopes should not be underestimated, but the impact of their contributions depends strongly on the quality of the analysis of their data, and how fast their results can become public.

In this context, we present PhoS-T, a user-friendly stand-alone astronomical software built to study in detail photometric data of transiting extra-solar planets. PhoS-T can perform high-quality data calibration, point-source differential photometry, and transit light curve modeling in a very short time, using a simple and clean graphical environment. PhoS-T comes from ”**Pho**tometric **S**oftware for **T**ransits”, and takes its name from the Greek word for light (Phos=ΦΩΣ=light).

8.2 Theoretical background

8.2.1 Data reduction function

The first mode of PhoS-T is based on a standard procedure of data reduction. The input data is a fits file, which is passed through standard bias subtraction, dark correction, and flat fielding. The function *Data reduction* uses the two sub-routines *Master Frames* and *Noise Reduction*. *Master Frames* creates the master noise frames. For the purpose of bias subtraction, it creates an average bias value $B_{i,j}$ for each pixel, where the index i runs through the columns and j runs through the lines of the image. With N as the total number of bias frames taken and $b_{i,j}$ as the individual bias values we get

$$B_{i,j} = \frac{1}{N}\sum_{k=1}^{N}(b_{i,j})_k. \tag{8.1}$$

We call this averaged bias frame the master bias. To obtain the master dark ($D_{i,j}$) and the master flat ($F_{i,j}$) frames, we use similar equations

$$D_{i,j} = \left(\frac{1}{N}\sum_{k=1}^{N} d_{i,j}c_k\right) - B_{i,j}$$

&

$$F_{i,j} = \frac{1}{\overline{F}}\left(\frac{1}{N}\sum_{k=1}^{N}(f_{i,j})_k c_f\right) - B_{i,j} - D_{i,j}$$

where $c_k = 1/(t^{\mathrm{D}}_{\mathrm{exp}})_k$ normalizes the exposure time of the kth dark frame and $c_f = 1/(t^{\mathrm{F}}_{\mathrm{exp}})_k$ which normalizes the exposure time of the kth flat frame. Moreover, $(d_{i,j})_k$ and $(f_{i,j})_k$ are the dark and flat pixels of the kth dark and flat field image and $\overline{F}$ is the mean value of the sum of all flat frames.

The second sub-routine, *Noise Reduction*, then extracts the reduced light $L_{i,j}$ frame via

$$L_{i,j} = \frac{R_{i,j} - B_{i,j} - D_{i,j}t^{\mathrm{R}}_{\mathrm{exp}}}{F_{i,j}}, \tag{8.2}$$

where $R_{i,j}$ is the jth pixel in the ith column of the raw science image and the $t^{\mathrm{R}}_{\mathrm{exp}}$ is the exposure time of each light frame. Finally, PhoS-T applies a “hot pixel” algorithm to remove all the bad pixels from the image. We use a mask of 10 × 10 pixels, which is applied to each pixel brighter than 40 000 analog-to-digital units (ADUs). This mask estimates how isolated these potentially bad pixels are or if they might be part of a point spread function (PSF).

8.2.2 Align function

For the parametrization of transiting exoplanet systems, telescopes with mirrors larger than 1 m are typically being used nowadays. These are significantly larger and have a much smaller field of view (FOV) than the instruments used by most survey teams, which prefer large FOVs and very often lenses instead of mirrors. The photometric data obtained for the detailed (follow-up) characterization of the transit is thus assumed to be not crowded with stars. Based on this assumption, the *Align* function of PhoS-T includes the two sub-routines *Offset & Rotation* and *Target & Comparison Selection*. The former one selects the two brightest stars of the FOV by

$$S_i = \sum_{j=1}^{J} L_{i,j} \quad , \quad 1 \leq i \leq I \& S_j = \sum_{i=1}^{I} L_{i,j} \quad , \quad 1 \leq j \leq J$$

where S_i and S_j are the sums of ADUs per column and line and I and J are the number of columns and lines of the frame, respectively (typically $I = J$). The impact of bad pixels is diminished to insignificance because we are using the sum of a full line or column. As an output we have two graphs with various peaks (Fig. 8.1). Each peak represents to a star of which PhoS-T selects the two highest for the alignment of the images. The combination of the two largest peaks in both dimensions yields the coordinates of the two brightest stars. If, for any reason, a combination of the two brightest stars does not suit well – they might be located at the edge of the frame or the tracking might be bad – the software selects the next most plausible pair of bright stars. With two stars as references we can then calculate the offset and the rotation angle of each frame with respect to the reference frame. Figure 8.2 shows an example for the offset in both axes. Moreover *Offset & Rotation* has a focus on the center of the CCD to minimize the risk that the reference stars might move outside the frame in the course of the observation. If the offset is large enough to set the reference stars out of the FOV, this frame is ignored and labeled as "bad frame".

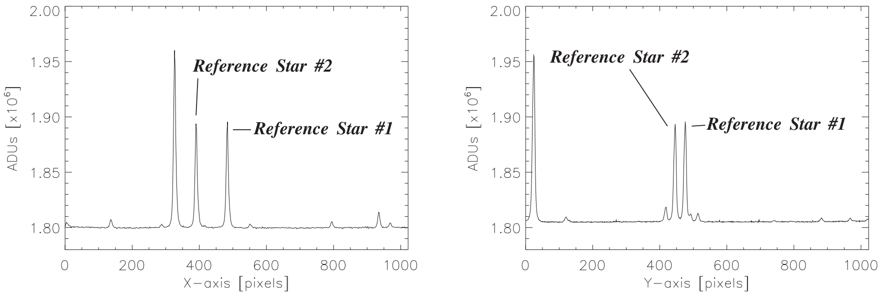

Figure 8.1: Sum of ADUs per line (left panel) and column (right panel) for the reference frame. As an example we point out the two brightest stars which serve as reference for the orientation of the frame.

With the *Target & Comparison Selection* the user chooses the window for the transit analysis. First, the reference frame appears divided into four sub-frames, one of which

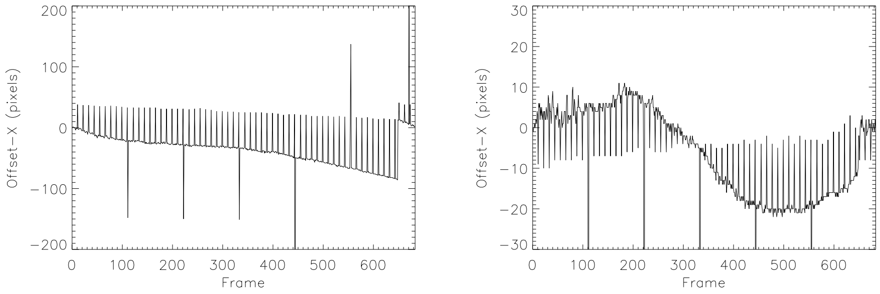

Figure 8.2: Offset in both image dimensions after application of the *Offset & Rotation* function. The plots show the shift in X-axis (left panel) & Y-axis (right panel) as a function of frame number. In both dimensions MONET shows a guiding periodic offset (varius peaks).

contains the target star to be selected by the user. The new sub-frame is again divided into four sub-frames and the user zooms in until only the target remains (Fig. 8.3). The same technique is applied for the comparison star. Finally, the user has defined the photometric window and a comparison star, which is why PhoS-T does not use apertures for photometry. The same technique is applied to the comparison star. Finally, the user has defined the photometric window and a comparison star. This is why PhoS-T does not use apertures for photometry. Although we confined to one comparison star in our example, the user can select as many references as he/she wants to.

8.2.3 Photometry function

The *Photometry* function uses the three sub-routines *Aperture Photometry*, *Time & Airmass*, and *Final LC*, where LC stands for light curve. The *Aperture Photometry* is different from the usual methods (Mighell 1999). First, it calculates the frame coordinates of the target star and then applies the *Offset & Rotation* sub-routines of the *Align* function to each frame. Then, it finds the new coordinates of the star and creates a sub-frame with the same measures as the photometric window. The software now finds the standard deviation σ_{sky} of the sky using the pixel values of the sky background:

$$\sigma_{\mathrm{sky}} = 0.5 * \left(\sqrt{\frac{1}{i} \sum_{i} (G_{i,1} - \bar{G})^2} + \sqrt{\frac{1}{j} \sum_{j} (G_{1,j} - \bar{G})^2} \right), \qquad (8.3)$$

with $G_{i,j}$ as the value of the background in the i, jth pixel and $\bar{G}$ as the mean value of the sky background of the first column and line in the photometric window. All the pixels with values 1.5 σ higher than $\bar{G}$ are replaced with the new sky values. To derive the new sky values, we are using random numbers from a Gaussian distribution where σ equals with the sky standard deviation σ_{sky}. The new frame is called *Sky Frame*. The *Sky Frame* is subtracted from each raw frame. The result of this subtraction, the *Final Frame* with values $\mathfrak{f}_{i,j}$, has a very dim background and an enhanced contrast to the flux values of the target. With this method it is not necessary to define an aperture because the flux of the star $\mathfrak{F}$ is the sum of all pixel values in the *Final Frame*.

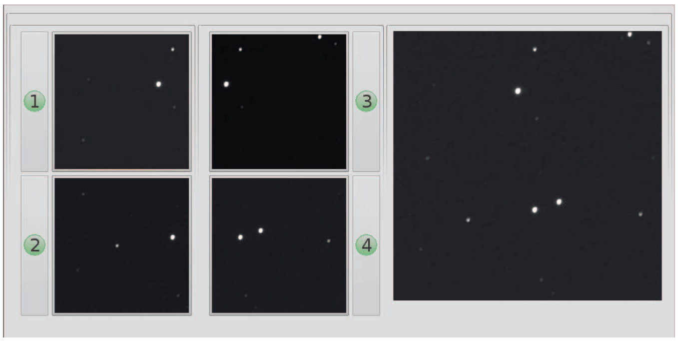

Figure 8.3: The *Target & Comparison Selection* screen of PhoS-T. **Right:** The original frame. **Left:** The original frame divided in four sub-frames. The user selects the target and the comparison star by clicking on the sub-frame. The software automatically defines the photometric window.

$$\mathfrak{F} = \sum_{i=1}^{I} \sum_{j=1}^{J} \mathfrak{f}_{i,j} \tag{8.4}$$

PhoS-T does not use apertures, thus it can easily handle defocused data, which is common for follow-up observations of transiting planets around bright stars.

The *Time and Airmass* sub-routine simply extracts the Julian date (JD) t and the airmass $a(t)$ from the fits header of the raw image. If there is no JD or modified JD (MJD) given in the header then the JD is calculated from the observing time and date. Using the JD the Heliocentric Julian Date (HJD) could be calculated. For the case of missing information about airmass, PhoS-T calculates the airmass using the coordinates of the pointing.

The *Final LC* sub-routine creates the final light curve $T(t)$ of the transit. First, it finds the correlation between airmass and the light curve of the comparison star(s) $C(t)$ and subtracts the airmass pattern from both the raw comparison light curve C_{raw} and the raw target light curve T_{raw}:

$$T(t) = \frac{T_{\mathrm{raw}}(t)/(\gamma_1 + \alpha \cdot a(t))}{C_{\mathrm{raw}}(t)/(\gamma_2 + \beta \cdot a(t))}. \tag{8.5}$$

Here, α, β, γ_1 and γ_2 are the free parameters of a linear fit to T_{raw} and C_{raw}, respectively. In Fig. 8.4 we show the final light curve after the airmass correction of the example object exoplanet XO-2b including a model fit (see Sects. 8.2.4 and 8.4).

8.2.4 Analysis function

The *Analysis* function includes the two sub-routines *Model Fit* and *Errors*. *Model Fit* uses the analytical transit model from Pál et al. 2008. As mentioned above, PhoS-T is a follow-up software. It is most efficient, if a rough parametrization of the transiting system, consistent of the host star and the transiting object, is already available. Provided that the period P is given, PhoS-T can fit the radius of the star R_{s}, the radius of the planet R_{p} (of course the output value is the ratio $R_{\mathrm{p}}/R_{\mathrm{s}}$), the semi-major axis α (again the output is the ratio of α/R_{s}) and the orbital inclination i with respect to the line of sight. Another set of input parameters are the limb darkening coefficients u_1

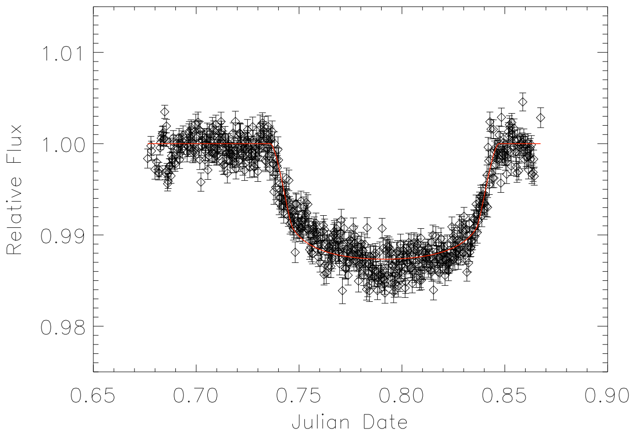

Figure 8.4: Final light curve of XO-2b (diamonds) and the transit model (red solid line). The model fit is not perfect at the first part of the transit because the data quality. The light curve shows a small asymmetry.

& u_2. However, the user is free to select the parameters to be fitted and she/he can choose which parameters should be fixed. After the user has defined the range of the parameters, a χ^2 fit of the model is applied to the full range (Fig. 8.4).

The *Errors* sub-routine relies on the bootstrap method (Alonso et al. 2008). After 1000 Monte Carlo simulations, a Gaussian distribution is fitted to define errors in all output parameters: the time of the center of the transit T_c, the transit duration (D), i, the ration α/R_s and the ratio of R_p/R_s.

8.2.5 CoRoT function

The *CoRoT* function is based on two sub-routines: *CDA* (CoRoT Detrend Algorithm - Mislis et. al. 2010) and *BLS* (Box Least Square Algorithm - Kovács et al. 2002). In the *CDA* mode the user can analyze raw CoRoT light curves. It deduces the transit period and removes trends and jumps from raw the light curves. *BLS* searches for transits in a light curve and calculates its period. When the period is known and the folded light curve is prepared, the user can go back at the *Analysis* function and apply a model fit for further analysis.

8.3 Graphical environment & technical details

The graphical environment of PhoS-T is built with the programming language GTK. For the majority of the sub-routines we have mainly used Python and AWK but also Fortran and Bash-scripting. The PhoS-T main screen is separated in two windows. The first one is the operating window where the user can select the functions and routines as described above. The second window is the display window, which shows output frames after the reduction, such as the aligned plots, the final light curve and the transit model fit. To ease the handling of the procedure, we have incorporated a few display dialogs.

In our example XO-2b (Sect. 8.4), we have used 774 frames, 22 bias frames, 40 dark frames, 26 flat frames, and 686 scientific frames with a virtual size of 1.5 Gb in total. Using a 4 GHz processor, PhoS-T needed roughly an hour for the full procedure, starting with the master frames creation and ending with the error calculation of the transit model.

8.4 PhoS-T in action: Photometric Follow up of XO-2b

We used PhoS-T to analyze follow-up photometric data of the transiting extrasolar planet XO-2b. This planet was announced and analyzed in detail by Burke et al. 2007, having an orbital period $P = 2.6$ days, mass $M_p = 0.57 M_\mathrm{J}$ and radius $R_p = 0.97 R_\mathrm{J}$. The host star, a K0 dwarf, has $V = 11.2$ mag and belongs to a proper-motion binary system, with an apparent distance of 30″ between the stars. The companion star has the same brightness and shares the same spectral characteristics of the planet-bearing star. Ground-based follow-up photometry has refined the transit ephemeris and confirmed the original transit parameters (Fernandez et al. 2009), and space-based infrared observations have detected thermal emission and a weak temperature inversion layer in the atmosphere of XO-2b (Machalek et al. 2009). Here we analyze a new transit of this extrasolar planet, obtaining a precise timing for the event which may be used to the search for evidence of a low-mass planetary companion (Agol et al. 2005; Holman & Murray 2005).

8.4.1 Observations and Results

To provide a high-quality light curve for the analysis of the transit of XO-2, we used the MONET 1.2-m telescope at McDonald Observatory (Hessman 2001). Data were obtained during the night between February 15 and 16, 2010, in remote observing mode. MONET has a 1K×1K Apogee Alta E47 CCD that gives a $5' \times 5'$ field and a pixel size of 0.30″ when the binning is 1×1. To minimize limb darkening effects on the shape of the transit light curve, observations were made using a Sloan *i* band filter. We used 15-second exposures, which provided and effective cadence of $\sim 25^{-1}$. Data calibration, photometry and light-curve analysis were performed using PhoS-T (Sec 9.2). Light-curve modeling results, including time of center-of-transit, are presented in Table 8.1, with previous results from Burke et al. 2007 (B07), Torres et al. 2008 (T08) and Fernandez et al. 2009 (F09). Also Fig. 8.5 shows the T_c results compare with previous values and Fig. 8.6 shows the residuals between PhoS-T and IRAF light curve.

8.5 Results & Conclusions

PhoS-T is a new software for data reduction, photometry and follow-up analysis of transiting planets. The software includes also functions for reduction and detection transit events in CoRoT light curves (CDA & BLS). The advantage of PhoS-T over established software flows from its graphical environment and its highly automatic operation. It comprises all the routines required for the standard analysis of transit light curves. In order to test the software, we re-examine new light curves of the well-known transiting planet XO-2b, obtained with the robotic 1.2m telescope MONET. We successfully reproduce the previously published values of the system and conclude that

Table 8.1: Physical Parameters of XO-2b exoplanet. We compare PhoS-T values with Burke et al. (2007), Torres et al. (2008) and Fernandez et al. (2009) (second third and fourth column respectively). The PhoS-T value of α/R_s is higher that the other values because the data quality (Fig. 8.4 - 8.6).

$XO-2b$ $Parameters$	$Burke$	$Torres$	$Fernandez$	$PhoS-T$	$Errors$
R_s/R_p	0.1040	0.1040	0.1049	0.1039	± 0.006
α/R_s	7.93	8.23	8.13	8.48	± 0.044
Inclination	88.90	88.90	88.87	88.95	± 0.028 [*deg.*]
Duration	160.72	160.28	161.74	159.70	± 0.860 [*min.*]

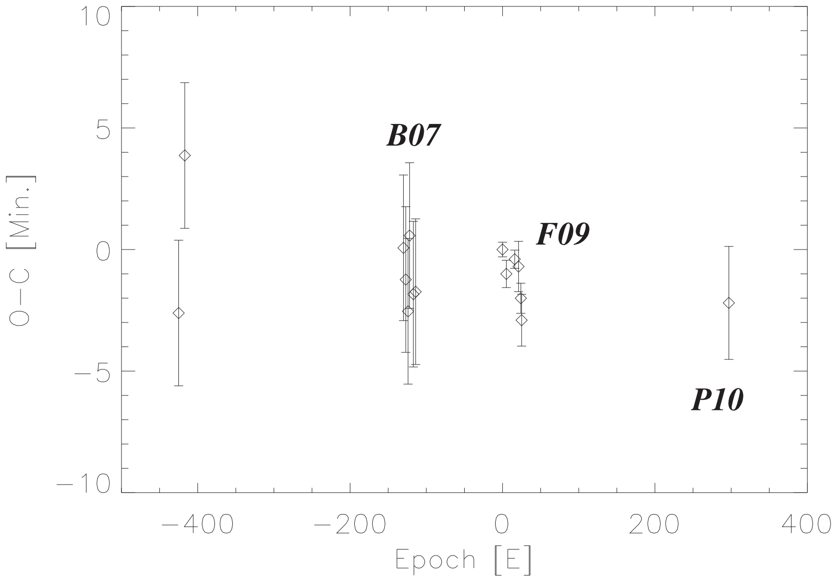

Figure 8.5: O-C diagram using values from Burke et al. (2007) and Fernandez et al. (2009). Our results match with previous results.

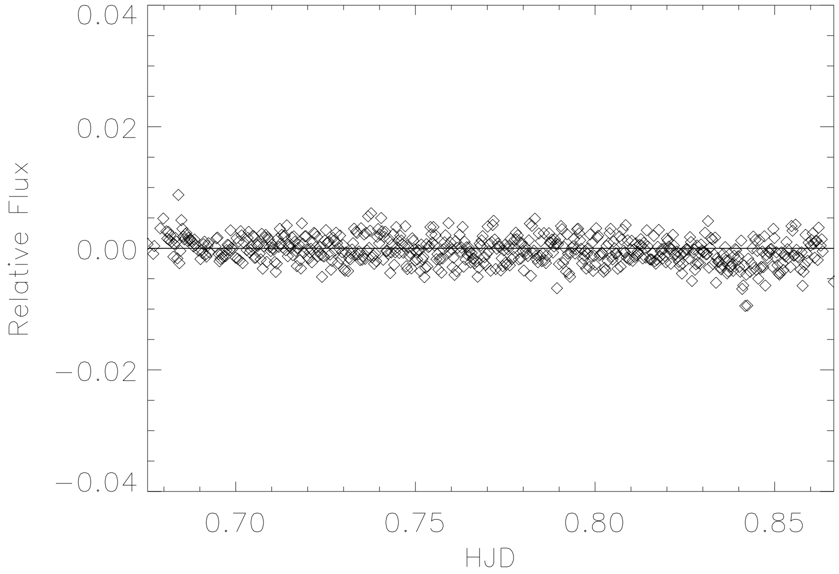

Figure 8.6: Residuals between PhoS-T photometry and IRAF photometry. The light curves obtained with both programs are in very good agreement.

data reduction, photometry, and the model fitting procedures of PhoS-T are coequal with well-established software.

8.6 Acknowledgements

D. Mislis and R. Heller are supported in the framework of the DFG-funded Research Training Group "Extrasolar Planets and their Host Stars" (DFG 1351/1). We thank I. Langa for the PhoS-T logo.

8.7 References

Agol, E., Steffen, J., Sari, R., & Clarkson, W. 2005, MNRAS, 359, 567
Alonso, R., Barbieri, M., Rabus, M., et al. 2008, A&A, 487, L5
Bakos, G. Á., Lázár, J., Papp, I., Sári, P., & Green, E. M. 2002, PASP, 114, 974
Borucki, W. J., Koch, D. G., Dunham, E. W., & Jenkins, J. M. 1997, in Astronomical Society of the Pacific Conference Series, Vol. 119
Burke, C. J., McCullough, P. R., Valenti, J. A., et al. 2007, ApJ, 671, 2115
Charbonneau, D., Brown, T. M., Burrows, A., & Laughlin, G. 2007, Protostars and Planets V, 701
Deleuil, M., Barge, P., Leger, A., & Schneider, J. 1997, in Astronomical Society of the Pacific Conference Series, Vol. 119
Fernandez, J. M., Holman, M. J., Winn, J. N., et al. 2009, AJ, 137, 4911
Gehrz, R. D., Reach, W., & Woodward, C. E. 2004, in COSPAR, Plenary Meeting,

Vol. 35, 35th COSPAR Scientific Assembly
Hessman, F. V. 2001, in Astronomical Society of the Pacific Conference Series, Vol. 246, IAU Colloq. 183
Holman, M. J. & Murray, N. W. 2005, Science, 307, 1288
Kovács, G., Zucker, S., & Mazeh, T. 2002, A&A, 391, 369
Machalek, P., McCullough, P. R., Burrows, A., et al. 2009, ApJ, 701, 514
McCullough, P. R., Stys, J., Valenti, J., et al. 2004, in Bulletin of the American Astronomical Society, Vol. 36
McDowell, J. 2001, S&T, 102, 30
Mighell, K. J. 1999, in Astronomical Society of the Pacific Conference Series, Vol. 189
Pál, A. 2008, MNRAS, 390, 281
Street, R. A., Pollaco, D. L., Fitzsimmons, A., et al. 2003, in Astronomical Society of the Pacific Conference Series, Vol. 294
Torres, G., Winn, J. N., & Holman, M. J. 2008, ApJ, 677, 1324
Udalski, A., Szymanski, M., Kaluzny, J., Kubiak, M., & Mateo, M. 1992, Acta Astronomica, 42, 253

Chapter 9

Conclusions

In this Thesis we present a study of transiting exoplanets using ground based data and techniques and space missions, as well. We have studied TrES-2b exoplanet system using the 1.2m OLT telescope and 2.2m Calar Alto telescope (BUSCA CCD). TrES-2b is an interesting system because the $\alpha \cos i$ parameter of the system is high enough to assume that the planet is almost grazing. We have three transiting light curves using OLT and one more (four filters simultaneously) using BUSCA CCD in a one year period (May 2008 - May 2009). We compare our results with previous results from other teams and we found that the inclination of TrES-2b decreases since November 2006. Also, Using ground based data and multi-band observations we prove that the limb darkening coefficients can not explain this change in inclination of TrES-2b. The most probable scenario for the change, is a non-transiting secondary planet (low inclination) who causes the variation at the inclination of the system.

We also present probability maps for Hot Jupiters and habitable transiting planets. Our analysis have showed, that the probability for a ground based survey (SuperWasp, HatNet, XO, Best) is a function of the resolution of the instrument and the FOV. Based on Tycho catalog simulations, we found that the expected number of transits for the most surveys, is not higher that 13% per field. Additional, another conclusion for this study, is that the expected number of transits around bright stars is much higher that the detected number of transits in a range of $6 < m_V < 9$ (full sky). For our second experiment, we have used data from CoRoT's IRa01 field. The IRa01 field has ~ 14000 stars and our simulations show, that the probability for CoRoT to detect a habitable planet in this field is $\sim 15\%$, but the probability of course, increases with the number of sample stars. From the theoretical study, we found an eccentricity threshold for habitable exoplanets. Eccentricities which are above this threshold are forbitten for habitable planets ($e_{max} = 0.397$), and it is independent for the stellar or planetary characteristics.

We have continued our work with CoRoT data by presenting the CoRoT Detrent Algorithm (CDA). More that 50% of CoRoT light curves shuffers by jumps and trends in flux, which affect and destroy the light curve. We prove that if a light curve of a faint star shuffers by these jumps and trends, then is impossible to detect a small transiting planet in this light curve. Using CDA we are able to reduce all annoying features and detect small transits around faint stars. Our examples (simulations and real data) show that the CDA is able to detect quite small transiting planets ($R_p \sim 6R_E$) around faint stars ($m_V \sim 15$). The procedure is fully automatic.

In the mean time, Kepler mission was launch on 2009 and we continue the studies for transiting theory. We present a method, which allows us to estimate planetary characteristics using only the transiting photometric light curve of the planet without radial velocity measurements. If the accuracy of the light curve is high enough ($> 10^{-4}$), the reflected light from the planetary surface is detectable. Kepler's equations show that the phase of the planet is quite similar to the RV curve, and gives us information about the orientation of the periaston (ω), the eccentricity (e) and the geometrca albedo of the planet (a_g).

Finally, we have developed the Photometric Softawre for Transits (PhoS-T) for data reduction analysis and model fit of transiting exoplanets. Furthermore, PhoS-T, includes routines for correction and analysis of CoRoT light curves using the CoRoT Detrend Algorithm (see chapter 6). PhoS-T is an open-source, graphical software.

Appendix A

PhoS-T manual

Version 1.0 - Manual
D. Mislis, R.Heller, J. Fernandez, U. Seemann
Hamburg 2010

Introduction

PhoS-T is an open-source graphical software for the data reduction of transiting exoplanets, for light curves analysis and for CoRoT light curve detrending. The code is written in the graphical language GTK. PhoS-T also bases on Python (including the PyFits routine), AWK, Fortran, Gnuplot, and bash-scripts. The software is split in three basic modes. The first one handles typical data reduction procedures, such as bias, dark, and flat corrections, photometry and light curve analysis (transit modeling & error distribution). In the second mode, the user may analyze his transit light curves using Monte Carlo simulations. The third mode detrends CoRoT light curves with thee aid of the CoRoT Detrend Algorithm (CDA - Mislis et al. 2010a). This mode provides a search for transiting planets with Box Least Squares (BLS, Kovács et al. 2002) and models to be fitted to the final light curve.

Technical Requirements

PhoS-T requires GTK-dialog 0.7.20 or higher, Python 2.6.2 or higher (including PyFits), the Inter Fortran Compiler (ifort), AWK 3.1.6 or higher, and Gnuplot 4.2. A processor with 4 GHz yields results within a reasonable amount of real time. We recommend the user to have at least three times of the virtual space of the data available for the output files.

Getting started

PhoS-T can easily be started by clicking on the PhoS-T icon. The **Start Window** (Fig. A.1) then opens, asking the user if he wants to load a previous project (a project that was saved before) or open a new one. Let us assume that we want to start a new project. After pressing the ***New project*** button, the **Input Window** opens (Fig. A.2), which is divided into three columns, headed **File names**, **System & Coordinates**, and **Directories**. One can now enter the relevant information into the free fields or leave all fields blank and mark the ***CoRoT*** button at the lower left of the window. If this box is selected, the third mode of PhoS-T is activated while all input fields above become inactive.

In order to proceed with the reduction of data that is not from CoRoT, one needs to fill the empty input fields. In the first column (**File Names**) the user is asked for the leading name of the data files. If the target file names are, e.g., HD209458-001.fits, HD209458-002.fits, HD209458-003.fits etc., then the leading name of the scientific files is ’HD209458-’. The same procedure is then applied to the bias, dark, and flat files. Enter the files’ extension into the last field of that column (e.g. ’fit’, ’fits’ or ’FIT’)!

In the second column **System & Coordinates** the user enters information about the CCD, such as gain in units of ADU/e^{-}, pixel size in units of arcseconds, readout noise $[e^{-}]$, and the coordinates of the target, where the right accession (RA) in units of degrees must be a value between 0 and 360 and the declination (DEC) must be between -90 and +90, also in units of degrees.

Check, and eventually change, the directory of your data files in the third column **Directories**! By default, the directory of the program is given. Finally, press the ***Start*** button to continue!

Screens

Main screen

After pressing the ***Start*** button, the two screens of PhoS-T appear. The **Main Screen** is shown in Fig. A.3. Here, the user can apply all the functions and subroutines of the program, available on the tool bar. At the right, one finds two buttons and two sub-windows for information about the status. The ***FITS Header*** button displays the fits-header of our scientific frames. Pressing the

Do you want to load an existing project or create a new one

Figure A.1: The **Start Window** dialog.

Show Procedure button, one opens another window showing which functions and procedures have already been applied (Fig. A.4). Each text field of a sub-routine is labeled by a color. Yellow stands for a sub-routine that is not applied yet. A green flag means that data has passed this procedure successfully, whereas red means that data did not pass the procedure successfully. A gray background indicates that the routine is not available. This can happen, e.g. when the data reduction mode (the first mode) is active and all the CoRoT sub-routines are not available, thus shaded in gray. This window can be useful if the user loads a previous project, summing up the project's progress.

After a sub-routine is applied, one might press the ***Refresh*** button to display comments on the status in the **Messages** sub-frame (lower right in Fig. A.3). In the lower left of the **Main Screen** the sub-window **Data Files** shows how many bias, dark, flat and scientific frames are in use.

Display screen

The second window is the **Display Screen** (Fig. A.5). Here, the user can visually check frames and plot graphs. The display screen is split in two parts: The **Main Display Window** and the **Graph Display Window**. The former one shows the scientific frames such as master-bias, master-dark and master-flat frames. The user can select among three contrast scales: ***linear***, ***logarithmic*** and ***square root***. A number of plots can be produced after the data reduction, by pressing the ***Select Graph from the list*** button: *Tycho Map*, *X offset*, *Y Offset*, *Target Raw*, *Comparison Raw*, *Final Curve*, *Model Fit*, *Before CDA*, *After CDA*, *Both CDA*, *BLS Single Search*, and *BLS Single Phase*. When the button ***Plot*** is hit, the graph is displayed in the **Graph Display Window**. The Tycho Map shows a number of reference stars with some information for the current field of the sky.

First mode

Data reduction

The tool-bar at the top of the **Main Screen** contains all the available routines. To run a consecutive reduction procedure, first apply the ***Data Reduction*** on the raw data! This function has two sub-functions: ***Master Frames*** and ***Reduction***. By choosing the ***Master Frames***, the software

FILE NAMES

prefix of science frames (e.g. "HD_" for "HD_001.fits"): HD_

prefix of bias frames (e.g. "BIAS_" for "BIAS_001.fits"): BIAS_

prefix of dark frames (e.g. "DARK_" for "DARK_001.fits"): DARK_

prefix of flat frames (e.g. "FLAT_" for "FLAT_001.fits"): FLAT_

file extension (e.g. "fit" for "HD001.fit"): fit

System & Coordinates

CCD gain [ADU/e-]: gain

pixel size [arcsec]: pixel_size

readout noise [e-]: rout

0 < RA < 360 [dec]: RA

-90 < DEC < 90 [deg]: DEC

Directories

system directory: /home/dimitris/Desktop/work

data directory: /home/dimitris/Desktop/work

List of files:
bias.10.fits
bias.11.fits
bias.12.fits
bias.13.fits
bias.14.fits
bias.15.fits
bias.16.fits
bias.17.fits
bias.18.fits
bias.19.fits
bias.1.fits

CoRoT

Click the COROT box if you want to work with PhOS third mode & CoRoT data

☐ COROT

Figure A.2: The **Input Window**.

collects all the noise frames (e.g. bias, dark and flats) and creates three master frames: Master Bias, Master Dark, and Master Flat. Some telescopes and CCDs do not show any dark pattern. In this case, or of no dark is available, it is better to type nodark into the 'prefix of dark frames' line in the first dialog window (left column in Fig. A.2). Then the software will avoid the master-dark sub-routine. When the procedure has finished, a message will appear, saying that the Master Frames are ready to be displayed, simply by clicking the ***Master Bias***, ***Master Dark*** or ***Master Flat*** button in the display screen.

Gone so far, the data are ready for reduction. To do so, choose ***Reduction***! Based on standard equations (Mislis et al. 2010b), the software will then remove the master frames from the light frames of the science data. It typically takes a few seconds until the first light frame is ready for the display, available via the ***Light Frame*** button at the upper right of the Graph display window.

Align

The ***Align*** function has three sub-functions: ***Guide Stars Offset***, ***Target Star***, and ***Comparison Star***. By pressing the ***Guide Star Offset***, the software defines the two brightest stars in a reference frame and computes the offset of the brightest one in the x- and y-coordinates. This sub-routine needs some minutes to run completely. A time-bar will pop up to show the overall time that is need for the procedure. Done that, three plots are ready to be plotted. In the **Graph Display Window**, the XY-Offset option plots the offset of Y-axis vs X-axis. The X-Offset plot shows the X-axis offset vs. frame number and the Y-Offset graph shows the Y-axis offset vs. frame number (Fig. A.6). These plots provide an estimate of the tracking quality and/or the guiding of the telescope, which will directly impact the accuracy of the photometry.

The ***Target Star*** & the ***Standard Star*** sub-routines are apply the same principals to the target

```
LIGHT FRAMES : 499
BIAS  FRAMES  : 30
DARK FRAMES  : 1
FLAT FRAMES    : 70

================
TOTAL        : 600
```

```
16:48:07 > reading characteristics
16:48:07 > making frame lists
16:48:49 > FIT image created
16:48:55 > TYCHO image created
16:49:24 > MasterBias created
16:49:35 > Master Dark created
16:49:44 > Master Flat created
```

Figure A.3: The **Main Window**.

star and the comparison star. When the user selects ***Target Star*** (***Standard Star***) a new window opens, shown in Fig. A.7. In the right panel, you see the reference light frame while at the left you find a quadruple of sub-frames. Each sub-frame is a button. The user may now click on one of these sub-frames, where the target star is located. After this first selection, the right frame is reloaded and shows a larger version of the chosen sub-frame, whereas the left frame provides again a quadruple of sub-frames of the image at the right. The user should redo this choice until only the target star remains in one of the four sub-frames at the left. This respective sub-frame which contains only the target star is now being defined as the photometric window: When your target star (standard star) is appears solely in one of the four sub-frames, check the box next to the ***Select Sub-Window*** option at the lower left. The inactive numbers (1, 2, 3 or 4) that label the sub-images become active. These numbers act as buttons. Press now the correct button of the image that comprises your star! By clicking on the ***Reset*** button, the whole selection procedure starts from the initial image.

Photometry

The ***Photometry*** routine contains three sub-routines: ***Aperture Photometry***, ***Time & Airmass***, and ***Light Curve***. When the ***Aperture Photometry*** is selected, the intensity of the target and comparison star are being calculated until, after some minutes, new graphs are ready to be displayed. The ***Target Raw*** and ***Comparison Raw*** light curves are the raw light curves. In these plots, the ordinate refers to photon flux and abscissa denotes the frame number. If these two raw light curves show completely different shapes, the comparison star is probably not good

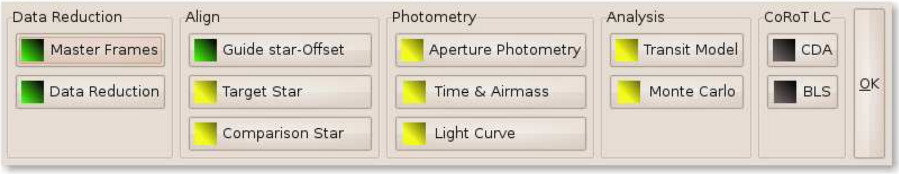

Figure A.4: The **Show Procedure Window**.

enough. The user is recommended to go back to the ***Standard Star*** sub-routine to select another comparison star.

For the case the photometry meets the expectations, one may continue with the ***Time & Airmass***. This sub-routine extracts the time (Julian Date [JD], Modified Julian Date [MJD] etc.) and the airmass values from the header of each frame. Before this sub-routine is chosen, it is recommended to click the ***Fits Header*** button in the **Main Window** for the correct header name of JD and airmass. But **Time & Airmass** can also obtain the JD from the real time of each frame using the observing date and time (dd.mm.yyyy hh:mm:ss) or the airmass from the telescope altitude. Starting the ***Time & Airmass*** sub-routine opens a new window to which one needs to pass the variable names, used in the header of the data file. Alternatively, the telescope altitude can be chosen. If there is no information available about JD or MJD, one may choose the observing date and the time format. In every case the header names must be correct. Finally, the user need to give the site coordinates, because at the end the software convert the time to the Heliocentric Julian Date [HJD].

When ***Time & Airmass*** has completed, one can proceed with the ***Light Curve*** sub-routine. After its selection, one is asked whether or not one wants to correct the raw light curves using the airmass calculated with ***Time & Airmass***. The decision can be made after checking the raw light curves by eyes. One may now plot the final light curve in the **Graph Display Window** by pressing ***Final Curve***.

Second Mode

In the Second Mode, the user can either analyze the light curves as produced with the First Mode or she/he can load any other light curve for analysis. This light curve must have three columns: JD (or MJD, or HJD), relative flux normalized to unity, and errors. The filename of this light curve must be ”finsub.lc” and must exists in the PhoS-T home folder. For the case the light curve was produced with the PhoS-T project no modification is required.

Analysis

The ***Analysis*** has two sub-routines: ***Transit Modeling*** and ***Monte Carlo***. Using the ***Transit Modeling***, PhoS-T fits the Pal et al. (2008) model to the light curve. A new dialog window appears (Fig. A.9), asking for information about the values to be fitted. The available fitting parameters are the radius of the star (R_s), the radius of the planet (R_p), inclination (i), and semi-major axis (a). The limb darkening coefficients (u_1 and u_2) and the period (P) are fixed meanwhile. If one (or more) of the parameters is known, it is not necessary to be fitted again. After applying this procedure, one more graph is ready to be plotted: ***Model Fit***.

Monte Carlo (MC) simulations are the next tool for the error analysis of our model. First, PhoS-T runs the MC time calculator, which estimates the time (in minutes) that the software will need to complete 100 MC simulations. But before that, one definse the parameters for which the errors shall be computed (R_p, R_s, a, and i are available). The boxes attached to those parameters for which the error calculation is going to be run must be un-checked. If checked, the respective parameter will be fixed. Then PhoS-T will search for errors in the same range that were used during the ***Transit Modeling***. After the MC time calculator has finished another dialog window opens, asking which parameters shall be simulated and how many MC loops will be run. In the output folder one finally finds an ASCII file named Final-Error.txt with all the relevant information of the simulation. For this whole procedure, the bootstrap technique is used to estimate errors (Alonso et. al. 2008).

Third Mode

In the third mode of PhoS-T, one can detrend CoRoT light curves, search for transiting planets, and apply model fits. The raw CoRoT light curve should have the default name CoRoT*corotID*.txt 1 from the CoRoT database : http://idoc-corot.ias.u-psud.fr (e.g. CoRoT0102773260.txt).

CoRoT LC

The ***CoRoT LC*** routine has two sub-routines: ***CDA***, ***BLS Low Accuracy***, and ***BLS High Accuracy***. First of all, we need to detrend the CoRoT light curve for jumps and trends by selecting ***CDA***. ***CDA*** is an abbreaviation for CoRoT Detrend Algorithm explained in Mislis et al. (2010a). Once the CDA dialog window is opened, one needs to specify the CoRoT filename from the list, or to check the ***ALL LC*** box if the CDA shall be applied to all CoRoT light curves (Fig. A.10). After the ***CDA*** has been applied, fresh plots are available in the **Graph display window** (see Fig. A.5), named *Before CDA*, *After CDA*, and *Both CDA*. *Before CDA* shows the raw CoRoT light curve. *After CDA* shows the CDA-treated plot and *Both CDA* displays an overplot of both the untreated and the CDA-treated graphs.

The two remaining sub-routines ***BLS Low Accuracy*** and ***BLS High Accuracy*** search for periodic transit signals in the light curve, based on the Box Least Square algorithm (Kovács et al. 2002). At first, the user must run the ***BLS Low Accuracy*** routine. Some output of this step will be required for the ***BLS High Accuracy*** explained below. Then, choosing ***ALL LC*** in the new dialog window prompts the software to perform a search in all available CoRoT light curves that have passed the ***CDA*** procedure. If ***ALL LC*** is not selected, the user must select a single light curve from the list below and define the period range in which BLS will explore. For the ***ALL LC*** mode there is no output plot. For each star there are two output files, filename.bls and filename.bls.info. The former one contains five columns (P, BLS value, number of the data point where the box model starts, model duration [in units of data points] and model depth [in units of relative flux]), while the latter file gives the values for the minimum BLS value, which denotes the bet fit. For the case a single light curve has been investigated, two new plots are available. The *BLS Single Star* shows the periodicity plot (BLS number vs. period) for the star and the *BLS Single Phase* displays the phase diagram of the light curve for the best-fit period. In the filename.bls.info file one finds the significance, which is the difference between the root mean square of the BLS and the minimum BLS in units of sigma. Intuitively, low values for the significance indicate that probably no transit occurs in the light curve.

The ***BLS Low Accuracy*** uses two positions after decimal point, which are enough to discern a transit from the noise. That saves time in opposite to running the high-accuracy way at first instance.

The ***BLS High Accuracy*** runs the same mathematical procedure as the low-accuracy method, but it uses five positions after decimal point. It applies the BLS fit to the a period window selected with the low accuracy procedure.

Finally, ***Transit Modeling*** and ***Monte Carlo*** are the same sub-routines as introduced above for the Analysis routine (Sect. Analysis). The user merely needs to define, which CoRoT light curve should be taken for the modeling.

Be aware that CoRoT files contain thousands of data points. PhoS-T requires between a few minutes and several hours to complete the BLS routines.

Output files

At any point, the user can save the project and continue later. To save the project, intuitively go to ***File*** on the tool bar and then ***Save*** as you are used to. To load a project, choose ***File*** and ***Load***. Outputs are ASCII files so the user may use any other convenient software to produce plots. Once the program is started, a folder phost-output is created in the program folder. All output files will be stored there.

Be sure to save all output files located in the phost-output folder before a new project is started! Starting a new project erases all files from this folder.

To exit PhoS-T, check the Secure exit box at the lower right in the Display Screen (Fig. A.5)!

Installation

PhoS-T comes with three sub-folders: ”Bin”, ”code-icons”, and ”install-phos”. To install the software, open a terminal and navigate to the PhoS-T directory:

```
dmislis:>cd /home/dimitris/Desktop/phost
```

Here you find the install folder ”install phos”, which you are supposed to enter now:

```
dmislis:>cd install phos
```

When the the installation script is run by

```
dmislis:>./install.sh
```

the PHOS-T directory and the home directory must be defined as well:

```
======= PhoS-T Installation script
HOME directory:
PhoS-T directory:
```

After that, a PhoS-T application-file appears at the Desktop. If the logo icon does not appear, give a right-click to the PhoS-T application and then select the PhoS-T.png logo as the application icon located at ”/usr/share/pixmaps”. PhoS-T starts with a double-click on the Desktop application. To complete the installation you need to know the root password.

Do not change or rename the PhoS-T home directory phost! If you need to do that, run the installation script and enter your custom PhoS-T home directory.

Before work with PhoS-T

We recommend to copy all the raw data (bias, flat, dark, scientific frames or CoRoT light curves) to the PhoS-T directory before running the program. If PhoS-T detects these files in an external folder, it will automatically copy these data into the phost directory. If the system directory and the data directory (right column in Fig. 2) coincide, this will save time when PhoS-T is running.

For more information, comments and questions visit
`www.hs.uni-hamburg.de/grk/phost`
or press the About button in the main tool bar of PhoS-T.

Acknowledgements

Our sincere thanks go to Frederic Hessmann and the MONET team who supplied us with data that we used to test PhoS-T. We also thank Ioanna Langa for the PhoS-T logo.

References

Alonso, R., Barbieri, M., Rabus, M., et al. 2008, A&A, 487, L5
Kovács, G., Zucker, S., & Mazeh, T. 2002, A&A, 391, 369
Mislis, D., Schmitt, J.H.M.M., Carone, L., Guenther, E., Pätzold, M. 2010a, subm. to A&A
Mislis, D., Fernandez, J., Heller, R., Seemann, U., 2010b, submitted to A&A
Pal, A. 2008, MNRAS, 390, 281

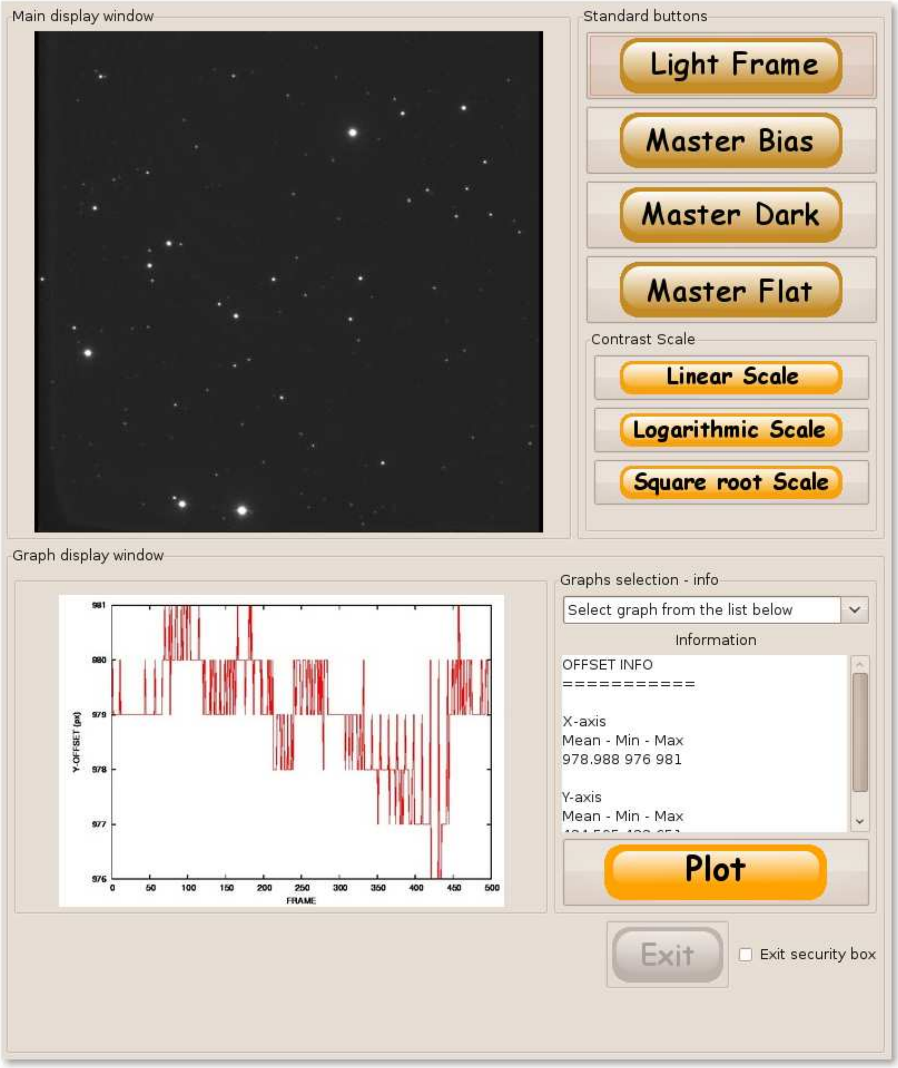

```
OFFSET INFO
============

X-axis
Mean - Min - Max
978.988 976 981

Y-axis
Mean - Min - Max
```

Figure A.5: The **Display Screen**. As an example the Y-offset is plotted in the **Graph Display Window**.

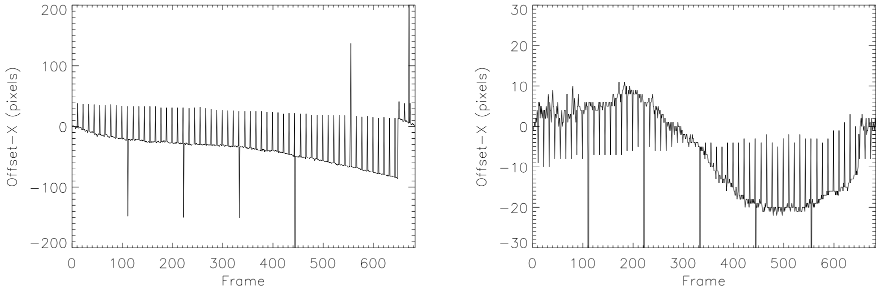

Figure A.6: Top: X-Offset vs. frame number. Bottom: Y-Offset vs. frame number. In this example the offset in both axes quite large.

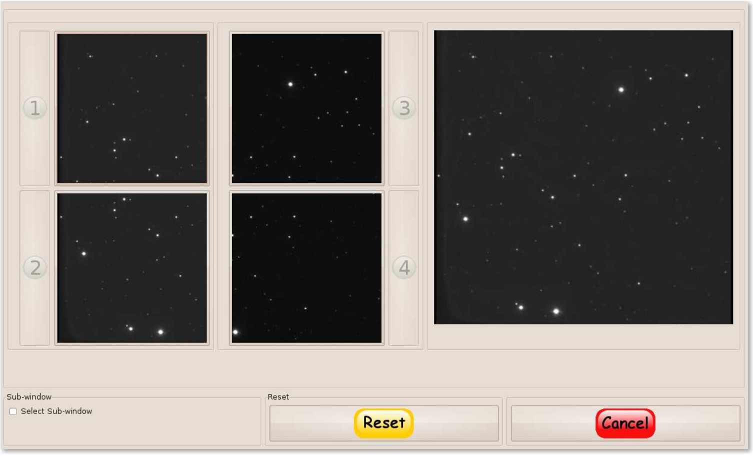

☐ Select Sub-window

Figure A.7: **Target (Standard) Star Window**. The ***Select Sub-Window*** box is not checked and thus the numbered buttons beside the sub-images are inactive.

☑ Select Sub-window

Figure A.8: **Target (Standard) Star Window**. Now the ***Select Sub-Window*** box is checked and the numbered buttons beside the sub-images are active.

Star Radius [Rs]

☐ Fit Star Radius

1.20

Start fit

End fit

Planet Radius [Rj]

☑ Fit Planet Radius

0.00

1.80

1.90

Period [days]

2.470610

Semi-major Axis

0.0367

Inclination [deg]

☑ Fit Inclination

00.00

83.80

90.0

Limb darkening

0.22

0.32

Figure A.9: Transit Modeling dialog window. In this example, we fit R_p (range 1.8 to 1.9 R_J) and inclination (range 83.80 to 90.00^o). We have fixed all the other parameters.

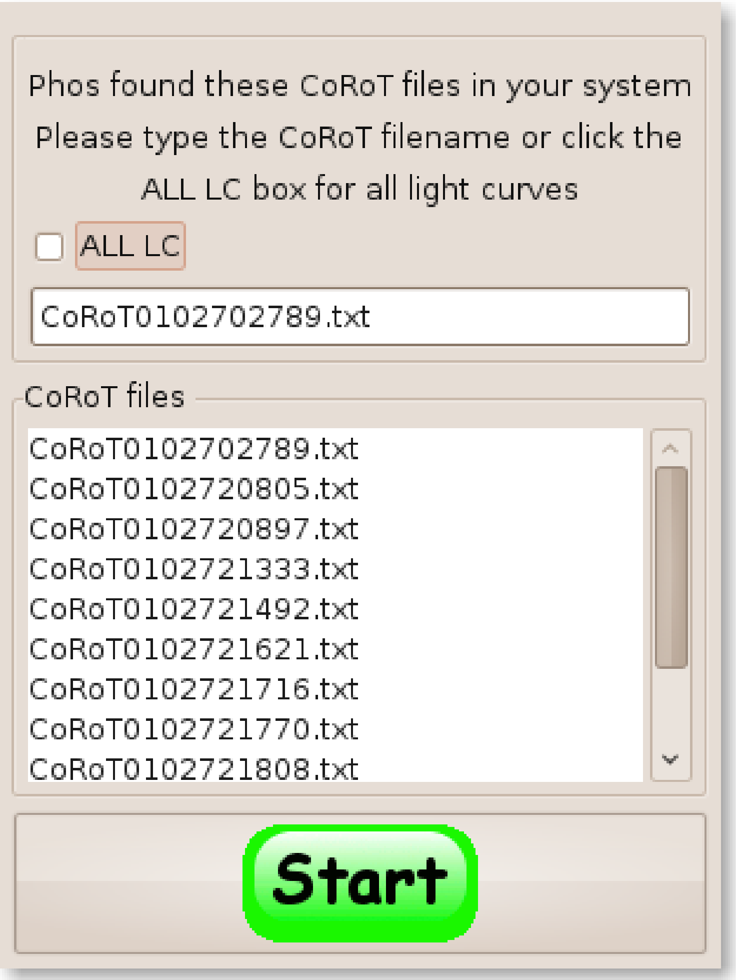

Phos found these CoRoT files in your system
Please type the CoRoT filename or click the
ALL LC box for all light curves

☐ ALL LC

CoRoT0102702789.txt

CoRoT files

CoRoT0102702789.txt
CoRoT0102720805.txt
CoRoT0102720897.txt
CoRoT0102721333.txt
CoRoT0102721492.txt
CoRoT0102721621.txt
CoRoT0102721716.txt
CoRoT0102721770.txt
CoRoT0102721808.txt

Figure A.10: The CDA dialog window. Type the CoRoT filename form the CoRoT list or click ALL LC box if you want to apply CDA to all light curves.